Heinrich Heine
Universität
Düsseldorf

Structure and interaction of polymer functionalized gold nanoparticles in non-aqueous media

Inaugural-Dissertation

zum Erlangen des Doktorgrades
der Mathematisch-Naturwissenschaftlichen Fakultät
der Heinrich-Heine-Universität Düsseldorf

vorgelegt von

Julian Sindram
aus Berlin

Düsseldorf, August 2025

aus dem Institut für Physikalische Chemie I
der Heinrich-Heine-Universität Düsseldorf

Gedruckt mit Genehmigung der
Mathematisch-Naturwissenschaftlichen Fakultät der
Heinrich-Heine-Universität Düsseldorf

Berichterstatter:

1. Prof. Dr. Matthias Karg

2. Prof. Dr. Peter Gilch

3. Prof. Dr. Thomas Hellweg

Tag der mündlichen Prüfung: 07.03.2025

Eidesstattliche Erklärung

Ich versichere an Eides Statt, dass die Dissertation von mir selbständig und ohne unzulässige fremde Hilfe unter Beachtung der "Grundsätze zur Sicherung guter wissenschaftlicher Praxis" an der Heinrich-Heine-Universität Düsseldorf erstellt worden ist.

Diese Dissertation wurde ausschließlich der Mathematisch-Naturwissenschaftlichen Fakultät der Heinrich-Heine-Universität Düsseldorf vorgelegt und ist nicht Gegenstand anderer Promotionsverfahren.

Ort, Datum	Unterschrift

Abstract

Nanoparticles possess unique properties compared to corresponding bulk materials of identical composition. Potential applications in composite materials, catalysis, sensing, and many other areas have driven research of nanoparticles and nanomaterials for decades. One of the key challenges in harnessing the unique properties of nanoparticles is the limited stability of finely dispersed matter. Stabilizing agents therefore represent an intrinsic part of the preparation and handling of nanoparticles. This work deals with the preparation and characterization of polymer functionalized gold nanoparticles. Using a novel approach, gold nanoparticles are transferred to an organic phase and stabilized by end-grafted polystyrene ligands. These composite particles are then characterized by a wide range of methods. Dynamic light scattering and analytical ultracentrifugation are used to examine the scaling of the brush height regarding ligand chain length and grafting density. Although high polymer grafting densities are achieved in general, there is a strong negative correlation between the chain length and the grafting density. The particles can be stabilized in a variety of organic solvents. The optical properties of the plasmonic gold particles are characterized by UV/Vis spectroscopy. A complex dependence on the refractive index of the solvent and brush swelling in that solvent is found. Small-angle x-ray scattering confirms the presence of attractive inter-particle interactions in non-polar solvents. The mechanism of ligand binding to the nanoparticle surface is investigated in fluorescence-based kinetic experiments. A distinct ligand chain length dependence of the effective rate constant suggests a diffusion-limited mechanism, which can also explain the lower grafting densities of polymer brushes formed by longer polymer chains. These findings can potentially be applied to other particle materials and polymers and aid in the development of stable composite materials that are compatible with a broad range of media and matrices.

Kurzzusammenfassung

Nanopartikel besitzen einzigartige Eigenschaften verglichen mit makroskopischen Körpern gleicher Zusammensetzung. Anwendungsmöglichkeiten in Kompositwerkstoffen, Katalyse, Sensorik und vielen anderen Bereichen haben die Forschung an Nanopartikeln und Nanomaterialien für Jahrzehnte angetrieben. Eine Herausforderung bei der Nutzbarmachung der besonderen Eigenschaften von Nanopartikeln ist die begrenzte Stabilität feindisperser Materie. Stabilisatoren stellen daher einen zentralen Aspekt der Herstellung und Verarbeitung von Nanopartikeln dar. Diese Arbeit befasst sich mit der Darstellung und Charakterisierung polymerfunktionalisierter Gold-Nanopartikel. Mittels einer neu entwickelten Methode werden Gold-Nanopartikel in eine organische Phase überführt und durch terminal angebundene Polystyrol-Liganden stabilisiert. Diese Komposite werden mit einer Reihe von Methoden charakterisiert. Die Abhängigkeit der Dicke und Dichte der Ligandenschicht vom Molekulargewicht der Liganden wird mittels dynamischer Lichtstreuung und analytischer Ultrazentrifugation untersucht. Trotz insgesamt hoher Pfropfdichten, gibt es eine negative Korrelation zwischen Molekulargewicht und Pfropfdichte. Die Partikel können in diversen organischen Lösungsmitteln stabilisiert werden. Die optischen Eigenschaften der plasmonischen Gold-Partikel werden mittels UV/Vis-Spektroskopie untersucht. Eine komplexe Abhängigkeit vom Brechungsindex des Lösungsmittels und Quellung der Polymerschicht wird beobachtet. Kleinwinkel-Röntgenstreuung zeigt das Auftreten attraktiver Wechselwirkungen zwischen Partikeln in unpolaren Medien. Der Mechanismus der Ligandenanbindung wird mittels fluoreszenzbasierter kinetischer Experimente untersucht. Eine Abhängigkeit der effektiven Geschwindigkeitskonstante von der Kettenlänge der Liganden legt einen diffusionslimitierten Mechanismus nahe, welcher auch die niedrigeren Pfropfdichten von Schichten aus längeren Polymerketten erklärt. Diese Ergebnisse können potenziell auf anderen Partikelmaterialien und Polymere übertragen werden und zur Entwicklung stabiler Komposite beitragen.

Acknowledgments

This Ph.D. thesis is based on research conducted at the Heinrich-Heine-Universität Düsseldorf between 2016 and 2021. Research was conducted under supervision of Prof. Matthias Karg, whom I thank for his support and guidance throughout these years. When I first met him in Bayreuth, his fascination for the world of particles and polymers had a contagious effect on me and has influenced my professional life ever since. I also admire his attention to detail, which he has upheld and encouraged in a scientific world often valuing quantity over quality.

I would like to thank Prof. Paul Mulvaney for his hospitality and supervision during my six-month stay with his group at the University of Melbourne, Australia. I would also like to extend this gratitude to his group members at this time, who made for excellent company and were a source for vivid scientific exchange.

The same has to be said for my colleagues in Düsseldorf, especially Kristina, Kirsten, Arne, and Joe, who also moved from Bayreuth and became good friends during the following years. It has also been a great pleasure to work with a new generation of colleagues, who were eager to learn and have since become experts in their field. I would also like to thank Jule, Lukas, Pauline, Lucas, Saskia, and Anna, the students I supervised over the years, for their quick mastery of complex topics and their contribution to my own research.

Special thanks go to the members of other HHU institutions that have contributed to this work; Dr. Luitgard Nagel-Steger and Dr. Thomas Pauly from the Institute for Physical Biology for AUC measurements, Stephanie Scheelen from the Institute for Macromolecular Chemistry for SEC measurements, Gaby Zerta from the Institute for Pharmaceutical and Medicinal Chemistry for elemental analysis, the NMR department led by PD Dr. Klaus Schaper, and the mass spectrometry department led by Dr. Peter Tommes.

Finally, I would like to thank my friends and family for their support and their understanding for the amount of time and effort that went into writing this thesis, which I was consequently unable to spend with them.

List of publications

The following publications were finished during my tenure as Ph.D. student at the Heinrich-Heine-University Düsseldorf.

- Sindram, J.; Volk, K.; Mulvaney, P.; Karg, M. Silver Nanoparticle gradient arrays: Fluorescence enhancement of organic dyes. *Langmuir*, **2019**, *35* (26), 8776-8783. doi: 10.1021/acs.langmuir.9b01027

- Carl, N.; Sindram, J.; Gallei, M.; Egelhaaf, S. U.; Karg, M. From normal diffusion to superdiffusion: Photothermal heating of plasmonic core-shell microgels. *Phys. Rev. E*, **2019**, *100* (5), 052605. doi: 10.1103/PhysRevE.100.052605

- Banger, A.; Sindram, J.; Otten, M.; Kania, J.; Wilms, D.; Strzelczyk, A.; Miletic, S.; Marlovits, T. C.; Karg, M.; Hartmann, L. Synthesis and self-assembly of amphiphilic precision glycomacromolecules. *Polym. Chem.*, **2021**, *12* (3), 4795-4802. doi: 10.1039/D1PY00422K

- Sindram, J.; Krüsmann, M.; Otten, M.; Pauly, T.; Nagel-Steger, L.; Karg, M. Versatile route toward hydrophobically polymer-grafted gold nanoparticles from aqueous dispersions. *J. Phys. Chem. B*, **2021**, *125* (29), 8225-8237. doi: 10.1021/acs.jpcb.1c03772

- Sindram, J.; Karg, M. Polymer ligand binding to surface-immobilized gold nanoparticles: a fluorescence-based study on the adsorption kinetics. *Soft Matter*, **2021**, *17* (32), 7487-7497. doi: 10.1039/D1SM00892G

List of conference contributions

The following conference contributions were made during my tenure as Ph.D. student at the Heinrich-Heine-University Düsseldorf.

- Annual symposium of the German Physical Society (DPG), Regensburg, Germany 2016. Poster: Resonant energy-transfer in plasmonic hybrid arrays.
- Australasian Colloid and Interface Symposium, Coffs Harbour, Australia 2017. Talk: Silver nanoparticle size maps as versatile platform for optical screening.
- Zsigmondy Colloquium, Dresden, Germany 2019. Talk: Functionalization of gold nanoparticles with hydrophobic polymer ligands: Concepts for plasmon-emitter coupled systems.
- Conference of the European Colloid and Interface Society, Leuven, Belgium 2019. Poster: Functionalization of gold nanoparticles with hydrophobic polymer ligands: Concepts for plasmon-emitter coupled systems.

Contents

List of abbreviations

AFM	Atomic force microscopy
AIBN	2,2'-Azobis(2-methylpropionitrile)
APTMS	3-(Aminopropyl)-trimethoxysilane
ATRP	Atom-transfer radical polymerization
AUC	Analytical ultracentrifugation
AuNC	Gold nanocube
AuNP	Gold nanoparticle
AuNR	Gold nanorod
CPB	Concentrated polymer brush
CTA	Chain transfer agent
CTAB	Cetyltrimethylammonium bromide
CTAC	Cetyltrimethylammonium chloride
DBCO	Dibenzylcyclooctyne
DCA	Dicarboxyacetone
DDLS	Depolarized dynamic light scattering
DLS	Dynamic light scattering
DMF	N,N-Dimethylformamide
EDTA	Ethylenediaminetetraacetic acid
FFT	Fast Fourier transform
FJC	Freely jointed chain
IC	Ideal chain
ICP-OES	Inductively coupled plasma optical emission spectroscopy
LSPR	Localized surface plasmon resonance
MEK	Methyl ethyl ketone, 2-Butanone
NMP	Nitroxide-mediated polymerization
NMR	Nuclear magnetic resonance

NP	Nanoparticle
PDI	Polydispersity index
PMMA	Poly(methyl methacrylate)
PS	Polystyrene
PSD	Power spectral density
PTFE	Polytetrafluoroethylene
PVP	Poly(N-Vinylpyrrolidone)
RAFT	Reversible addition-fragmentation chain transfer
RMS	Root-mean-square
SANS	Small-angle neutron scattering
SAXS	Small-angle x-ray scattering
SCFT	Self-consistent field theory
SEC	Size exclusion chromatography
SDPB	Semi-dilute polymer brush
SLD	Scattering length density
SLS	Static light scattering
SPAAC	Strain promoted azide-alkyne cycloaddition
SWP	Square well potential
TEM	Transmission electron microscopy
TGA	Thermogravimetric analysis
THF	Tetrahydrofuran
TTC	Trithiocarbonate

1 Introduction

The vibrant red and purple colors of gold nanoparticles (AuNPs) and their application as colorant in glass manufacturing have been known for millennia.[1] Some evidence of the use of gold and other metal nanoparticles in glass staining survives to this day in the form of colorful church windows and ornate glassware.[2, 3] Nevertheless, an understanding of these optical phenomena and their physicochemical origin has only been enabled by analytical and computational methods developed in the past few decades.[4] In turn, this has spurred tremendous interest in the use of metal nanoparticles in materials science,[5–7] nano-optics,[8–10] sensing,[11–14] and medicine.[15–18] This work focuses on the preparation and characterization of polymer stabilized AuNPs with potential applications in functional nano-composites and nano-optic sensors.

Nanoparticles (NPs) are defined as particles with sizes between 1 and 100 nm.[19] As such, they are a subgroup of colloidal particles, which extend the size range to 1 µm.[20] The term NP is usually associated with more or less isotropic nanomaterials, for which the definition is met in all three dimensions. Other terms, such as nanorod, nanowire, and nanosheet, are applied to anisotropic nanomaterials that exhibit nanoscopic sizes in at least two dimensions or one dimension, respectively.

NPs fill the gap between the atomic and microscopic length scales, which has consequences for their properties. With sizes well below the diffraction limit for visible light, individual NPs cannot be resolved in conventional bright-field microscopy.[21] Already during the early days of colloid science, ultramicroscopy, a variation of optical dark-field microscopy, was developed to visualize NPs.[21] However, it still was incapable of resolving details, e.g. their shape or exact size. To achieve the resolution required to visualize such features, advanced imaging methods, such as electron microscopy,[22] super-resolution laser scanning microscopy,[21] and atomic force microscopy were developed.[23, 24] Another important set of methods that have enabled structural investigation of nanomaterials are scattering techniques.[25, 26] These typically use the scattering of light,[27, 28] x-rays, or neutrons to record intensity patterns or intensity fluctuations,[29, 30] which can then be related to structural parameters of the sample. As scattering patterns are reciprocal-space representations of real-space

structures, they are particularly suited to probe very small objects. Characteristic length scales, are on the order of $D \approx \lambda/2$, where λ is the wavelength of the radiation used.[31] Hence, visible light allows characterization of nano- and microscopic objects, whereas much shorter wavelength x-rays and neutrons can potentially achieve atomic resolution. This is demonstrated by the early use of the closely related method of x-ray diffraction to measure atomic length scales in crystallography.[32, 33] Because they rely on interference, scattering techniques require a certain degree of uniformity or periodicity in the sample in order to acquire meaningful data. In addition, scattering techniques usually involve extensive ensemble-averaging. On one hand, this allows for unmatched statistical reliability of the results. On the other hand, information on variations between particles within the sample is frequently lost. The combination of advanced imaging techniques and scattering methods eventually allowed detailed studies of the structure-property relationships in nanomaterials and boosted nanoscience as they became more widespread and affordable.

One consequence of the small dimensions of NPs is their high surface-to-volume ratio, which is inversely proportional to particle size.[34] This is even amplified by the fact that NPs are constructed of discrete atoms rather than consisting of infinitely fine, continuous matter, as demonstrated by the following examples. We consider a cube of N atoms on a primitive cubic grid. If $N = 1000$ atoms, the cube has an edge length of 10 atoms and the number of surface atoms is exactly 488 or 48.8% of all atoms in the cube. We now increase the edge length of the cube to 100 atoms, such that $N = 1,000,000$. In this case, the exact number of surface atoms is 58808 or 5.9% of all atoms in the cube. If we further increase the edge length to 1000 atoms, the cube now contains $N = 10^9$ atoms, of which 0.59% are surface atoms. The correlation between the edge length of the cube and the fraction of surface atoms is shown in **Figure 1**. Bearing in mind that the particle sizes corresponding to these examples roughly represent the full nanoscopic range, we can make two observations. Firstly, the number of atoms in a single NP can be very small, similar to that of large molecules, but increases rapidly with particle size. Secondly, small NPs comprise a large proportion of surface atoms, emphasizing the properties of the surface over those of the bulk material.

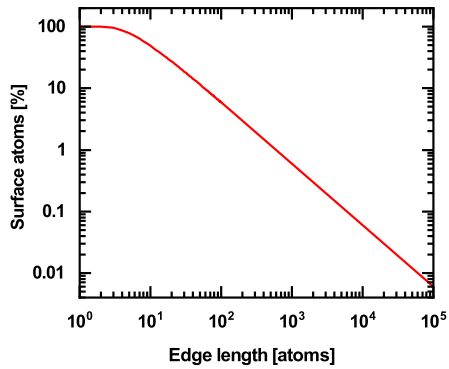

Figure 1: Correlation between the edge length of a cube of atoms and the corresponding fraction of surface atoms.

Their small size also has implications regarding the stability of NPs. Compared to macroscopic bulk materials, which are stabilized by internal lattice energies and cohesion forces, surface tension and van-der-Waals forces have a much greater influence.[35] The Laplace pressure, i.e. the pressure caused by surface tension acting on curved surfaces, is inversely proportional to the radius of curvature.[36] While promoting the isotropic, often spherical, shape of NPs, it also increases the internal energy of small, dispersed systems. A phenomenon related to the Laplace pressure and commonly observed in NPs is Ostwald ripening.[37] The Laplace pressure increases the chemical potential of surface atoms in small particles compared to larger ones. If there is a pathway of mass transport between particles, e.g. due to partial solubility, small particles will shrink in favor of large particles, which will grow in size. This concept is illustrated in **Figure 2**.

Ostwald ripening can be reduced by reducing the surface tension between NPs and the surrounding medium and by inhibiting mass transport.[38, 39] Both can be achieved by stabilizing agents. Stabilization of NPs is also required to overcome attractive van-der-Waals interactions between particles. Due to the small mass of NPs, these otherwise relatively weak forces are sufficiently strong to cause irreversible particle aggregation. A repulsive potential to prevent aggregation can be created by electrostatic or steric interactions.[35] The sum of attractive and repulsive forces creates a potential barrier between particles, that is usually finite in height. Thus, such NPs are

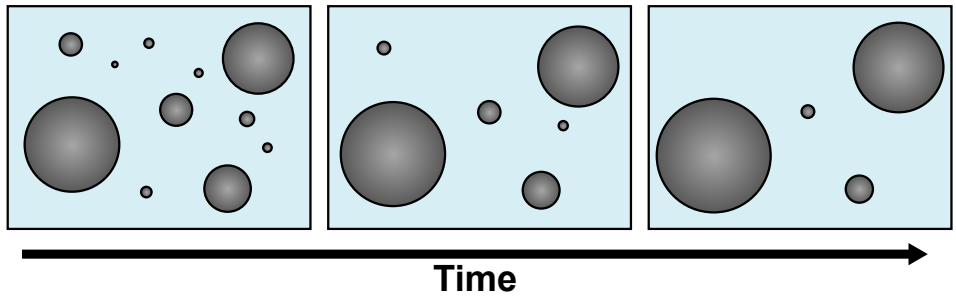

Figure 2: Schematic illustration of Ostwald ripening of solid particles. The Laplace pressure is higher for small particles than for large particles. Over time, small particles will shrink and ultimately disappear, while large particles increase in size.

only kinetically stabilized, rendering particle dispersions metastable. Changes in environmental parameters, for instance pH or ionic strength of the dispersing medium, can shift the force equilibrium and destabilize the dispersion. The most important strategies for the stabilization of NPs are shown in **Figure 3**.

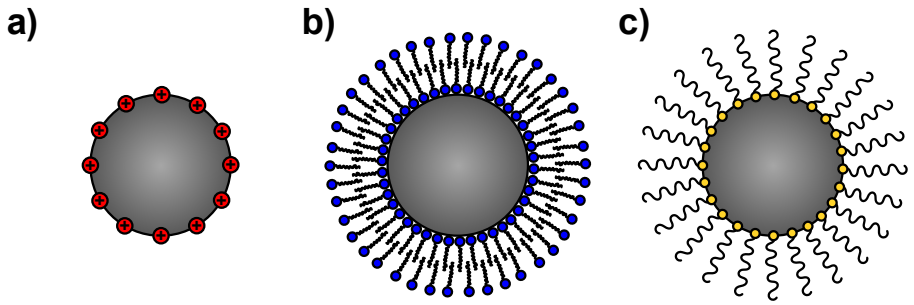

Figure 3: Examples of concepts for nanoparticle stabilization. a) Introduction of surface charges. b) Stabilization by surfactant bilayers. c) Stabilization by surface bound ligands.

One simple method to improve stabilization of NPs is a direct chemical or physical modification of the particle surface, which is generally aimed at introducing surface charges (**Figure 3 a**). Naturally, these processes often are specific to a given particle material. A more universal approach involves the use of surfactants as stabilizing agents, which adsorb to the particle surface or even form protective bilayers in order to reduce interfacial tension (**Figure 3 b**).[40, 41] Using anionic or cationic surfac-

tants with charged headgroups and nonpolar tails, electrostatic repulsion also provides stabilization against aggregation. AuNPs are frequently stabilized using the cationic surfactant cetyltrimethylammonium bromide (CTAB).[40, 42] Non-ionic surfactants may also be used, in which case stabilization is achieved via steric interactions.[43, 44] Finally, NPs can be stabilized by organic ligands, which are coordinated or covalently bound to the particle surface (**Figure 3 c**). The term ligand covers a broad range of not closely defined substances. Ligands can be small, multifunctional molecules,[45] end-functional hydrocarbon chains,[46, 47] linear or branched polymers,[48–52], and bio(macro)molecules.[53, 54] Depending on the type of ligand used, particle stabilization against aggregation can be electrostatic or steric. This variety renders the ligand approach very versatile and the properties of NPs can be controlled and fine-tuned by the choice of different ligands. For instance, ligands can be used to introduce surface charges in otherwise relatively inert materials, such as gold. They can also increase the compatibility with a dispersant or matrix and be used to promote specific binding events on the particle surface, which can be used for sensing. Polymeric ligands in particular can be tailor-made to fulfill a specific purpose.

Polymers are comprised of macromolecules, i.e., molecules with a high molecular mass.[55] Specifically, polymer molecules are macromolecules that are formed by a large number of identical or similar sub-units, called monomers. Polymers containing more than one type of monomer are called copolymers. Whereas the chemical nature of the monomers defines many properties of the polymers they form, some other typical properties of polymers, e.g., toughness and flexibility, are a result of their large size.[56] This size is usually expressed as the *degree of polymerization*, N, which is the number of monomer units in the chain. Importantly, synthetic polymers rarely contain chains with identical N, but rather a distribution of N. They are *polydisperse*. Polymer molecules can have varied structures, including linear chains, branched chains, stars, dendrimers, three-dimensional networks, and others.[57] Of these, linear homopolymers are the simplest and the most studied. **Figure 4** shows schematic examples of polymer molecules with $N = 31$ and different molecular architectures.

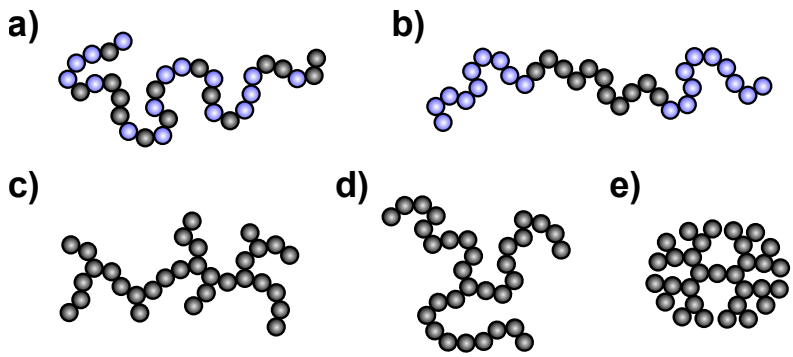

Figure 4: Examples of polymer architectures shown as beads on a string. Each bead represents a monomer unit, with all examples comprising $N = 31$ monomers. Different colors represent different types of monomer. a) Linear, statistical copolymer, b) linear, ABA tri-block copolymer, c) branched polymer, d) star polymer, e) dendrimer.

This thesis deals with the preparation and characterization of AuNPs that are sterically stabilized by hydrophobic polymer ligands in organic media. AuNPs typically are prepared and stabilized in aqueous media.[58–60] Although there are methods for the direct preparation of AuNPs in organic media,[61–63] the more common approach to obtain such particles is by a ligand driven phase transfer of particles from an aqueous to an organic phase.[47, 64, 65] During this process, a hydrophobic ligand is used to replace the ionic, hydrophilic ligands of AuNPs at the water/organic interface and thus promote a migration of particles into the organic phase. The phase transfer works reliably with small, strongly binding hydrophobic ligands in combination with small nanocrystals or spherical NPs. However, the phase transfer of large AuNPs and non-spherical AuNPs can be challenging.[66, 67] In addition, the reactive end groups of long polymer chains may not be as accessible as those of short chain ligands, which hinders the phase transfer process. In order to fully utilize the advantage of polymer ligands in terms of tunable functionality without affecting stability, a method that is inherently versatile and adaptable to a wide range of particle sizes and geometries, polymer materials, and functionality is required. One of the earlier approaches has been the direct functionalization of particles in water-miscible organic solvents.[68–70] In this method, a dispersion of gold or silver NPs is slowly added to a polymer solution in acetone or THF. A potential disadvantage of this method is the temporary

destabilization of particles, which requires high dilution in order to prevent aggregation before they are sufficiently functionalized with polymer. Indeed, precipitation of the particles during the grafting process has been reported.[68, 69] Another approach has been the functionalization of NPs with a temporary ligand in aqueous phase or by phase transfer, which can then be replaced by a polymer ligand in an organic phase.[71, 72] The main challenge of this process is to use a temporary ligand that sufficiently stabilizes NPs in organic media but can be replaced by other ligands. An interesting combination of different methods has been presented by the group of Liz-Marzán. In their approach the direct functionalization with a first, end-grafted polymer ligand in THF is followed by the addition of a second, amphiphilic polymer in the organic phase and a re-transfer to the aqueous phase.[66, 67]

For this thesis, linear, α,ω-functionalized polystyrene (PS) ligands with varying chain length will be grafted to AuNPs using a novel approach that combines the methods presented previously. PS is a well-characterized polymer that is soluble in a range of organic solvents. Moreover, α,ω-functionalized PS ligands with narrow molecular weight distributions are easily accessible by controlled polymerization techniques. The first part of the thesis focuses on the method used to prepare polymer stabilized AuNPs. In the second part of this thesis, the structure and properties of the polymer ligand shell on small, spherical AuNPs will be examined in detail, in particular with regard to the molecular weight and grafting density of the ligands. These findings will be compared to theoretical models describing polymer brushes, i.e., dense layers of polymer chains end-grafted to a solid surface. Finally, the kinetics of the binding process of α,ω-functionalized PS on the AuNP surface will be investigated.

2 Theoretical background

2.1 Thermodynamics of polymer solutions

This section deals with a brief overview of the thermodynamics of polymer solutions, in particular the *Flory-Huggins equation*.[56, 57] This fundamental equation describes the free energy of mixing, ΔF_{mix}, for polymer solutions and blends, although we will limit ourselves to polymer solutions here. The Flory-Huggins equation allows predictions regarding whether or not a polymer of a certain molecular weight will dissolve in a solvent at a given concentration and temperature. It also introduces a concept of *solvent quality*, i.e. how capable a solvent is of dissolving a specific polymer. Solvent quality has a major impact on the properties and conformations of polymers, as will be discussed in the following section. The Flory-Huggins equation has been derived from statistical considerations of polymers and solvent molecules on a lattice. This lattice can be two- or three-dimensional and can have different geometries. For sufficiently large lattice size, the resulting expressions will be equal. **Figure 5** shows an example of polymer chains on a two-dimensional lattice.

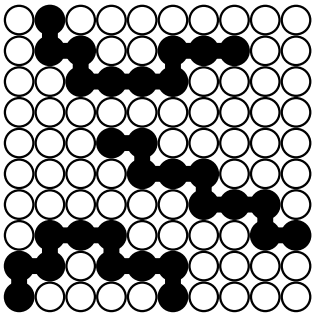

Figure 5: Example of a lattice representation of a polymer solution. Lattice sites occupied by polymer and solvent are shown in black and white, respectively. The lattice size is 10×10, the degree of polymerization is $N = 10$, and the polymer volume fraction is $\phi = 0.3$.

The fixed size of the grid is the reason for expressing the thermodynamics of mixing in terms of free energy (isochoric process) rather than free enthalpy (isobaric process), which is a reasonable approximation as the volume change for the dissolution of poly-

mers tends to be small.[73, 74] Equation 1 shows the Flory-Huggins equation, where N is the degree of polymerization, ϕ is the volume fraction of polymer, and χ is the Flory-Huggins interaction parameter.

$$\Delta F_{\mathrm{mix}} = k_{\mathrm{B}}T\Bigg[\underbrace{\frac{\phi}{N}\ln\phi + (1-\phi)\ln(1-\phi)}_{\Delta \mathrm{S}_{\mathrm{mix}}} + \underbrace{\chi\phi(1-\phi)}_{\Delta \mathrm{U}_{\mathrm{mix}}}\Bigg] \tag{1}$$

The first two terms in the square brackets correspond to the entropy of mixing, ΔS_{mix} and are similar to expressions found for the mixing of gases. However, the degree of polymerization has a major impact on the entropy gain during mixing. The first term decreases as N increases. As a result, the entropy of mixing is small for polymers, which typically have N in the order of 10^2 - 10^6. The last term in square brackets represents the energy of mixing, ΔU_{mix}, which has the major contribution to polymer solubility. The interaction parameter, χ, can be approximated by the use of tabulated solubility parameters, $\delta_{\mathrm{t,p}}$ and $\delta_{\mathrm{t,s}}$ of polymer and solvent respectively.

$$\chi \approx \frac{V(\delta_{\mathrm{t,p}} - \delta_{\mathrm{t,s}})^2}{k_{\mathrm{B}}T} \tag{2}$$

Here, V is the volume of a grid site or the typical volume of a monomer unit of the polymer in question. The concept of solubility parameters was first introduced by Hildebrand and is based on the heat of vaporization of a liquid.[75] For polymers, the values have to be estimated from structural analogies. As the Hildebrand model only accounts for non-polar interactions, it often fails for strong polar or specific interactions. A more refined system is that of Hansen solubility parameters.[76] Here, individual contributions of dispersion interactions, δ_{d}, polar interactions, δ_{p}, and hydrogen bonding, δ_{h}, are considered to define the total solubility parameter, δ_{t}, as shown in Equation 3.

$$\delta_{\mathrm{t}} = \sqrt{\delta_{\mathrm{d}}^2 + \delta_{\mathrm{p}}^2 + \delta_{\mathrm{h}}^2} \tag{3}$$

A stable solution will generally be obtained as long as the difference between solubility parameters of polymer and solvent is small. For good solvents, χ is small or

even negative. If $\chi > 0.5$, in the poor solvent regime, phase separation may occur, depending on T, ϕ, and N.[57] A special case are systems with $\chi = 0.5$, in which the net change of pairwise interaction energies between polymer segments and solvent upon polymer dissolution is zero.[57] This is referred to as θ *conditions* and a solvent which satisfies this condition is called θ *solvent*. Polymers in θ solvents have special properties, which will be discussed in the next section. In general, χ itself is a function of volume fraction and temperature.[57] As demonstrated by Equation 2, one would expect a $\chi \propto T^{-1}$ dependency. However, more complex behavior is often observed, leading to a wide variety of phase behavior of polymer solutions.[77]

2.2 Dimensions of polymer chains in solution

2.2.1 Conformational isomerism of polymer chains

The conformation of polymer chains in solution is tightly linked to the physical properties of the polymer solution. This section will discuss common models and quantities used to describe the dimensions of polymer chains. For the sake of simplicity and in the context of this thesis, only linear homopolymers with a continuous C–C backbone will be discussed. The large number of bonds within a typical polymer chain results in several differences between the solution behavior of polymers and small molecules. Each of the dihedral bond angles within a polymer chain follows a Boltzmann distribution, with the *trans* position as the most likely and the *cis* position as the least likely conformation. The two *gauche* positions represent local minima in the rotation potential, slightly higher in energy than the *trans* conformation. **Figure 6** shows a schematic energy curve in relation to dihedral angle. The exact energies of the conformers will depend on the substitution pattern. In n-butane for example, the energy barrier for a full rotation through the *cis* position is $\approx$ 20 kJ/mol, whereas the *gauche* positions are $\approx$ 4 kJ/mol higher in energy than the *trans* position.[78] Thus, bond rotation is possible over a wide range of angles at room temperature, but mostly restricted to the *trans* position and the two *gauche* positions.[79]

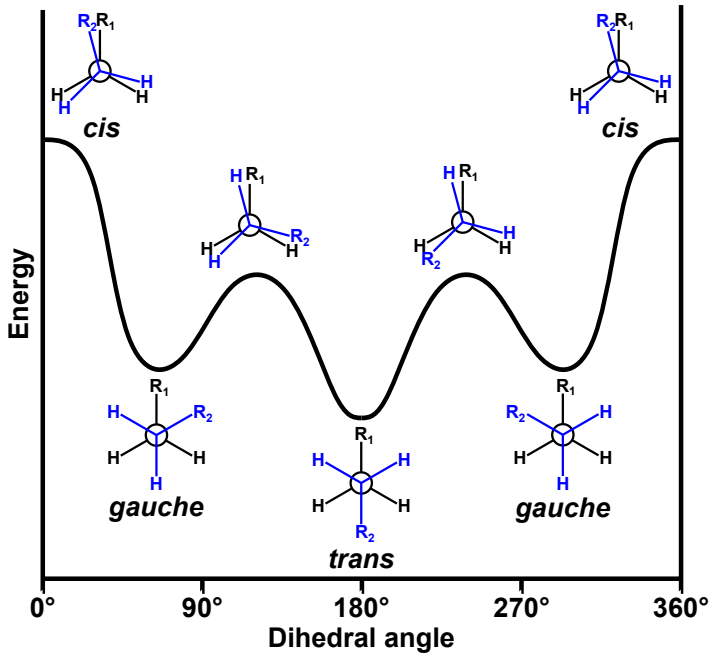

Figure 6: Schematic energy curve for the C-C bond rotation of a polymer chain segment. The conformations are shown from a perspective along the rotating C-C bond, with the black CH_2R_1 group at the back and the blue CH_2R_2 group in front. Eclipsed conformations are shown slightly offset for clarity.

As the number N of bonds within the polymer chain increases, there are more possible combinations for the overall conformation of the polymer chain. For sufficiently large N, the sum of bond rotation angles results in a continuous distribution of chain dimensions. This distribution also describes the segment density profile of a chain in solution, i.e. how the chain segments are distributed relative to the center of the coil. The distribution of chain dimensions is identical for the ensemble average of many chains and time average of a single chain. This property of polymer chain statistics is called *ergodicity* and it is relevant in both experimental and theoretical contexts.[77] For example, experiments involving a time averaged measurement will also give us information about the ensemble average and vice versa. Moreover, theoretical models can utilize both ensemble and time averaged methods, for instance Monte Carlo (ensemble average) and molecular dynamics (time average), to come to identical results.

2.2.2 Ideal polymer chains

The most simplistic model system to describe the conformation of a polymer chain is the *freely jointed chain* (FJC). In this model, the chain is represented by N segments of fixed length l that are linked together without restrictions to the angle between adjacent segments. This is shown in **Figure 7**. The segments have no volume and can overlap. The end-to-end vector, $\vec{s}$, of the chain is the sum of segment vectors $\vec{r}_\mathrm{i}$ with $|\vec{r}_\mathrm{i}| \equiv l$. The magnitude $|\vec{s}| \equiv s$ is called *end-to-end distance*.[57]

$$\vec{s} = \sum_{\mathrm{i}=1}^{N} \vec{r}_\mathrm{i} \tag{4}$$

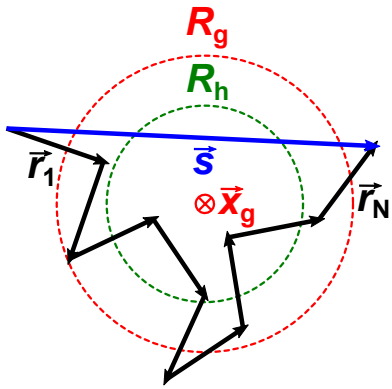

Figure 7: Representation of a polymer chain as series of bond vectors, $\vec{r}_\mathrm{i}$. The end-to-end vector, $\vec{s}$, is shown in blue. The center of mass, $\vec{x}_\mathrm{g}$, and the radius of gyration, R_g, are shown in red. The hydrodynamic radius, R_h is shown in green.

As there are no restrictions of bond angles, the FJC is equivalent to a random walk with N steps in three dimensions. For large N or averaged over a large number of chains, the expected value $\langle s \rangle$ will approach zero.

$$\langle s \rangle = \left| \lim_{\mathrm{N}\to\infty} \sum_{\mathrm{i}=1}^{N} \vec{r}_\mathrm{i} \right| = 0 \tag{5}$$

Therefore, the *mean-square end-to-end distance* $\langle s^{\,2} \rangle$ is often used as a non-zero ensemble average instead.

$$\langle s^2 \rangle_{\mathrm{FJC}} = \sum_{\mathrm{i}=1}^{N} (\vec{r}_{\mathrm{i}} - \langle \vec{r} \rangle)^2 = \sum_{\mathrm{i}=1}^{N} \vec{r}_{\mathrm{i}}{}^2 = Nl^2 \tag{6}$$

From the root-mean-square (RMS) end-to-end distance we finally obtain the relation commonly known as $\sqrt{N}$ law.

$$\sqrt{\langle s^2 \rangle}_{\mathrm{FJC}} = \sqrt{N} l \tag{7}$$

This scaling law is frequently used to approximate polymer chains by a simple mathematical expression. However, it does not account for the fixed bond angles and restricted bond rotation of real molecules. Thus, deviations from the FJC model can be substantial, in particular for polymers with high molecular weights or bulky monomer side groups. By including a chain expansion factor, the *ideal chain* (IC) model describes the true dimensions of polymer chains following random walk statistics. In an experimental context, the total chain expansion is frequently described in terms of the *characteristic ratio*, C, between the true mean-square end-to-end distance and the FJC model. The characteristic ratio depends on the degree of polymerization. For sufficiently large N, it becomes constant and is denoted as C_∞.[57]

$$\left. \frac{\langle s^2 \rangle}{\langle s^2 \rangle_{\mathrm{FJC}}} \right|_{\mathrm{N} \gg 1} = \left. \frac{\langle s^2 \rangle}{Nl^2} \right|_{\mathrm{N} \gg 1} = C_\infty \tag{8}$$

$$\langle s^2 \rangle_{\mathrm{IC}} = Nl^2 C_\infty \tag{9}$$

The characteristic ratio is specific to a polymer/solvent pair in θ conditions and is a measure for the stiffness of a polymer chain. The higher C_∞, the lower the flexibility of the chain along the backbone. A popular alternative formalism for the expanded ideal chain is given by the *Kuhn* equivalent chain. This model constructs an ideal chain from a random walk of N_K Kuhn segments with the Kuhn length l_K, which are chosen in a way that Equation 10 is satisfied.

$$\langle s^2 \rangle_{\mathrm{IC}} = N_\mathrm{K} {l_\mathrm{K}}^2 \tag{10}$$

From a comparison of coefficients between Equations 9 and 10 we can deduce that $N_\mathrm{K} = \frac{N}{C_\infty}$ and $l_\mathrm{K} = lC_\infty$. Similarly to the characteristic ratio, the Kuhn length is a common measure for the stiffness of a polymer chain.

Although $\langle s^2 \rangle$ can be obtained experimentally in some cases, a more directly measurable quantity describing the size of a polymer chain in solution is the *radius of gyration*, R_g. It is derived from the distribution of mass within the polymer coil. In the chain representation in **Figure 7**, the mass is located at the nodes of the segments. For N segments, there are $N+1$ nodes. With $\vec{x}_\mathrm{i}$ as the position of the i-th node and $\vec{x}_\mathrm{g}$ as the position of the center of gravity of the chain, R_g can be calculated according to Equation 11.

$$R_\mathrm{g}{}^2 = \frac{1}{N+1} \sum_{\mathrm{i}=0}^{N} (\vec{x}_\mathrm{i} - \vec{x}_\mathrm{g})^2 \tag{11}$$

It can be shown that $\langle s^2 \rangle$ and $\langle R_\mathrm{g}{}^2 \rangle$ are directly proportional.[57]

$$\langle s^2 \rangle = 6 \langle R_\mathrm{g}{}^2 \rangle \tag{12}$$

This relation is very helpful, since we can obtain values for R_g from scattering techniques, which we can then translate into end-to-end distances.

The radius of gyration is usually obtained from static scattering methods, such as static light scattering (SLS) and small angle neutron scattering (SANS). However, dynamic light scattering (DLS) can also be used to obtain a size measure for polymer chains, which is called the *hydrodynamic radius* R_h. It determines the velocity at which the polymer chain or other small object moves through a viscous medium. The hydrodynamic radius is the radius of a sphere with the same diffusion coefficient as the object. Since polymers in solution are not dense spheres and therefore experience little hydrodynamic drag, we can expect that R_h will be much smaller than the actual dimensions of the chain. From considerations based on the hydrodynamic interaction between particles, R_h of a polymer chain has been derived as

$$\frac{1}{R_\mathrm{h}} = \left\langle \frac{1}{|\vec{x}_\mathrm{i} - \vec{x}_\mathrm{j}|} \right\rangle_{\mathrm{i} \neq \mathrm{j}} \tag{13}$$

where $\vec{x}_\mathrm{i}$ and $\vec{x}_\mathrm{j}$ are positions of mass points or monomer units along the chain. For the FJC model, we obtain the following expression.[77]

$$R_\mathrm{h} = \sqrt{\frac{3\pi}{128}}\sqrt{N}l \approx 0.271\sqrt{N}l \tag{14}$$

As expected, R_h is much smaller than $\sqrt{\langle s^2 \rangle}$ and R_g.

2.2.3 Real polymer chains

Real polymer chains differ from the ideal chain models discussed so far due to their molecular volume and additional interactions that have to be taken into consideration as a result. These interactions often are referred to as *long-range interactions*. This terminology is misleading, as the forces involved do not act over particularly long distances. Instead, the term *long-range* is related to the distance between segments along a chain, which are affected by these interactions. In this context, *short-range* refers to interactions between adjacent chain segments, i.e. restrictions to bond angles and rotation. The change to the conformation and properties of polymers in solution due to long-range interactions is called *excluded volume effect*. Despite its name, the excluded volume, v, is only loosely related to the monomer or chain segment dimensions. Instead, it can be understood as a volume difference between space dominated by repulsive and attractive interactions, respectively.[57] As a result, the excluded volume will assume negative values, if attractive interactions outweigh repulsion. This is the case for polymer chains in poor solvents. In good solvents, the excluded volume is positive, resulting in chain expansion beyond ideal chain dimensions. Due to its origin in polymer-polymer interactions, the excluded volume is related to important thermodynamic quantities, such as the second virial coefficient, A_2, and the Flory-Huggins interaction parameter, χ, which was already introduced in the previous section. Equation 15 shows the theoretical relation between v and χ in context of the Flory theory.[57]

$$\mathrm{v} = (1 - 2\chi)l^3 \tag{15}$$

Here, l^3, i.e. the cube of the monomer length, represents a coarse, spherical approx-

imation of the monomer volume. In many cases, the dimensionless excluded volume parameter, $\mathrm{v}/l^3 = 1 - 2\chi$, is used instead, deleting the necessity for an accurate value for the monomer volume. Notably, the excluded volume vanishes for $\chi = 0.5$, which corresponds to θ conditions and results in ideal, random walk chain statistics. With $\mathrm{v} \neq 0$, the chain can no longer be described by a random walk, as chain segments interact. They are no longer allowed to occupy the same volume, which is why the conformation of real chains also is referred to as *self-avoiding walk*. A first, simple derivation of the chain statistics of real chains in good solvents was presented by Flory. Equation 16 shows his estimation of the total free energy of a real chain in a good solvent, where s is the end-to-end distance of the chain.

$$F = k_\mathrm{B}T\left(\mathrm{v}\frac{N^2}{s^3} + \frac{s^2}{Nl^2}\right) \tag{16}$$

The first term in the brackets corresponds to the internal energy contribution, whereas the second term corresponds to the entropic contribution. F has a minimum regarding s, which determines the most likely end-to-end distance, s_F. The derivative of F is shown in Equation 17.

$$\frac{\partial F}{\partial s} = k_\mathrm{B}T\left(-3\mathrm{v}\frac{N^2}{s^4} + 2\frac{s}{Nl^2}\right) \tag{17}$$

We solve for $s = s_F$ at the minimum of F, i.e. $dF/ds = 0$.

$$s_F \approx \mathrm{v}^{1/5}N^{3/5}l^{2/5} \tag{18}$$

Comparing the Flory result for s_F with ideal chain scaling, we find that the end-to-end distance scales with $N^{3/5}$ rather than $N^{1/2}$, reflecting the departure from random walk statistics. Although Flory's approach was flawed due to inaccurate estimation of energetic and entropic contributions, his result for the scaling exponent is in good agreement with later numerical calculations as well as experimental data.[57, 77] In practice, more generalized scaling laws with ν as the so-called Flory exponent are often used. The RMS end-to-end distance of a real chain, $\sqrt{\langle s^2\rangle}_\mathrm{RC}$, therefore satisfies Equation 19 in any solvent, where b is the statistical segment length.

$$\sqrt{\langle s^2 \rangle}_{\mathrm{RC}} = N^{\nu} b \tag{19}$$

Akcasu et al. expanded this generalized scaling law with expressions for $R_{\mathrm{g,RC}}$ and $R_{\mathrm{h,RC}}$.[80]

$$R_{\mathrm{g,RC}} = \frac{1}{\sqrt{2(\nu+1)(2\nu+1)}} N^{\nu} b \tag{20}$$

$$R_{\mathrm{h,RC}} = \frac{\sqrt{6\pi}}{12}(2-\nu)(1-\nu) N^{\nu} b \tag{21}$$

Using this set of relations, the scaling of polymer chains can be determined by measuring either $\langle s^2 \rangle$, R_{g}, or R_{h}, using various methods. The found parameters can then be used to calculate any of the other measures of chain dimensions, that may not be accessible experimentally. Importantly, the scaling exponent itself remains unchanged, regardless of the experimental method used, and can be directly extracted from a set of data without conversion of the experimental quantity into a different measure of chain dimension.

2.3 Dimensions of polymer chains at surfaces

2.3.1 Flat surfaces

The conformation and dimensions of polymers attached to surfaces by one chain end can differ significantly from those of polymers in solution. In addition to parameters such as degree of polymerization, chain flexibility and solvent quality, the conformation of attached chains also depends on the grafting density, σ, i.e. the number of chains attached per surface area and the curvature of the surface.[81] At high grafting densities, a strong influence of the excluded volume effect can be expected. High surface curvature results in a stronger excluded volume effect for chain segments near the surface, whereas segments far from the surface are less affected. Furthermore, the restriction of space in one direction by the substrate must inevitably change the scaling statistics. At low grafting densities, polymer chains attached to a surface retain their scaling statistics, independent of σ. However, as only half the space surrounding the

attached chain end is accessible, their dimensions are approximately twice of those of a free chain in solution.[81] This situation is referred to as dilute or *mushroom* regime, as shown in **Figure 8 a**. At grafting densities of $\sigma \geq \langle s \rangle^{-2}$ the chains start to interact and stretch. Such densely packed structures of stretched, end-grafted polymer chains are called *polymer brushes*. At intermediate grafting densities, they behave similarly to semi-dilute polymer solutions and are therefore called *semi-dilute polymer brush (SDPB)*. **Figure 8 b** illustrates a SDPB on a flat surface. At even higher grafting densities, chain interactions begin to dominate the brush structure, often leading to significant chain stretching. This scaling regime is referred to as *concentrated polymer brush (CPB)*.[81]

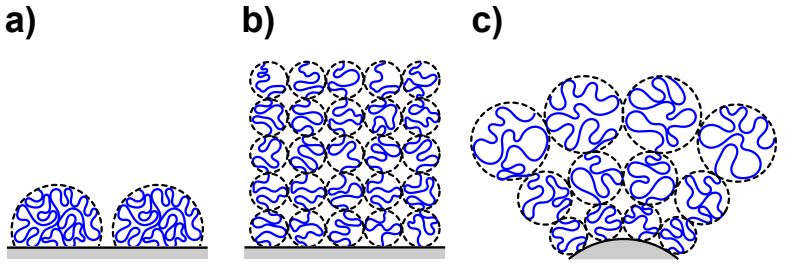

Figure 8: a) Dilute polymer brush in the *mushroom* regime. b) Semi-dilute brush on a flat surface. c) Semi-dilute brush on a spherical surface. The correlation blobs are indicated as dashed lines around the solid blue polymer chains.

The scaling theory for polymer brushes was pioneered by Shlomo Alexander and Pierre-Gilles de Gennes and has since been refined and expanded by others.[82, 83] To understand the brush structure in the SDPB regime, it is helpful to divide the polymer chains into smaller subsections, usually referred to as *blobs*. The chains within these blobs follow the same statistics as the corresponding unperturbed chain. The size of the blobs is determined by system parameters, such as temperature, polymer concentration, and mechanical stress. The relevant parameter that determines the blob size of end-grafted chains is the local volume fraction or segment density. Such blobs are also termed *correlation blobs*.[57] The blob size, ξ, is analogous to the end-to-end distance of a chain with g segments of length b.[57]

$$\xi \approx b g^{\nu} \tag{22}$$

The volume fraction, ϕ, of polymer within each blob can be approximated as

$$\phi \approx \frac{g b^3}{\xi^3} \tag{23}$$

At semi-dilute concentrations, the solution volume is filled with densely packed correlation blobs. This allows us to estimate the correlation blob size.

$$\xi \approx b \phi^{-\nu/(3\nu-1)} \tag{24}$$

This relation will become important for chains grafted to a curved surface. For chains grafted to a flat surface, this expression greatly simplifies, as the volume fraction is approximately constant and defined by the surface area or footprint available per chain.

$$\xi \approx \sigma^{-1/2} \tag{25}$$

Since $\xi = b g^{\nu}$, the number of monomer segments per blob is

$$g \approx \left(\frac{\xi}{b}\right)^{1/\nu} = \sigma^{-1/(2\nu)} b^{-1/\nu} \tag{26}$$

The flat brush of height H_0 is formed by a chain of $n = N/g$ blobs of size ξ.[57]

$$H_0 \approx \xi \frac{N}{g} \approx N \sigma^{(1-\nu)/(2\nu)} b^{1/\nu} \tag{27}$$

For $\nu = 3/5$, i.e., good solvent conditions, we obtain

$$H_0 \approx N \sigma^{1/3} b^{5/3} \tag{28}$$

and for $\nu = 1/2$, i.e. θ conditions we obtain

$$H_0 \approx N \sigma^{1/2} b^2 \tag{29}$$

2.3.2 Curved surfaces

For polymer brushes on curved surfaces, the chains are more confined near the surface than they are at a greater distance from it, as shown in **Figure 8 c**. Consequently, the volume fraction of polymer tends to decrease as the distance, z, from the surface increases. Compared to polymer brushes on flat surfaces, this allows for a complex variety of brush structure and scaling behavior.[81, 84, 85] Within this broad range, two extreme cases stand out; locally flat brushes and the star polymer limit. As the name implies, locally flat brushes can mostly be treated like Alexander-de Gennes brushes, discussed previously. This approximation is legitimate, if the radius of surface curvature is large and the polymer chains are relatively short, resulting in a negligible change of polymer volume fraction throughout the brush. In contrast, brushes in the star polymer limit comprise relatively long polymer chains on surfaces with a small radius of curvature. This situation leads to a highly divergent polymer volume fraction profile, similar to that of star polymers.[84] Spherical brushes that are neither locally flat nor in the star polymer limit can exhibit complex volume fraction profiles and transitions between different scaling regimes.[81, 85] Approaches based on self-consistent field theory (SCFT) or molecular dynamics have been used to investigate the scaling behavior of such transitional brushes.[85, 86]

In the following, the impact of surface curvature, grafting density, and solvent quality on brush scaling will be discussed. This discussion will focus on the star polymer limit, as it is the most relevant for this thesis and allows for simple, analytical approximations. The volume fraction profile for a brush in the star polymer limit is given by Equation 30, where R is the radius of curvature of the grafting surface, z is the distance from the surface, and d is the dimension of curvature, with $d = 1$ for a flat surface, $d = 2$ for cylinders, and $d = 3$ for spheres.[85]

$$\phi(z) = (\sigma b^2)^{(3\nu-1)/(2\nu)} \left(\frac{R}{R+z}\right)^{(d-1)(3\nu-1)/(2\nu)} \tag{30}$$

For spherical grafting surfaces, the polymer volume fraction scales approximately as z^{-1} in θ solvents and $z^{-4/3}$ in good solvents. Inserting this expression into the concentration-dependent size of correlation blobs (Equation 24), we obtain the

distance-dependent blob size $\xi(z)$.

$$\xi(z) \approx \sigma^{-1/2} \left(\frac{R+z}{R} \right)^{(d-1)/2} \tag{31}$$

For $d = 1$, we obtain the same result as in Equation 25. For $d = 3$, i.e. a brush on a spherical surface, ξ increases linearly with increasing distance from the surface and increases with decreasing radius of curvature. Notably, the blob size does not depend on solvent quality. The height of the brush in the star polymer limit can be approximated using a similar approach to the one shown in Equation 27 or solved analytically from the volume fraction profile.[84] In good solvents, the height, H, of a curved brush scales as shown in Equation 32, which differs from the corresponding height of a flat brush, H_0 by an additional exponent of 3/5.[81, 84]

$$H \propto N^{3/5} \sigma^{1/5} \propto H_0^{3/5} \tag{32}$$

In θ solvents, the scaling changes to Equation 33, linked to the flat brush height by an exponent of 1/2.[81, 84, 87]

$$H \propto N^{1/2} \sigma^{1/4} \propto H_0^{1/2} \tag{33}$$

We can therefore postulate a universal scaling law according to Equation 34.

$$H \propto N^{\nu} \sigma^{(1-\nu)/2} \propto H_0^{\nu} \tag{34}$$

At high grafting densities, as the probability of polymer-polymer contacts becomes comparable to that of polymer-solvent contacts, the effect of excluded volume decreases and higher order interactions between chains begin to dominate. As a result, chain statistics are now ideal, irrespective of the solvent conditions and the influence of σ is more pronounced, as shown in Equation 35.[81, 84, 88]

$$H \propto N \sigma^{1/2} \tag{35}$$

The absolute values for the brush height depend on, chain flexibility, excluded vol-

ume, and the curvature of the grafting surface. All three parameters influence the volume density profile, which can be solved by SCFT calculations. The different scaling regimes for flat and curved brushes in good and θ solvents are summarized in **Table 1**.

Table 1: Scaling relations for flat and curved brushes in good and θ solvents.

regime	good solvent		θ solvent	
	flat	curved	flat	curved
mushroom	$N^{3/5}$		$N^{1/2}$	
semi-dilute	$N\sigma^{1/3}$	$N^{3/5}\sigma^{1/5}$	$N\sigma^{1/2}$	$N^{1/2}\sigma^{1/4}$
concentrated	$N\sigma^{1/2}$			

2.4 Dynamic light scattering

Dynamic light scattering (DLS) is one of the principal methods used in this thesis. In DLS, the intensity fluctuations of light, elastically scattered by a sample, are analyzed to determine the diffusion coefficients of scattering objects, e.g. particles and polymer coils. From the translational diffusion coefficient, D_t, the hydrodynamic radius, R_h, of the object can be calculated using the Stokes-Einstein equation. Unlike static light scattering (SLS), which relies on average scattering intensities and therefore refractive index contrast, DLS is not as sensitive towards complex structures of scattering objects, e.g. core-shell morphologies with a large refractive index contrast between core and shell. DLS on the other hand requires a good understanding of the overall shape of the objects (spherical, rod-like, fractal,...) in order to obtain meaningful size information.

Intensity fluctuations are an inherent characteristic of light scattering measurements. They originate from local refractive index fluctuations which are caused by motion (usually translation and rotation) of molecules and dispersed particles in the sample. The faster the motion, the shorter the decay time of the intensity fluctuations will be. Experimentally, this decay is analyzed by means of an *intensity-time autocorrelation function*, $g^{(2)}(\tau)$, which compares the intensity at a certain point in time, $I_\mathrm{sc}(t)$, with the intensity at a later point in time, $I_\mathrm{sc}(t+\tau)$, as shown in Equation 36.[89, 90]

$$g^{(2)}(\tau) = \frac{\langle I_\mathrm{sc}(t)\, I_\mathrm{sc}(t+\tau)\rangle}{\langle I_\mathrm{sc}\rangle^2} \tag{36}$$

This operation is repeated in real time and for a large number of delay times, τ, by a hardware autocorrelator. $g^{(2)}(\tau)$ is linked to the *field-time autocorrelation function*, $g^{(1)}(\tau)$, by the modified Siegert relation, shown in Equation 37.[91] Here, B is a baseline parameter (ideally $B = 1$) and β is the intercept, a measure for signal quality.

$$g^{(2)}(\tau) = B + \beta \left[g^{(1)}(\tau)\right]^2 \tag{37}$$

For a monodisperse sample, $g^{(1)}(\tau)$ is a simple exponential decay with a mean decay constant, $\overline{\Gamma}$. Real samples usually possess some degree of polydispersity, which can be

approximated by a series expansion. The coefficients μ_n are called the n^{th} *cumulant*, hence this approach is called *cumulant method*. One method for the cumulant analysis of experimental intensity-time autocorrelation functions has been described by Barbara Frisken and is shown in Equation 38.[92] The main advantages of the Frisken method are a higher fidelity and the possibility to apply the fit to the full data range, rather than a manually defined sub-range, which facilitates automated data processing.

$$g^{(2)}(\tau) = B + \beta \exp(-2\overline{\Gamma}\tau)\left(1 + \frac{\mu_2}{2}\tau^2\right)^2 \tag{38}$$

The polydispersity can be calculated from the second cumulant and the mean decay rate.[90]

$$\mathrm{PDI} = \frac{\mu_2}{\overline{\Gamma}^2} \tag{39}$$

For a Gaussian size distribution, the PDI is also defined by Equation 40, where σ is the standard deviation of R_h.[93]

$$\mathrm{PDI} = \frac{\sigma^2}{R_\mathrm{h}^2} \tag{40}$$

For greater accuracy, autocorrelation functions can be obtained at multiple scattering angles, θ. In the case of purely translational diffusion, D_t can be obtained as the slope from a plot of $\overline{\Gamma}$ versus the squared magnitude of the scattering vector, q.

$$\overline{\Gamma} = q^2 D_\mathrm{t} \tag{41}$$

The scattering vector and its magnitude are defined as

$$\vec{q} = \vec{k}_\mathrm{sc} - \vec{k}_0 \tag{42}$$

$$q = \frac{4\pi n}{\lambda} \sin\left(\frac{\theta}{2}\right) \tag{43}$$

where $\vec{k}_\mathrm{sc}$ and $\vec{k}_0$ are the wave vectors of scattered and incident light respectively, n is the refractive index, and λ is the wavelength of incident light. From the Stokes-

Einstein equation, R_h can then be calculated from D_t, as shown in Equation 44. Here, η is the dynamic viscosity of the medium.

$$R_\mathrm{h} = \frac{k_\mathrm{B}T}{6\pi\eta D_\mathrm{t}} \tag{44}$$

Most DLS measurements are performed using polarized light with the polarization plane of incident and detected light perpendicular to the plane opened by θ. This is also referred to as *vv*-geometry. Anisotropic objects, such as particle dimers possess different polarizability along and perpendicular to their main axis. If struck by linearly polarized light, anisotropic objects scatter differently, depending on their orientation relative to the polarization plane of incident light. As a dipole moment will be induced most efficiently along the axis with the highest polarizability, the polarization plane of scattered light is rotated, which is called depolarization. Consequently, anisotropic objects that are able to depolarize light upon scattering contribute to the scattering intensity measured with crossed polarizers (*vh*-geometry). Such experiments are termed *depolarized* DLS or DDLS. As the intensity fluctuations now depend on translation as well as rotation of the objects, the rotational diffusion coefficient, D_r can be determined. In this case, the angle-dependent mean decay rate is given by

$$\overline{\Gamma} = q^2 D_\mathrm{t} + 6D_\mathrm{r} \tag{45}$$

2.5 Small angle x-ray scattering

Small angle x-ray scattering (SAXS) is a scattering technique based on the electron density difference between elements. As a rule of thumb, the electron density, ρ_e, increases with atomic number. Consequently, SAXS is particularly suited for measurements on inorganic or inorganic/organic composite samples. Although measurements of purely organic samples are possible, high photon flux (i.e. synchrotron x-ray) or long acquisition times are required.[29] In most experiments, SAXS is employed to obtain time- and ensemble-averaged, two- or one-dimensional angle-dependent intensity profiles. Although the angular range is not strictly defined, SAXS measurements are usually limited to scattering angles of $\theta < 10°$. The corresponding scattering vector

or q-range is sufficient to resolve features with sizes from 1 nm to 1 µm. As shown in Equation 46, the measured intensity as a function of q is the sum of coherent and incoherent intensity contributions, I_{coh} and I_{inc} respectively.

$$I(q) = I_{\mathrm{coh}}(q) + I_{\mathrm{inc}}(q) \tag{46}$$

Whereas the incoherent term can be considered as undesired background, the coherent term contains information on size, shape, structure, and concentration of the sample material. The contributions to $I_{\mathrm{coh}}(q)$ are shown in Equation 47, where N is the number of scatterers, V is the volume of each scatterer, $\Delta\eta$ is the scattering length density (SLD) contrast, $P(q)$ is the form factor, and $S(q)$ is the structure factor.[25]

$$I_{\mathrm{coh}}(q) = NV^2\Delta\eta^2 P(q)S(q) \tag{47}$$

The SLD can be calculated from the chemical composition and density of a material and the SLD contrast is simply the difference of SLD of the various components within the sample, e.g. particles dispersed in a liquid. The form factor, $P(q)$, is a characteristic function describing the angle dependence of the scattered intensity in relation to the shape and size of a scattering object. Some of these form factors are analytical functions, whereas others have to be modeled numerically. The most prominent form factor, which is also used in this thesis, is the form factor for a sphere with radius R, shown in Equation 48.[25]

$$P(q) = \left[3\frac{\sin(qR) - qR\cos(qR)}{(qR)^3}\right]^2 \tag{48}$$

The structure factor, $S(q)$, describes the angle dependence of scattered intensity in relation to superstructures formed by multiple scattering objects. It represents a Fourier transform of the pair correlation function of scatterers and $S(q) \approx 1$ for dilute or uncorrelated samples. In this thesis, a structure factor derived from a square well potential (SWP) is used. The SWP is a simplistic approximation of a Lennard-Jones potential and is defined as shown in Equation 49, where σ is the hard sphere diameter (i.e. $\sigma = 2R_{\mathrm{HS}}$), ϵ is the well depth, and Δ is the well width.

$$U(r) = \begin{cases} \infty & \text{for} \quad 0 < r < \sigma \\ -\epsilon & \text{for} \quad \sigma < r < \sigma + \Delta \\ 0 & \text{for} \quad r > \sigma + \Delta \end{cases} \tag{49}$$

The analytical solution for $S(q)$ corresponding to this potential has been derived by R.V. and K.V. Sharma [94].

2.6 Analytical ultracentrifugation

Analytical ultracentrifugation (AUC) is a method pioneered by Theodor Svedberg, in which the sedimentation of particles and large molecules during centrifugation is monitored to gather information about the size, shape, or density of the sample material.[95] AUC can be used in a wide variety of modes, the most prominent being *sedimentation equilibrium* and *sedimentation velocity* experiments.[96] In sedimentation equilibrium experiments, the radial concentration profile within the sample is analyzed after an equilibrium between sedimentation and back-diffusion has been reached. These experiments are particularly useful to determine the molecular weight distribution of large molecules, such as proteins. In sedimentation velocity experiments, the transient concentration profiles for a complete sedimentation process are analyzed.[97] Thus, the molar mass, density, or diffusion coefficient of molecules and particles with a wide range of weights and sizes can be obtained, depending on which of the quantities are already known. Within this thesis, only sedimentation velocity experiments were performed. **Figure 9** schematically illustrates an AUC experiment. The rotor of the centrifuge is shown in top view in **a** and in side view in **b**.

Sample chambers are set into the rotor. Unlike conventional UV/Vis cells, these sample chambers are trapezoidal to minimize the distortion of sedimentation near the walls of the cells. The rotor is placed within a spectrometer setup. For transmission or absorbance experiments, this spectrometer consists of a flash lamp or other suitable light sources and a detection unit, which also contains a monochromator. The spectrometer is synchronized to the rotation of the rotor and measurements are performed when the sample chambers pass through the light path. In order to obtain radial transmission

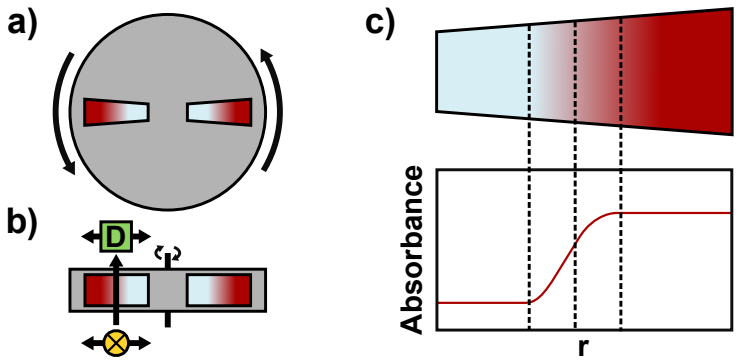

Figure 9: Illustration of a typical AUC experiment with transmission detection. a) Top view of a rotor with two sample chambers. b) Side view of the rotor, illustrating the radially movable detection optic. c) Example of a radial absorbance profile, showing the sedimentation front as a step in absorbance.

or absorbance profiles, the spectrometer can be moved radially, scanning through the length of sample chamber. A schematic example of a radial absorbance profile for the sedimentation of AuNPs is shown in **Figure 9 c**. The sedimentation front is seen as a step in the radial absorbance curve. For sedimentation processes with negligible diffusion, the sedimentation front can be sharp throughout the entire process, whereas the sedimentation front becomes more blurry over time for processes with significant diffusion. The resolution are limited by the speed of rotation, the sample frequency of the spectrometer, and the time scale of the process to be observed. Basis for the analysis of measured concentration profiles is the *Lamm equation* shown below.[96]

$$\frac{\partial c}{\partial t} = -\frac{1}{r}\frac{\partial}{\partial r}\left[cs\omega^2 r^2 - D_\mathrm{t}\frac{\partial c}{\partial r}r\right] \tag{50}$$

This inhomogeneous differential equation fully describes the time and radius dependent concentration in relation to angular frequency, ω, diffusion coefficient, D_t, and sedimentation coefficient, s. It can only be solved numerically, unless very strict boundary conditions are introduced, e.g. equilibrium conditions ($\partial c/\partial t = 0$). The algorithm of the software SEDFIT used in this thesis uses a finite difference approach to obtain a distribution $c(s)$ of sedimentation coefficients.[98] The sedimentation coefficient is a normalized measure of the sedimentation velocity, v, as shown in Equation 51. It has

the dimension of time and is usually given in the unit Svedberg, S = 10^{-13} s.

$$s = \frac{v}{\omega^2 r} \tag{51}$$

For a compact, spherical particle, the sedimentation coefficient can be expressed as a function of R_h, η, and the densities of particle and solvent, ρ_part and ρ_solv, respectively.

$$s = \frac{2{R_\mathrm{h}}^2(\rho_\mathrm{part} - \rho_\mathrm{solv})}{9\eta} \tag{52}$$

If either R_h or ρ_p are known, the other quantity can be determined, assuming that the solvent properties (η and ρ_s) are known as well. Since R_h is also accessible through DLS measurements, sedimentation velocity experiments can be used to determine the average density of particles.

2.7 Optical properties of gold nanoparticles

The unusual optical properties of small gold particles are the result of phenomena that occur in all metals but only manifest themselves in such a fascinating manner in a few of them.[99] Although similar effects can be observed for bulk metals, we will limit ourselves to a brief introduction to particles on the colloidal scale. The phenomenon in question is the *localized surface plasmon resonance (LSPR)*, which can be described as a collective, forced oscillation of conduction electrons in a metal particle.[100, 101] Electromagnetic waves that impinge on such a *plasmonic particle* cause a periodic displacement of the electron gas, resulting in polarization of the particle. The process of LSPR excitation is depicted in **Figure 10**.

The polarizability of the plasmonic particle depends on a wide range of parameters, such as the material, size and shape of the particle, the nature of the surrounding medium, and the wavelength of incident radiation.[100] The LSPR corresponds to the wavelength, at which the polarizability exhibits a maximum. **Figure 11** shows the influence of the particle diameter, D, and refractive index of the surrounding medium on the LSPR wavelength of AuNPs immobilized on glass substrates. The values were calculated using fit parameters of experimental data found in literature.[102] The LSPR wavelength increases with both particle size and the refractive index of the

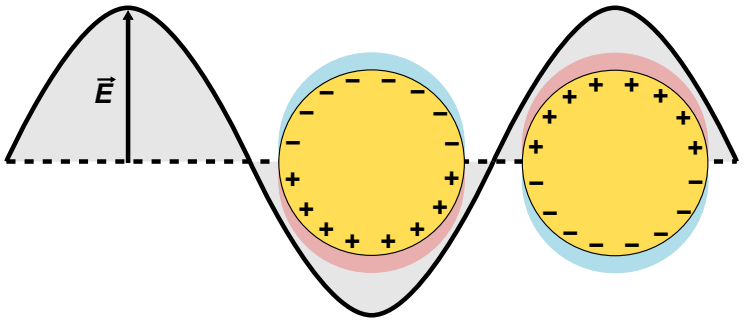

Figure 10: Schematic depiction of LSPR excitation in plasmonic nanoparticles. Light, represented here by its E-field component, irradiates a gold particle and causes an oscillating polarization of the particle, which is in phase with the electromagnetic wave. The polarization creates a strong electromagnetic near-field, indicated by the red and blue crescents.

medium. The energy stored in the oscillation can either be re-radiated or dissipated as heat, leading to scattering and absorption of the incident radiation, respectively. In contrast to most other metals, the LSPR of gold and silver nanoparticles typically occurs in the visible or near infrared range, explaining the great popularity of these materials for plasmonic particles.[99]

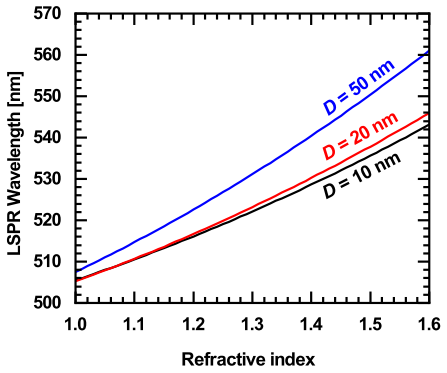

Figure 11: Calculated LSPR wavelengths of AuNPs as a function of the particle diameter and the refractive index of the surrounding medium.

2.8 RAFT polymerization

Free radical polymerization reactions are among the earliest polymerization methods used commercially and still account for a large portion of industrial polymer production.[103] The main advantages of free radical polymerization are the excellent compatibility with a wide range of vinylic monomers and relatively undemanding process conditions, allowing low production cost for these polymers.[103] However, the radical mechanism and complex kinetics result in broad molecular weight distributions, which limit the utility of free radical polymerization in some laboratory scale applications and macromolecular design in particular. Thus, efforts have been made to mimic the narrow and controlled molecular weight distributions, achievable by living anionic and cationic polymerization, with radical polymerization. This ultimately led to the development of a series of controlled radical polymerization techniques in the 1990's, including *nitroxide-mediated polymerization* (NMP), *atom-transfer radical polymerization* (ATRP), and *reversible addition-fragmentation chain transfer* (RAFT) polymerization.[104] The common working principle of all three methods is to reduce the number of active radical chain ends by a reversible deactivation of growing chains. This has two effects. Firstly, the overall rate of chain propagation is reduced compared to the rate of initiation. Secondly, the probability of chain termination is reduced, as radical-radical recombination and disproportionation become less likely. In contrast to truly living anionic and cationic polymerization techniques, termination is not completely suppressed and polymerization will eventually cease. As a result, the molecular weight distribution narrows significantly and the lower reaction rates allow for fine-tuning of the average molecular weight. Nevertheless, chain termination reactions will eventually cause the polymerization to cease, rendering these methods *controlled*, but not strictly *living* polymerizations. RAFT polymerization has seen extensive use since its first implementation in 1998.[105]. Its popularity largely originates from nature of the *chain transfer agent* (CTA) or simply *RAFT agent*, which simultaneously acts as initiator and capping agent. Thus, the chains are inserted within the structure of the CTA, which provides a convenient and versatile route towards α,ω-functionalized polymers and other complex polymer architectures. **Figure 12** shows the four prin-

cipal steps of the RAFT process. The polymerization begins with the formation of initiator radicals (Ini ·) and the addition of monomers (M) to form a first, short chain (P_n ·). Typically, but not exclusively, thermal initiators, such as AIBN, are used as radical sources. The growing chain is quickly captured by the CTA, which typically comprises a dithiocarbamate or trithiocarbonate moiety with a leaving group (R) and a moderator group (X). The former is chosen such that it can undergo homolytic cleavage of the S – R bond, whereas the latter controls the reactivity of the CTA. The radical formed by capture of the P_n · chain is mesomerically stabilized and not prone to recombination. From this point, either P_n · or R · can be released. If R · is released, it will initiate a new polymer chain (P_m ·). Finally, a steady state is achieved by reversible capture and release of polymer chains. During this equilibration stage, molecular weights of individual chains converge (i.e. n ≈ m), resulting in a narrow molecular weight distribution.

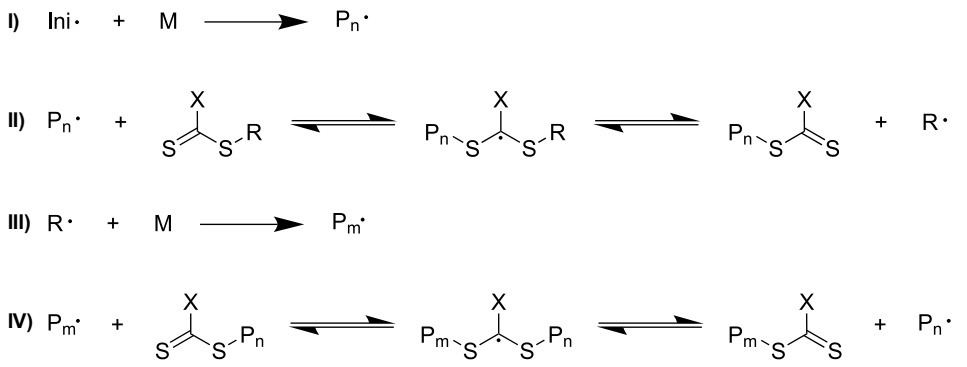

Figure 12: Fundamental steps of the RAFT process, including I) initiation, II) chain transfer, III) reinitiation, and IV) equilibration.

As mentioned previously termination occurs via recombination or disproportionation. If the concentration [CTA] of the RAFT agent is much larger than the total concentration [Ini ·] of initiator radicals generated throughout the reaction, the P_m-CTA complex on the right hand side of **Figure 12 IV** is the main product. Therefore, the monomers have effectively been inserted into the R – S bond of the original CTA. The proportion of the desired main product is determined by the livingness of the reaction, i.e. the fraction of chains that will not undergo termination. The livingness L at full

initiator conversion is shown in Equation 53, where $[\mathrm{CTA}]_0$ and $[\mathrm{Ini}]_0$ are the initial concentration of the CTA and the initiator molecules, respectively. d is a numerical parameter related to the termination mechanism, and f is the initiator efficiency, with $0 \leq f \leq 1$. Depending on the decomposition half-life of the initiator, full conversion is not achieved during the polymerization, resulting in higher livingness.[106]

$$L = \frac{[\mathrm{CTA}]_0}{[\mathrm{CTA}]_0 + d\, f\, [\mathrm{Ini}]_0} \tag{53}$$

High livingness also promotes control over the average molecular weight and allows for a narrow molecular weight distribution. Typically, $[\mathrm{CTA}]_0/[\mathrm{Ini}]_0$ ratios of 5 and larger are preferable. At low livingness, the kinetics and obtained molecular weight distribution will resemble that of a free radical polymerization.

3 Experimental section

3.1 Materials

2,2'-Azobis(2-methylpropionitrile) (AIBN, 98%, Sigma-Aldrich) was recrystallized from methanol. Styrene (99%, Acros Organics) was passed over basic alumina before use. 2-(dodecylthiocarbonothioylthio)-2-methylpropanoic acid 3-azido-1-propanol ester (CTA, 98%, Sigma-Aldrich), gold(III) chloride hydrate ($HAuCl_4$, 99.995%, Sigma-Aldrich), trisodium citrate dihydrate ($Na_3Cit \cdot 2\ H_2O$, $\geq$ 99%, Sigma-Aldrich), citric acid monohydrate ($H_3Cit \cdot H_2O$,$\geq$ 99.5%, AppliChem), EDTA tetrasodium salt dihydrate (Na_4EDTA, $\geq$ 99%, Sigma-Aldrich), sodium azide (99%, Acros Organics), tetrabutylammonium azide ($>$ 95%, TCI), hydroquinone ($\geq$ 99.5%, Carl Roth), cetyltrimethylammonium bromide (CTAB, $\geq$ 99%, AppliChem), cetyltrimethylammonium chloride (CTAC, 25 wt% in water, Sigma-Aldrich), sodium borohydride ($NaBH_4$, $\geq$ 98%, Merck), sodium bromide (NaBr, $\geq$ 99%, Fisher), ascorbic acid ($\geq$ 99%, Carl Roth), poly(N-vinylpyrrolidone) (PVP, 10 kg/mol, Sigma-Aldrich), ATTO 488-NHS (ATTO-TEC), dibenzylcyclooctyne-amine (DBCO-amine, $>$ 95%, Jena Bioscience), 3-(aminopropyl)-trimethoxysilane (APTMS, 97%, Sigma-Aldrich), and Sephadex LH-20 (GE Healthcare) were used as received. Solvents were used in analytical grade. Ultrapure water with a resistivity of 18 MΩ cm was used for syntheses and purification.

3.2 Preparative methods

3.2.1 Synthesis of spherical AuNPs

Spherical gold nanoparticles (AuNP) were prepared using an optimized protocol based on work by Schulz et al.[107] The protocol is a variation of the inverse Turkevich method, which reverses the sequence of reagent addition.[108] Synthesis usually was performed in large batches in order to compensate for the low particle concentration obtained using this protocol. For a typical batch size, 4.5 L of water were brought to boil in a 5 L Erlenmeyer flask. A solution containing 2.206 g (7.5 mmol) of $Na_3Cit \cdot 2\,H_2O$ and 0.525 g (2.5 mmol) of $H_3Cit \cdot H_2O$ in 100 mL of water as well

as 1.2 mL of an aqueous solution of Na_4EDTA (0.1 M) were added. The solution was stirred for 15 min, after which 30 mL of $HAuCl_4$ (25 mM in water) were added under vigorous stirring. The color of the solution quickly changed to a blue-ish gray, followed by a change to the typical wine red color of small AuNP in dilute dispersion within a few minutes. In order to achieve full conversion, the solution was kept boiling for 20 min and allowed to cool down to room temperature.

3.2.2 Synthesis of AuNRs

Gold nanorods (AuNRs) were prepared in a two-step method published by Vigdermann et al. with slight modifications.[40] Monocrystalline seed particles were prepared by mixing 5 mL each of aqueous solutions of CTAB (0.2 M) and $HAuCl_4$ (1 mM) at 35 °C and adding 920 µL of a freshly prepared solution of 10 mM $NaBH_4$ and 10 mM of NaOH under vigorous stirring. The color of the solution immediately changed from dark yellow to copper-brown. The solution was stirred at 35 °C for 5 min and then heated to 50 °C for 1 h in order to decompose excess $NaBH_4$. These seed particles are then used in a seed-mediated growth process. For this, 100 mL each of of aqueous solutions of CTAB (0.2 M) and $HAuCl_4$ (1 mM) were mixed at 35 °C. Then 1.4 mL of an aqueous solution of $AgNO_3$ (0.1 M) was added. After 2 min, 10 mL of an aqueous solution of hydroquinone (0.1 M) were added dropwise while gently shaking the flask, which led to a discoloration of the solution. Finally, 3.6 mL of the seed particle dispersion were added and the flaks was shaken thoroughly to disperse them. The reaction proceeded at 35 °C and without further agitation overnight, during which the color gradually changed to a dark, brown-ish red. The particles were centrifuged at 6000g rcf for 10 min, removing fast-sedimenting spherical particles. The supernatant was further purified by centrifuging twice at 4000g rcf until full sedimentation was achieved.

3.2.3 Synthesis of AuNCs

AuNCs were kindly provided by Marcel Krüsman and Philipp Hammers and were prepared by a protocol adapted from H.-L. Wu et al.[42] First, monocrystalline seeds were prepared by quickly adding 450 µL of a freshly prepared aqueous solution of

$NaBH_4$ (0.2 M) to 10 mL of a solution of 0.1 M CTAC and 0.25 mM $HAuCl_4$. The dispersion was stirred at 30 °C for 1 h. Two separate feed solutions were prepared, containing 0.1 M CTAC, 0.25 mM $HAuCl_4$, 0.02 mM NaBr, and 0.09 mM of ascorbic acid each. 25 µL of seed particle dispersion were added to 9.975 mL of the first feed solution while shaking. 313 µL of the resulting mixture were quickly added to 1.025 mL of the second feed solution. The seeded growth reaction was allowed to proceed for 30 min before quenching by centrifugation at $4700g$ rcf for 10 min.

3.2.4 Functionalization of AuNPs with PVP

In preparation for the later functionalization with polystyrene (PS) ligands, AuNPs, AuNRs, and AuNCs were coated with poly(vinylpyrrolidone) (PVP) and transferred into an organic solvent, in this case DMF. The amphiphilic nature of PVP allows the stabilization of nanoparticles in both, aqeuous and organic media, whereas the polydentate but relatively weak coordination to the gold surface render the chains easily displaceable by more strongly binding ligands. Preliminary experiments showed that the addition of 50 chains/nm^2 was sufficient to stabilize AuNPs, prepared by the inverse Turkevich method, during the entire purification and solvent exchange procedure and subsequent storage as dispersion in DMF. The method was readily adaptable to AuNRs and AuNCs. The required amount of polymer for a given particle batch was determined using Equation 54.

$$m_{\mathrm{PVP}} = 50\,\mathrm{nm}^{-2}\; A_{\mathrm{NP}}\; c_{\mathrm{NP}} V M_{\mathrm{PVP}} \tag{54}$$

Here, A_{NP} is the surface area of one particle in nm^2, c_{NP} is the molar particle concentration, V is the volume of the particle dispersion, and M_{PVP} is the molar mass of the PVP used. For spherical AuNPs, the area was calculated from the average particle radius, R.

$$A_{\mathrm{NP}} = 4\pi R^2 \tag{55}$$

If R had not been determined yet (by TEM or SAXS), a typical value of 6 nm was assumed. For AuNRs, the surface area was calculated from the average length and

width, L and D respectively. As the rods had half-spherical ends, the surface area can be approximated as show in Equation 56.

$$A_{\mathrm{NR}} = (L - D)\pi D + \pi D^2 = L\pi D \tag{56}$$

For AuNCs, the surface area was calculated from the average edge length, a. The rounded corners were ignored.

$$A_{\mathrm{NC}} = 6a^2 \tag{57}$$

Particle concentrations were calculated from UV/Vis absorption data in accordance with literature.[109, 110] First, the concentration $c_{\mathrm{Au(0)}}$ of gold atoms was determined from the absorbance spectrum applying the Lambert-Beer law. The extinction coefficient of $\epsilon = 2330$ L mol^{-1}cm^{-1} at a wavelength of 400 nm was taken from literature.[109] Then, the particle concentration can be calculated from the mass ratio between a single gold atom and a particle, as shown in Equation 58. Here, V_{NP} is the volume of one particle, M_{Au} is the molar molar mass of gold, ρ_{Au} is the density of gold, and N_{A} is Avogadro's number.

$$c_{\mathrm{NP}} = \frac{c_{\mathrm{Au(0)}} M_{\mathrm{Au}}}{V_{\mathrm{NP}} \rho_{\mathrm{Au}} N_{\mathrm{A}}} \tag{58}$$

Particle volumes were calculated in analogy to the surface areas, according to Equations 59 - 61.

$$V_{\mathrm{NP}} = \frac{4\pi}{3} R^3 \tag{59}$$

$$V_{\mathrm{NR}} = (L - D)\frac{\pi}{4} D^2 + \frac{\pi}{6} D^3 \tag{60}$$

$$V_{\mathrm{NC}} = a^3 \tag{61}$$

For the particle batch from Section 3.2.1, this yielded a required mass of 3 g of PVP ($M_{\mathrm{PVP}} = 10$ kg/mol). The polymer was dissolved in 20 mL of water and added

dropwise to the AuNP dispersion, which was then sitrred at a slow rate and at room temperature for 24 h. The volume of the dispersion was reduced to approximately 250 mL by rotary evaporation and centrifuged at 3000g rcf. The particles were redispersed in DMF and centrifugation was repeated two times, always redispersing the particles in DMF. Thus, the water was gradually replaced by DMF, achieving a residual water content below 1%. The PVP functionalized AuNPs (AuNP@PVP) were stored at 4 °C.

3.2.5 Synthesis of α,ω-functionalized PS ligands

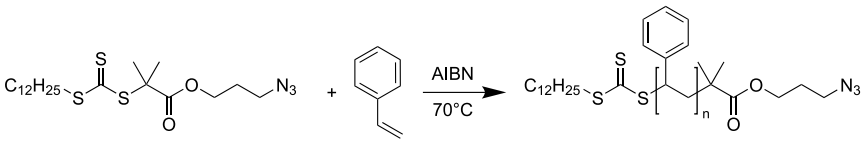

Figure 13: Reaction scheme of the RAFT polymerization of PS using an azido-terminated trithiocarbonate CTA.

The linear polystyrene ligands used for this thesis were prepared by RAFT polymerization in bulk. Due to the choice of CTA and post-modification, the chains carry a thiol group at one end and and an azide group at the other end. Whereas the thiol is the main anchor group for binding to the AuNP surface, the azide represents a versatile attachment point for further derivatization, e.g. dye labeling, by "click"-chemistry. As the azide is a small, non-ionic, and relatively inert group, it should not interfere with the overall properties of the polymers or polymer decorated nanoparticles. All synthesis followed the same general protocol, varying mainly the monomer/CTA ratio and the reaction time. First, the CTA was dispensed into a round-bottom flask. Then, AIBN was dissolved in styrene and an aliquot of this solution, containing the desired amount of AIBN, was added into the flask. Finally, styrene was added to match the monomer/CTA ratio, also incorporating the styrene added with the AIBN solution. The flask was sealed off with a rubber septum stopper and purged with argon for 20 min. The argon supply was removed and the flask was placed in a pre-heated oil bath. ^{1}H-NMR spectroscopy was used to determine the monomer conversion during

and after the RAFT polymerization and estimate the current $\overline{M}_n$ of the chains in the batch. Samples were prepared by withdrawing 50 µL from the reaction mixture and diluting them with approximately 0.45 mL of $CDCl_3$. Spectra were recorded on an Advance III (Bruker, USA) at 300 MHz operating frequency. The reaction was quenched by quickly cooling the flask in an ice bath. The polymers were purified by triple precipitation from methanol and dried in vacuo. The amounts of reagents and other reaction parameters for each batch are listed in **Table 2**. The batch name indicates the $\overline{M}_n$ of the polymer in kg/mol. Polymer characterization, including the molecular weight distributions, are discussed in Section 4.

Table 2: Overview of the reagent amounts and reaction parameters for the synthesis of PS ligands used within this thesis.

Batch	n_{CTA} [mmol]	n_{AIBN} [mmol]	$n_{Styrene}$ [mmol]	T [°C]	t_r [h]
$PS_{6.5}$	0.54	0.054	70	70	15
PS_{18}	0.22	0.044	211	70	13
PS_{21}	0.22	0.044	211	70	17
PS_{25}	0.32	0.065	103	65	93
PS_{28}	0.27	0.053	204	70	33
PS_{33}	0.22	0.044	211	70	89

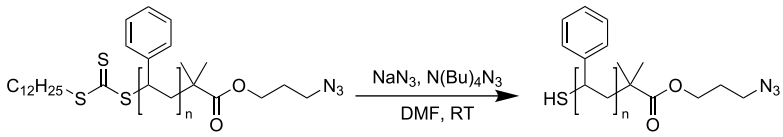

Figure 14: Reaction scheme for the cleavage of the TTC group by NaN_3 to form a thiol. Side products are not shown.

The as-prepared polymers still carry the trithiocarbonate (TTC) group form the CTA, which was cleaved in order to obtain a more reactive thiol terminus. Although the TTC also binds to gold surfaces, the C12 side chain may hinder efficient binding and increases the chain footprint on the surface.[111] A protocol published by Y. Wu et al. was used for this post-modification step.[112] This protocol uses azide ions as nucleophile to attack at the center carbon atom of the TTC group, replacing the sulfur-terminal polymer chain. The main advantage of the azide nucleophile is the

retention of the azide group at the other end of the polymer chain, which may be attacked by less specific nucleophiles, e.g. primary amines. The disadvantage is the low solubility of azide salts in organic solvents and the resulting low reaction rate. A typical TTC cleavage reaction was performed as follows. 50 µmol of polymer were dissolved in 20 mL of DMF and 60 mg (0.9 mmol) of sodium azide were added. In order to overcome the low solubility of the salt, 10 mg of tetrabutylammonium azide in 0.5 mL of DMF were added. The organic ammonium ion acts as phase transfer catalyst via the formation of a contact ion pair with the azide ion. The mixture was stirred at room temperature for 96 h. The polymers were purified by triple precipitation from methanol.

3.2.6 Fluorescent labelling of PS ligands

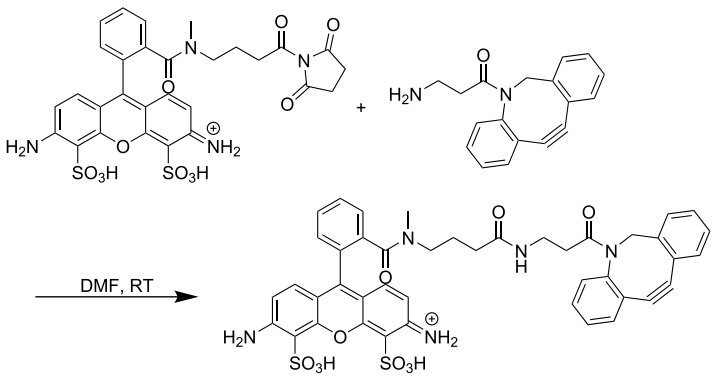

Figure 15: Reaction scheme for the functionalization of ATTO 488 with DBCO.

1 mg (1 µmol) of ATTO 488-NHS and 4 mg (15 mmol) of DBCO-amine were dissolved in 1 mL of anhydrous DMF and stirred at room temperature for 4 days. The raw product was passed over a column of Sephadex LH-20. The strongly fluorescent main fraction was passed over the column again and stored as a 0.5 mM solution in DMF. ESI-MS: m/z = 886.2 [ATTO 488-DBCO + K], 870.3 [ATTO 488-DBCO + Na], 848.1 [ATTO 488-DBCO].

1 µmol of the PS ligands were dissolved in 0.5 mL of DMF. 0.2 mL of ATTO-DBCO (0.5 mM in DMF) were added, corresponding to a maximum degree of labeling of

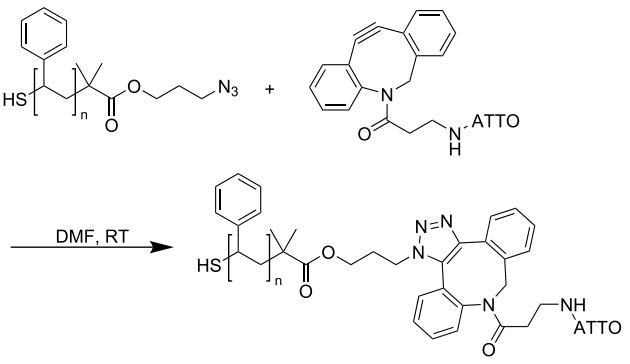

Figure 16: Reaction scheme for the coupling of ATTO 488-DBCO to PS ligands by SPAAC.

10%. The solution was stirred at room temperature for 5 days to ensure quantitative turnover. The polymer was precipitated by addition of 1 mL of methanol and centrifugation at 10000g rcf for 90 min. It was re-dissolved in DMF and precipitated again. The labeled polymers were dried in vacuo and stored as 1 mM solutions in DMF.

3.2.7 Functionalization of AuNPs with PS ligands

Polystyrene functionalized AuNPs (AuNP@PS) were prepared in a ligand exchange reaction of AuNP@PVP and α,ω-funtionalized PS ligands. This method represents a new approach for the preparation of AuNPs with hydrophobic polymer ligands in a single phase. As AuNP@PVP were stored in DMF (see Section 3.2.4), which also is a solvent for PS, the ligand exchange was conducted in this solvent. AuNP@PS were prepared in several batches over time. The standard procedure for the particle batches used in the majority of this work (apart from Section 9) was as follows. Firstly, 3.2 µmol of PS ligand (see Section 3.2.5) were dissolved in 8 mL of DMF in a glass vial. Then, 2 mL of AuNP@PVP stock dispersion (0.14 µM) were added under stirring. The resulting ratio of ligand per surface are was approximately 20 chains per nm^2. The dispersions were stirred gently for one week. Purification can be subdivided into two phases. The first phase served to remove PVP from the equilibrium and potentially increase the grafting density of PS on the particle surface. To do so, the dispersions were filled into 50 mL centrifuge tubes and 25 mL of methanol were added, causing the

AuNP@PS and free PS ligands to precipitate, whereas the PVP remains in solution. The precipitate was sedimented by centrifugation at 10000g rcf for 30 min. The supernatant was removed. The sediment was dried in air and redispersed in 10 mL of DMF. This entire process was repeated another two times. The second phase of purification was aimed to remove excess PS ligand, which was accomplished by triple centrifugation in DMF at 15000g rcf for 2 h. Finally, the AuNP@PS were redispersed in a small volume (approximately 3 mL) of DMF.

3.2.8 Amine-functionalization of glass slides and AuNP deposition

76 mm × 26 mm soda-lime glass slides were cleaned using RCA-1 solution for 30 min and dried in an oven at 60 °C.[113] For functionalization, the slides were immersed a solution of 0.5 vol% of APTMS and 0.2 vol% of glacial acetic acid in methanol and incubated at room temperature for 3 h. The slides were removed from the solution and physisorbed silane was removed by sonication in ethanol for 10 min. The slides were dried with N_2 and placed in an oven at 60 °C for 1 h to improve silane binding. The slides were sonicated twice in ethanol and once in water for 10 min each and dried at 60 °C. AuNPs were immobilized on the modified glass surface by dispensing 2 mL of a 1 nM particle dispersion on each slide and incubating at room temperature overnight. The slides were enclosed in Petri dishes to prevent excessive evaporation of liquid. The liquid was then removed with a pipette and the slides were rinsed with water and ethanol an dried with N_2. The slides were cut into smaller pieces of approximately 8 mm × 26 mm and treated with O_2 plasma (0.2 mbar, 200 W) for 5 min, using a PlasmaFlecto 10 (plasma technology GmbH, Germany). Subsequently the pieces were immersed in pH 7 phosphate buffer solution for 2 h to remove oxidation products and equilibrate surface charges and then rinsed with water and ethanol.

3.3 Methods

3.3.1 Atomic force microscopy (AFM)

AFM was used to characterize the AuNP loaded glass substrates before and after binding of PS ligands. All measurements were performed on a NanoWizard 4 (JPK Instruments, Germany), operated in intermittent contact mode (AC mode) and high-resolution force mapping mode (QI mode). OTESPA-R3 probes (f = 300 kHz, k = 26 N/m, r_{tip} = 7 nm, Bruker, USA) were used for measurements in AC mode. The typical scan size and line rate were 1 µm × 1 µm and 1 Hz, respectively. Measurements in QI mode were carried out using much softer and sharper SNL-B probes (f = 23 kHz, k = 0.12 N/m, r_{tip} = 2 nm, Bruker, USA). Tip velocity was 20 µm/s for both approach and withdrawal. The force setpoint was 1 nN and the typical scan size was 200 nm × 200 nm.

3.3.2 Measurement of ligand binding kinetics by fluorescence spectroscopy

Fluorescence based kinetics measurements were performed using a FLS 980 (Edinburgh Instruments, UK), equipped with a Xe lamp and photomultiplier tube detector in a 90° arrangement, as well as a temperature-controlled cell holder. 2.5 mL of a 10 nM solution of dye-labeled PS ligand in DMF were filled into a quartz cuvette (10 mm path length, Hellma, Germany) with a small stirring bar. The sample was placed in the cell holder, which was set to 20 °C and equilibrated for 30 min while stirring the solution. Kinetics were recorded by synchronous spectral scans with excitation wavelengths from 480 to 550 nm, an emission offset of 20 nm, and 5 nm bandwidth for both excitation and emission. Step size was 1 nm and integration time was 0.2 s. Each scan consisted of two runs which were added for a better signal-to-noise ratio. Hence, each measurement took approximately 30 s. The spectra were analyzed by a Gaussian fit with a linear background. Measurements were performed in 10 min intervals. First, a baseline of 90 min was recorded, then the AuNP loaded glass substrate was placed in the cuvette and fixed against the wall opposite the emission optics of the spectrometer.

3.3.3 UV/Vis spectroscopy

All UV/Vis spectra were recorded on a Specord S 600 (AnalytikJena, Germany) equipped with an 8-cell sample holder and Peltier elements for temperature control. The temperature was measured in a reference cell in position 8 of the holder. Measurements in water were carried out in disposable PMMA cuvettes ($d = 10$ mm), whereas measurements in non-aqueous media were carried out in quartz cuvettes ($d = 10$ mm, Hellma, Germany). For experiments involving accurate determination of peak wavelengths in different solvents, samples were equilibrated at 20°C in the holder for 10 min before the measurement. The typical sample concentration was 1 nM particle number density. Spectra were recorded for the full wavelength range from 182 to 1020 nm. A cuvette containing the same solvent as the sample was used as reference.

3.3.4 Analytical ultracentrifugation

Analytical ultracentrifugation (AUC) was used to determine the average density of AuNP@PS and from this the grafting density of chains on the particle surface. All experiments were carried out on an Optima XL-A (Beckman Coulter, USA). AuNP@PS were dispersed in DMF and the concentration was adjusted to an absorbance value of $A = 1$ at the LSPR maximum. The samples were filled into titanium centerpieces with quartz windows, which were then placed in the 8-hole rotor. The rotor chamber was evacuated and equilibrated at a temperature of 20 °C. The experiment was carried out at sedimentation velocity run at a constant speed of 5000 rpm for approximately 5 h. During the experiment, 40 radial absorbance profiles were measured per sample at 418 nm wavelength and with 20 µm radial step size. The data was analyzed using the freeware SEDFIT (v.16.36, Peter Schuck, NIST, USA) and the $c(s)$ distribution model with floating partial specific volume, $\overline{v}$. The frictional ratio was estimated as 1.2, accounting for surface roughness and hydration of the particles. Values for the viscosity and the density of DMF were taken from literature. Due to the low rotational speed and relatively small hydrostatic pressures, the solvent was assumed to be incompressible.

3.3.5 Dynamic light scattering

Angle-dependent dynamic light scattering (DLS) was employed to measure hydrodynamic radii, primarily of AuNP@PS. Measurements were carried out on a 3D LS Spectrometer (LS Instruments, Switzerland) in the 2D pseudo-cross correlated single-beam mode. A vertically polarized HeNe laser with $\lambda = 632.8$ nm was used as light source. Samples were prepared at low concentrations, typically <0.5 vol%, passed through a PTFE syringe filter (0.45 µm pore size) to remove dust and other large impurities, and filled into borosilicate cuvettes. The samples were then placed in the decalin bath of the instrument, which is used for temperature control and refractive index matching. Samples were equilibrated for a minimum of 15 min prior to measurement. Typical experiments consisted of triplicate measurements at scattering angles from 30 to 140° in 10° angle increments. Integration times were between 45 and 90 s,

depending on the concentration and scattering contrast. For depolarized measurements, the detection polarizer was turned horizontal (vh geometry). All data was analyzed using the cumulant method according to B. Frisken, including terms up to the second cumulant.[92].

3.3.6 Small angle x-ray scattering

SAXS measurements were carried out on a Xeuss 2.0 (Xenocs, France), equipped with a Cu K_α source ($\lambda = 0.154$ nm) and a Pilatus 3 300K detector (Dectris, Switzerland). Samples were prepared in 1 mm round capillaries and measured at detector distances of 1200 mm and 2500 mm with an acquisition time of 30 min per measurement. The corresponding solvents were measured as reference samples under the same conditions. Radial averaging, background subtraction and merging of the data from the two detector distances was performed with Foxtrot (v.3.4.9, Soleil/Xenocs, France). Fitting was done using SASfit (v.0.94.11, Paul Scherrer Institute, Switzerland).[114, 115]

3.3.7 Transmission electron microscopy

TEM measurements were performed on a JEM-2100Plus (JEOL, Japan) operated in bright-field mode at 80 kV acceleration voltage. Samples were prepared on carbon-coated copper grids (200 mesh, Science Services, Germany). Samples of aqueous dispersions were prepared by dispensing 7 µL of dilute dispersion onto the carbon-coated side of the grid and letting the liquid dry in air. Samples from organic dispersions were prepared by dispensing a small droplet of dispersion onto a PTFE surface and placing the grid on top of the droplet with the carbon-coated side facing down towards the liquids. The grid was removed after 60 s and dried in air. TEM images were processed and analyzed using ImageJ (v.1.50, NIH, USA).

3.3.8 Values for material properties used in this work

Refractive indices were measured using an Abbemat WR/MW (Anton Paar, Austria). Samples were equilibrated at the desired temperature until the refractive index was constant. The values relevant for this work are summarized in **Table 3**.

Table 3: Overview of refractive indices, n_D of the solvents used at $\lambda = 589.6$ nm and 20 °C and 25 °C respectively.

Solvent	$n_{D,20}$	$n_{D,25}$
MEK	1.3789	1.3764
THF	1.4073	1.4047
Dioxane	1.4223	1.4202
DMF	1.4305	1.4282
Chloroform	1.4459	1.4429
Toluene	1.4969	1.4941

Density and viscosity values for DLS and AUC were taken from literature. **Table 4** summarizes the values used in this work and indicates the source.

Table 4: Overview of densities and viscosities used in this work.

Solvent	$\rho_{D,20}$ [g/cm^3]	$\eta_{D,20}$ [mPa s]	$\rho_{D,25}$ [g/cm^3]	$\eta_{D,25}$ [mPa s]
DMF [116, 117]	0.950	0.889	0.946	0.813
Dioxane [118]			1.028	1.196

Hansen solubility parameters used in this work were taken from the *CRC Handbook of Solubility Parameters and Other Cohesion Parameters* and listed in **Table 5**.[119]

Table 5: Overview of Hansen solubility parameters, with δ_d, δ_p, and δ_h as the dispersion, polar, and hydrogen bonding components, respectively, as well as total parameters, δ_t.[119]

Substance	δ_d [MPa$^{-1/2}$]	δ_p [MPa$^{-1/2}$]	δ_h [MPa$^{-1/2}$]	δ_t [MPa$^{-1/2}$]
MEK	16.0	9.0	5.1	19.0
THF	16.8	5.7	8.0	19.4
Dioxane	19.0	1.8	7.4	20.5
DMF	17.4	13.7	11.3	24.8
Chloroform	17.8	3.1	5.7	19.0
Toluene	18.4	1.4	2.0	18.6
PS	21.3	5.8	4.3	22.5

4 Characterization of α,ω-functionalized PS ligands

4.1 RAFT polymerization and post-modification

The linear polystyrene ligands used for this thesis were prepared by RAFT polymerization. The azide group introduced by the CTA can be used for further functionalization, e.g. via Cu catalyzed azide-alkyne cycloaddition or strain promoted azide-alkyne cylcoaddition (SPAAC).[120–123] The TTC group at the other chain end can be converted into other functional groups. For this thesis, the TTC groups were hydrolyzed in order to introduce thiol group. Thiols can be used in thiol-ene "click" reactions with alkenes and Michael acceptors.[124] However, the primary use in this work was for binding of the PS chains to gold surfaces. The TTC group typically is transformed into a thiol by nucleophilic substitution using alkylamines or alcoholamines as nucleophiles.[106] As these are good nucleophiles, side reactions at other electrophilic centers are possible, in this case the primary azide and the ester linking it to the TTC. In order to retain the azide in particular, the TTC cleavage was performed using sodium azide (NaN_3) as nucleophile.[112] This salt is poorly soluble in organic solvents, such as the DMF that was used for the reaction, and tetrabutylammonium azide ($N(Bu)_4N_3$) was employed as phase transfer catalyst. The progress of the reaction is traceable by the decrease of absorbance caused by the TTC group in the UV ($\lambda_{max} \approx 315$ nm). The change is also visible as discoloration of the solution, originating from a forbidden transition and correspondingly weak absorption band between 400 and 450 nm wavelength.[125] At full conversion, the absorbance peak vanishes completely, as shown in **Figure 17**.

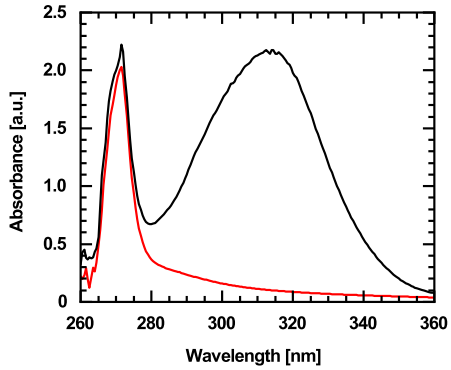

Figure 17: UV/Vis absorbance spectrum of 5 g/L solutions of PS_{33}-TTC (black) and PS_{33}-SH (red) in DMF. The strong absorbance of the TTC group vanishes due to cleavage by NaN_3. Reproduced with permission from Ref. [126]. Copyright 2021 American Chemical Society.

4.2 Molecular weight determination of RAFT polymers

During the RAFT polymerization of styrene, ^{1}H-NMR spectra were measured to monitor monomer conversion and calculate $\overline{M}_n$. The reactions were stopped once the desired molecular weight range was reached. Example spectra from an early and a late stage of the reaction, i.e. low and high conversion respectively, are shown in **Figure 18**. The relevant integration regions are indicated in blue. The region I_1 comprises peaks from two of the three vinylic protons, which only occur for the monomer. The region I_2 contains the signals from all five aromatic protons for both, the monomer and the polymer, as well as the signal from the remaining vinylic proton of the monomer. The spectrum from a late stage of the reaction in **Figure 18 b** possesses all features of the spectrum from an earlier stage. Additionally, there are broad signals corresponding to the aromatic protons of the polymer. The equally broad alkylic proton signals at low chemical shifts are not shown here. As these signals overlap with those of other reagents, notably the C12 chain of the CTA, they are not suitable for determining monomer conversion. Monomer conversion, p, is defined as shown in Equation 62, where $[M]_t$ is the monomer concentration at a point t in time and $[M]_0$ is the initial monomer concentration.

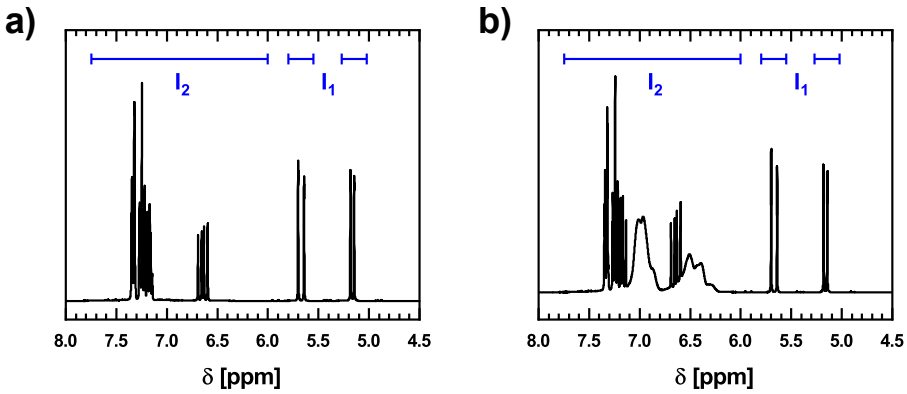

Figure 18: ^{1}H-NMR spectra from the RAFT polymerization of PS in bulk at a) an early stage of the reaction and b) at a late stage of the reaction. The integrals used for determination of conversion are shown in blue. The integrals of the two vinylic peaks between 5 and 6 ppm chemical shift were combined as I_1

$$p = \frac{[M]_0 - [M]_t}{[M]_0} = 1 - \frac{[M]_t}{[M]_0} \tag{62}$$

In our case, the exact concentrations are unknown. However, as the I_2 region contains the signals from the aromatic protons of both, monomer and the polymerized styrene unit, we can use it as a replacement for the unknown $[M]_0$. As this area also contains the signal from one of the three vinylic protons of the monomer, we have to correct I_2 as shown in Equation 63 in order to obtain the true integral for the total aromatic signals, I_a.

$$I_a = I_2 - \frac{1}{2} I_1 \tag{63}$$

With $I_a \propto [M]_0$ and $I_1 \propto [M]_t$, we can use Equation 62 to calculate the monomer conversion. In order to do so, the integrals must be normalized by the number of protons they represent, i.e. 5 for I_a and 2 for I_1, by which we obtain Equation 64.

$$p = 1 - \frac{\frac{1}{2} I_1}{\frac{1}{5} I_a} = 1 - \frac{\frac{1}{2} I_1}{\frac{1}{5}(I_2 - \frac{1}{2} I_1)} \tag{64}$$

$\overline{M}_n$ can be approximated according to Equation 65, where $n_{Styrene}$, n_{CTA}, and n_{AIBN}

are the initial molar quantities of styrene, CTA, and AIBN, respectively, M_{Styrene} is the molar mass of styrene, and M_{CTA} is the molar mass of the CTA used. d is a numerical parameter related to the termination mechanism and f is the initiator efficiency, with $0 \leq f \leq 1$.

$$\overline{M}_{\mathrm{n}} \approx \frac{n_{\mathrm{Styrene}}\, p}{n_{\mathrm{CTA}} + d\, f\, n_{\mathrm{AIBN}}} M_{\mathrm{Styrene}} + M_{\mathrm{CTA}} \tag{65}$$

NMR can only provide a rough estimate of $\overline{M}_{\mathrm{n}}$. Therefore, the molecular weight distributions were determined by size exclusion chromatography (SEC) in THF. As the system was calibrated against a series of PS standards, the molecular weights obtained by this method should be fairly accurate. The molecular weight distributions, $w(M)$, are shown in **Figure 19**.

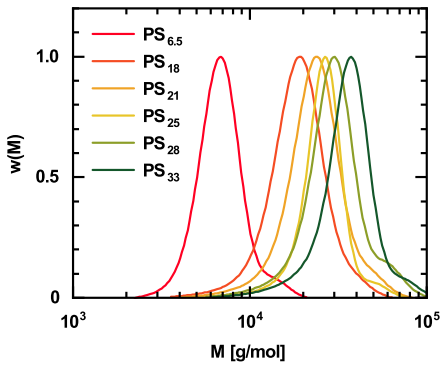

Figure 19: Molecular weight distributions measured by SEC in THF for six batches of PS prepared by RAFT polymerization. Reproduced with permission from Ref. [126]. Copyright 2021 American Chemical Society.

All distributions exhibit a single main peak and a small shoulder towards higher molecular weights. This shoulder corresponds to chain-chain termination products and therefore occurs at approximately twice the molecular weight of the main peak. **Table 6** summarizes $\overline{M}_{\mathrm{n,NMR}}$ calculated from the conversion as well as $\overline{M}_{\mathrm{n,SEC}}$ and $\overline{M}_{\mathrm{w,SEC}}$ measured by SEC. As exact values for d and f were not available, $\overline{M}_{\mathrm{n,NMR}}$ was calculated using $d\, f \approx 1$, based on data for similar conditions.[127] In some cases, the molecular weights from NMR and SEC are in good agreement, whereas they sig-

nificantly differ in others. This discrepancy originates from the complex RAFT mechanism, which hinders reliable predictions regarding the molecular weight distribution. Due to their greater accuracy, $\overline{M}_{\mathrm{n,SEC}}$ and $\overline{M}_{\mathrm{w,SEC}}$ will be used for all calculations involving molecular weights.

Table 6: Overview of the molecular weights and dispersities obtained from NMR and SEC measurements of PS ligands used within this thesis.

Batch	$\overline{M}_{\mathrm{n,NMR}}$ [g/mol]	$\overline{M}_{\mathrm{n,SEC}}$ [g/mol]	$\overline{M}_{\mathrm{w,SEC}}$ [g/mol]	$\overline{M}_{\mathrm{w}}/\overline{M}_{\mathrm{n}}$
$PS_{6.5}$	5620	6470	7130	1.10
PS_{18}	17530	17530	20190	1.15
PS_{21}	21240	21390	24880	1.16
PS_{25}	18610	24650	27200	1.10
PS_{28}	24900	27490	32200	1.17
PS_{33}	34300	33180	38110	1.15

4.3 Chain dimensions of RAFT polymers

For characterization of the polymer chain dimensions, the hydrodynamic radius, R_{h}, of the polymers was measured by DLS of dilute solutions (5 g/L). Measurements were performed in DMF and 1,4-dioxane and the correlation functions were analyzed using the cumulant method.[92] **Figure 20** shows the linear and double-logarithmic plots of R_{h} as a function of the number of monomer units, N, which was calculated from $\overline{M}_{\mathrm{n,SEC}}$. In the double-logarithmic representation, the scaling behavior should be a linear with $\ln(R_{\mathrm{h}}) = \nu \ln(N) + \gamma$, where ν is the Flory exponent and γ is the intercept. The linear fits yield Flory coefficients of $\nu_{\mathrm{DMF}} \approx 0.52$ and $\nu_{\mathrm{diox}} \approx 0.56$ for DMF and dioxane respectively. Whereas the Flory coefficient found for DMF is close to $\nu = 1/2$ observed in θ conditions, the higher value found for dioxane is closer to a good solvent ($\nu \approx 3/5$). Hence, the chains are more expanded in dioxane than in DMF. Using Equation 21, we calculate the statistical segment length, b, from ν and γ. We find that b_{DMF} is slightly larger than b_{diox}. In both cases, the chain is expanded by a factor of 3 to 4, which is in good agreement with the characteristic ratios found in literature, e.g. $C_\infty \approx 10$ and a corresponding chain expansion of $\sqrt{C_\infty} \approx 3.3$ for PS in a θ solvent.[128]

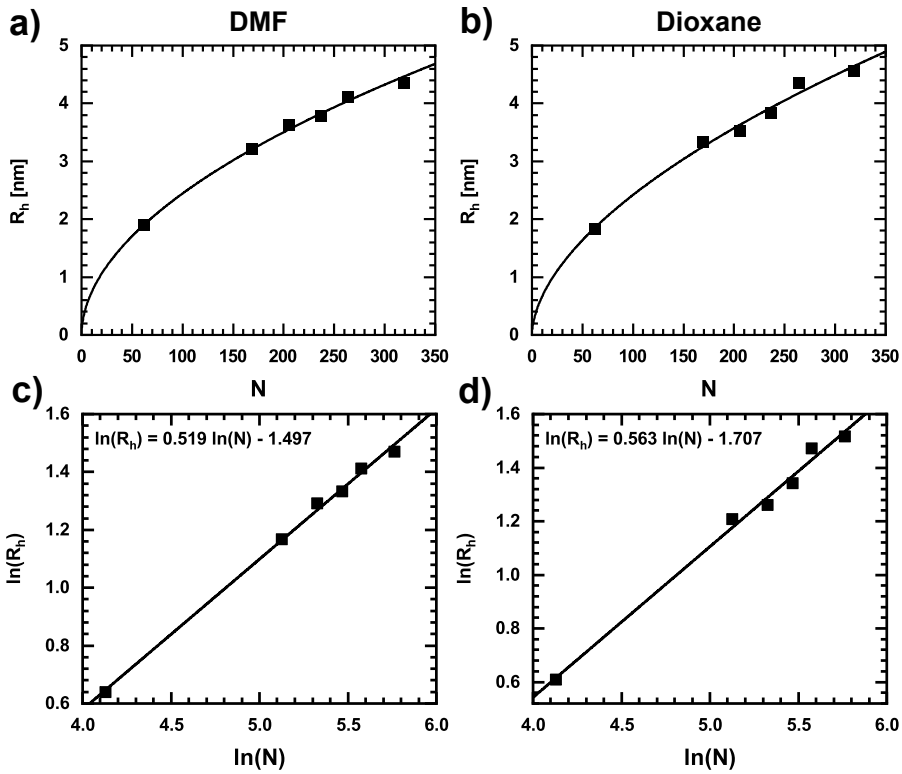

Figure 20: Plots of the hydrodynamic radius of PS ligands in relation to the number of monomer units, measured in a) DMF and b) 1,4-dioxane at 20 °C. Corresponding double-logarithmic plots for c) DMF and d) dioxane. The equations of the linear fits to the log-log plots are given. The power law curves in the lin-lin plots were generated from these fit parameters. Reproduced with permission from Ref. [126]. Copyright 2021 American Chemical Society.

$$\gamma = \ln\left[\frac{\sqrt{6\pi}}{12}(2-\nu)(1-\nu)\,b\right] \tag{66}$$

$$b_{\mathrm{DMF}} = \frac{12\exp(\gamma)}{\sqrt{6\pi}(2-\nu)(1-\nu)} = \frac{12\exp(-1.497)}{\sqrt{6\pi}(2-0.519)(1-0.519)} = 0.87\,\mathrm{nm} \tag{67}$$

$$b_{\mathrm{diox}} = \frac{12\exp(-1.707)}{\sqrt{6\pi}(2-0.563)(1-0.563)} = 0.80\,\mathrm{nm} \tag{68}$$

5 Characterization of AuNPs

For this work, small, spherical gold nanoparticles (AuNP) were prepared by the inverse citrate method, following a protocol by Schulz et al. with slight modifications.[107] In this synthesis, aurochloric acid ($HAuCl_4$) is used as metal precursor whereas a mixture of citric acid (H_3Cit) and trisodium citrate (Na_3Cit) acts as reducing agent. AuNP formation fundamentally follows a nucleation and growth mechanism. However, the details of the chemical processes and relevant parameters are complex and have been subject to debate. Turkevich, whose name is generally associated with the citrate method, first proposed a mechanism for the reduction of $HAuCl_4$ by citrate in 1951.[58] In a first step, Au(III) is reduced to Au(I), which then undergoes disproportionation into Au(0) and Au(III). Once nuclei are formed, Au(III) can be directly reduced to Au(0) in a surface reaction. Turkevich also suggested that dicarboxyacetone (DCA), a biproduct of the redox reaction, plays an important role in the nucleation step. According to his theory, DCA forms chains of bridged Au(I) complexes, increasing the local gold concentration and facilitating nucleation. Although the existence of such structures has not been confirmed,[59, 60] the importance of DCA in the nucleation step remains undisputed.[59, 108] More recent works conclude that a direct reduction of Au(III) to Au(0) takes place during nucleation, which is achieved more rapidly by DCA than by citrate itself.[60, 108, 129] Notably, DCA is not only formed by the reaction of citrate with Au(III) but also by thermal decomposition.[60, 108] In the classic Turkevich synthesis, citrate is added to a pre-heated gold precursor solution. Unless the citrate has been thoroughly pre-heated, DCA forms more gradually and its concentration remains low. In the inverse Turkevich synthesis, the citrate solution is boiled for a defined length of time before the gold precursor is added. Thus, the concentration of DCA is much higher at the beginning of the reaction, leading to very fast nucleation. At identical reactant concentrations, the inverse Turkevich method yields smaller particles with narrow size distributions and excellent reproducibility.[107, 108] Moreover, up-scaling is easily possible and does not appear to affect the outcome of the synthesis.[107] Another important aspect is that of pH control. In a typical Turkevich reaction, the pH value can change significantly during the reaction, which influences

the reactivity of the gold precursor and the reducing agent.[108, 129] The pH can be adjusted and kept relatively constant by employing a mixture of H_3Cit and Na_3Cit rather than pure citrate.[107, 129] **Figure 21** shows TEM images of AuNPs prepared by the inverse Turkevich method, recorded at 80 kV and 100,000× magnification. This specific batch of particles was used for large-scale ligand exchange experiments, discussed in subsequent chapters. However, these results are representative for the majority of particle batches used in conjunction with this work. Due to the excellent reproducibility, particle morphology, and size distributions varied little between batches.

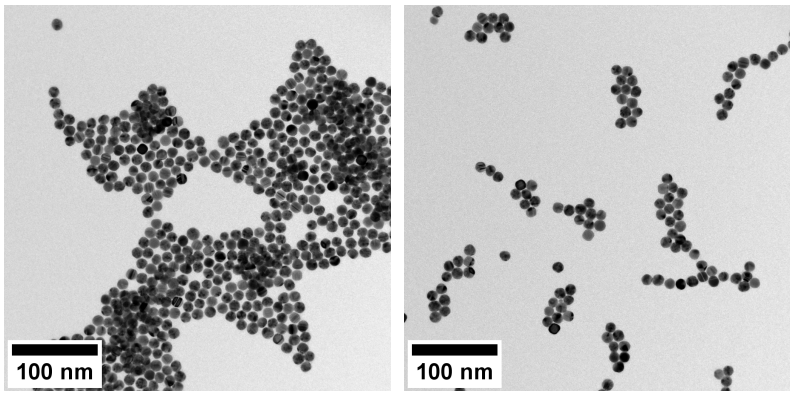

Figure 21: Representative TEM images of citrate stabilized AuNPs prepared by the inverse Turkevich method. These images were recorded at 80 kV and 100,000× magnification. The AuNPs are spherical and exhibit a narrow size distribution. The observed particle aggregation is a result of the drying process during sample preparation.

The particles exhibit a high degree of sphericity and smooth surfaces with little visible faceting. This is a result of the typical polycrystallinity of Turkevich particles and the use of EDTA, which has been found assist to in isotropic particle growth.[107] Therefore, non-spherical particle morphologies, notably triangles and bipyramids, are not observed. The size distribution is narrow and there are only very few outliers with much larger or much smaller diameters. **Figure 22 a** shows the particle size histogram from manual measurements of the diameter, d, of 194 particles. A diameter of 12.4 ± 0.6 nm was found, corresponding to a relative standard deviation of less than

5%. The narrow size distribution is also expressed by the tendency of the AuNPs to assemble in a hexagonal close packed array during sample preparation. These aggregates are not pre-existent in dispersion, which was confirmed by UV/Vis absorbance spectroscopy and small angle x-ray scattering (SAXS). **Figure 22 b** shows the UV/Vis spectrum of the AuNPs in aqueous dispersion. The LSPR peak at a wavelength of 515.5 nm is well-defined and narrow. The absence of a shoulder at longer wavelengths suggests that the particles are well-dispersed and do not form aggregates in aqueous dispersion. The increase in absorbance in the UV range can be related to inter-band transitions of metallic gold.

Figure 22 c shows the radially averaged intensity profile from a SAXS measurement of AuNPs in aqueous dispersion. The data was fitted using a polydispserse sphere model, comprising the form factor of a sphere with Gaussian size distribution and incoherent background signal. The first minimum of the undulating form factor is clearly visible. Due to the low particle concentration, subsequent minima are obscured by the noise in the high q range. From the fit, a particle diameter of 12.3 ± 0.8 nm is obtained, which is consistent with TEM data. The larger standard deviation is likely to be caused by the poor signal-to-noise ratio in the high q range. In the low q range, the intensity profiles exhibits a clear Guinier plateau. The slight increase in intensity for the first few data points can be related to inaccurate background subtraction. **Figure 22 d** shows the Guinier plot of the plateau region ($q < 0.3$ nm^{-1}). The good agreement between the data and the linear fit underlines the validity of the Guinier approximation in the low q region. More importantly, it confirms the narrow size distribution and absence of aggregates, as even a small fraction of aggregates or larger particles would cause a significant deviation from q^2 scaling in the Guinier region. The R_g of the particles can be determined from the slope of the linear fit according to equation 69.

$$\frac{d[\ln(I)]}{dq^2} = -\frac{R_\mathrm{g}^2}{3} \tag{69}$$

The found value of $R_\mathrm{g} = 5.1$ nm corresponds to a $R_\mathrm{g}/R_\mathrm{sphere}$ ratio of 0.83, which is larger than the well-known theoretical value of 0.775 for hard spheres.[130] The most likely reasons for this discrepancy are slight deviations from a perfectly spherical

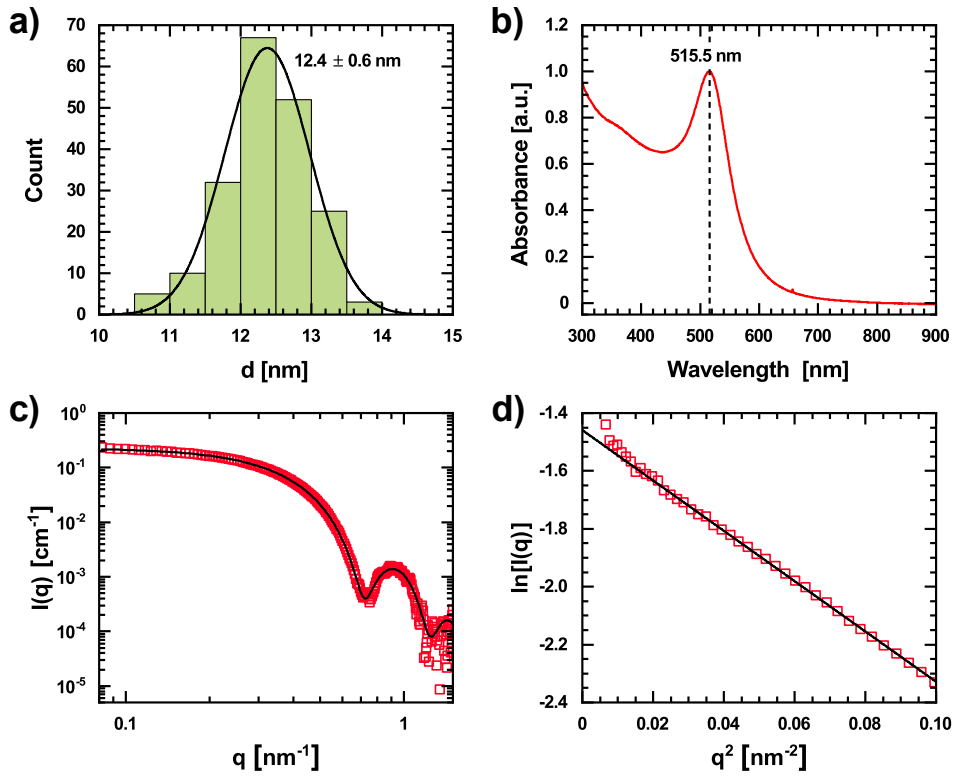

Figure 22: a) Particle size histogram of particle diameters determined from TEM images of AuNP and corresponding normal distribution. b) UV/Vis absorbance spectrum of the same batch of AuNPs measured in water at room temperature. The LSPR peak at a wavelength of 515.5 nm, as indicated by the dashed line, is well-defined and narrow. c) Radial scattering intensity profile from a SAXS measurement of the AuNPs in water. The black line corresponds to a polydisperse sphere fit to the data. The first minimum of the form factor is clearly visible. d) Guinier plot of the small q region of the radial scattering intensity and linear fit to the data. Adapted with permission from Ref. [126]. Copyright 2021 American Chemical Society.

geometry, as edges can be expected to increase R_g. For instance, a cube has $R_g = a/2$, where a is the edge length of the cube.[131] As a result, the radius of gyration of the cube is comparable to its overall dimensions, whereas the radius of gyration is always smaller than the radius of a sphere. A faceted sphere should therefore exhibit $0.775 \leq R_g/R_{\text{sphere}} \leq 1$.

6 Characterization of AuNP@PS

6.1 The two-step ligand exchange process

AuNPs were functionalized with thiol-terminated PS ligands using a two-step ligand exchange route. This approach was designed to avoid two-phase systems and provide good particle stabilization throughout the process. By performing the ligand exchange step itself in a homogeneous phase, it can continue until thermodynamic equilibrium between the old and the new ligands is achieved. In contrast to phase transfer processes, this approach is not influenced by interfacial tension, the affinity of ligands for the two phases, and particle shape or size. Moreover, kinetic aspects, e.g. the reactivity of the ligands, play only a minor role and can be compensated for by extending reaction time or increasing concentrations. Consequently, the approach used here should be robust enough to work reproducibly with a wide range of different anchoring groups, ligand materials, and molecular weight. The scheme for the ligand exchange process developed for this work is shown in **Figure 23**, using the example of Turkevich AuNPs.

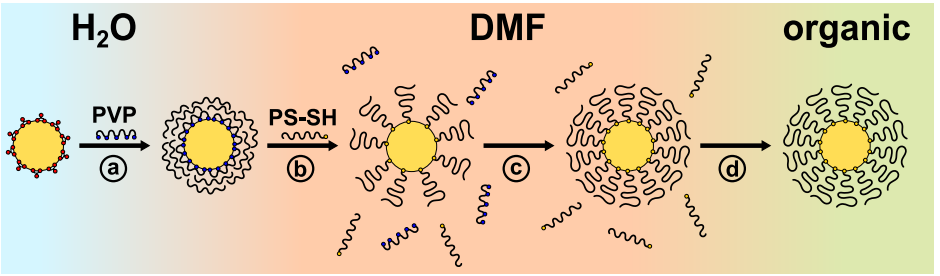

Figure 23: Scheme illustrating the ligand exchange process used in this work. a) Citrate stabilized AuNPs are functionalized with PVP, an amphiphilic, polydentate ligand, and then transferred to DMF. b) Within the DMF phase, the PVP is then displaced by thiol terminated PS ligands. In the equilibrium state, most of the PVP will be removed from the particle surface, while the solution contains PVP and excess PS ligands. c) In a first purification step, AuNP@PS and excess PS ligands are precipitated with methanol. The PVP is removed, shifting the equilibrium further towards PS functionalized particles. This may also increase the grafting density. d) In the second purification step, excess PS ligand is removed by centrifugation. AuNP@PS can be dried or stored in a suitable solvent for PS.

The first step is the functionalization of water-borne AuNPs with PVP. This polymer can wrap around particles, with each chain potentially binding in a large number of places, while providing steric stabilization. As PVP is an amphiphilic material, the formed AuNP@PVP can be transferred to an organic solvent. In this case, the water was gradually replaced with DMF by repeated centrifugation. The next step was the displacement of PVP by PS-SH ligands in an equilibrium process. There are several aspects that aid in shifting this equilibrium towards PS functionalization. Firstly, thiols and other sulfur containing functional groups tend to bind strongly to gold surfaces, whereas the amide groups of PVP are likely to bind less strongly. Secondly, an excess of PS ligand was used to avoid depletion of PS ligand in the equilibrium state. Finally, selective precipitation of AuNP@PS along with the excess PS ligands with methanol was employed. As PVP is soluble in methanol, but PS is not, the PVP is removed from the equilibrium, which can also improve grafting density and stabilization.[49] Excess PS is then removed by centrifugation of AuNP@PS. As will be demonstrated throughout the following sections, AuNP@PS with ligand molecular weights between 6.5 and 33 kg/mol were prepared. These particles are stabilized in a wide range of solvents and can even be dried completely, stored, and subsequently redispersed in a desired solvent. In general, the particles exhibit excellent long-term stability. Sedimentation only occurred over extended periods and redispersing the particles was usually possible. The properties of AuNP@PS prepared using this approach were characterized by a variety of methods, as presented in the following sections. Elemental analysis and UV/Vis spectroscopy were used to confirm the functionalization of the AuNPs with PS ligands, the stabilization, and optical properties of AuNP@PS. The dimensions and structure of the ligand shell were investigated by DLS and AUC. This will be supplemented by SAXS measurements of concentrated AuNP@PS, which provide an insight into the correlation between brush structure and particle stabilization. Finally, TEM imaging is utilized to directly visualize the ligand shell to further support findings from the other analytical methods.

6.2 Composition of the ligand shell of AuNP@PS

In order to verify the presence of PS ligands and successful displacement of auxiliary PVP ligands, vacuum-dried AuNP@PS were examined by elemental analysis. **Table 7** shows the obtained carbon, hydrogen, and nitrogen contents for AuNP@PS with four different molecular weights of PS ligand.

Table 7: Summary of obtained weight fractions of C, H, and N in dry AuNP@PS with different molecular weights of the PS ligands. The total sum of weight fractions is also given.

	PS_{18}	PS_{21}	PS_{28}	PS_{33}
C	21.7	24.8	27.9	28.1
H	2.0	2.3	2.6	2.9
N	0.5	0.5	0.4	0.4
Σ_{CHN}	24.2	27.7	31.0	31.4

The data shows that approximately 30% of the overall particle mass is comprised of organic material. Although other elements, in particular oxygen, are not measured directly, most of the residual mass can be attributed to the gold cores. Also notable is the increase of overall organic mass with increasing molecular weight of the ligand. As shown in Equation 70, this data can also be utilized for a first estimate of grafting density, σ. Here, R_{Au} is the radius of the gold cores, ρ_{Au} is the density of gold, N_A is Avogadro's number, and M_{PS} is the molecular weight of the ligand. The equation is adopted from analogous calculations of grafting densities from TGA data.[132]

$$\sigma = \frac{R_{Au}\,\rho_{Au}\,\Sigma_{CHN}\,N_A}{3\,(100-\Sigma_{CHN})\,M_{PS}} \tag{70}$$

The obtained grafting densities fall in the range of 0.3 nm^{-2} for PS_{33} to 0.5 nm^{-2} for PS_{18}, which are plausible values for long, end-on grafted polymer chains.[50, 81, 132] It should be noted that these measurements were performed on an earlier batch of AuNP@PS than all other measurements that follow hereafter and grafting densities found here are considerably lower than those that will be discussed in later sections of this thesis. In order to assess the chemical nature of the ligand shell and confirm the displacement of PVP, we will turn our attention to the relative composition of

the ligand shells. This is achieved by dividing the individual weight fractions of the elements by the total combustible weight fraction. The results of this calculation are shown in **Table 8** and are compared to the theoretical compositions of bulk PS and PVP, respectively.

Table 8: Analysis of the chemical composition of the ligand shells of AuNP@PS and comparison to the theoretical values for PS and PVP.

	PS_{18}	PS_{21}	PS_{28}	PS_{33}	PS	PVP
C/Σ_{CHN}	89.8	89.9	90.1	89.5	92.3	64.8
H/Σ_{CHN}	8.3	8.4	8.5	9.2	7.8	8.2
N/Σ_{CHN}	1.9	1.8	1.4	1.3	0	12.6

It is evident that the measured compositions of the ligand shells is in better agreement with the theoretical composition of PS than with that of PVP. Particularly, the carbon content suggests that the shell contains mainly PS. In contrast, the measured hydrogen content is even higher than theoretically predicted value for both PS and PVP, which may be an indication for impurities. The nitrogen content is non-negligible but still supports the idea that most of the PVP has been displaced. In addition, residues of DMF may have been present in the sample, which could explain the high hydrogen content and also be a source of nitrogen. Overall, the elemental analysis has shown that the ligand shell of AuNP@PS is indeed mostly comprised of PS ligands. Some residues of PVP or DMF may be present. The grafting densities estimated from this data are plausible but must be discussed in the context of other data shown in later sections.

6.3 Optical properties of AuNP@PS

This section discusses the absorbance spectra of AuNP@PS in different solvents and the influence of the refractive index of the medium and the molecular weight of the ligand on the LSPR. Furthermore, the implications for the stability of AuNP@PS in different solvents will be evaluated. **Figure 24 a** shows a photograph of AuNP@PS dispersed in the six solvents used in this section. All of these solvents are good solvents for PS and the corresponding AuNP functionalized

with this polymer should be dispersible and stable in all of them. Indeed, clear dispersions were obtained in all cases. Although the colors are similar, there are some distinguishable differences between solvents. Most notably, the particles dispersed in toluene exhibit a more blue hue than the others and some aggregation was observed.

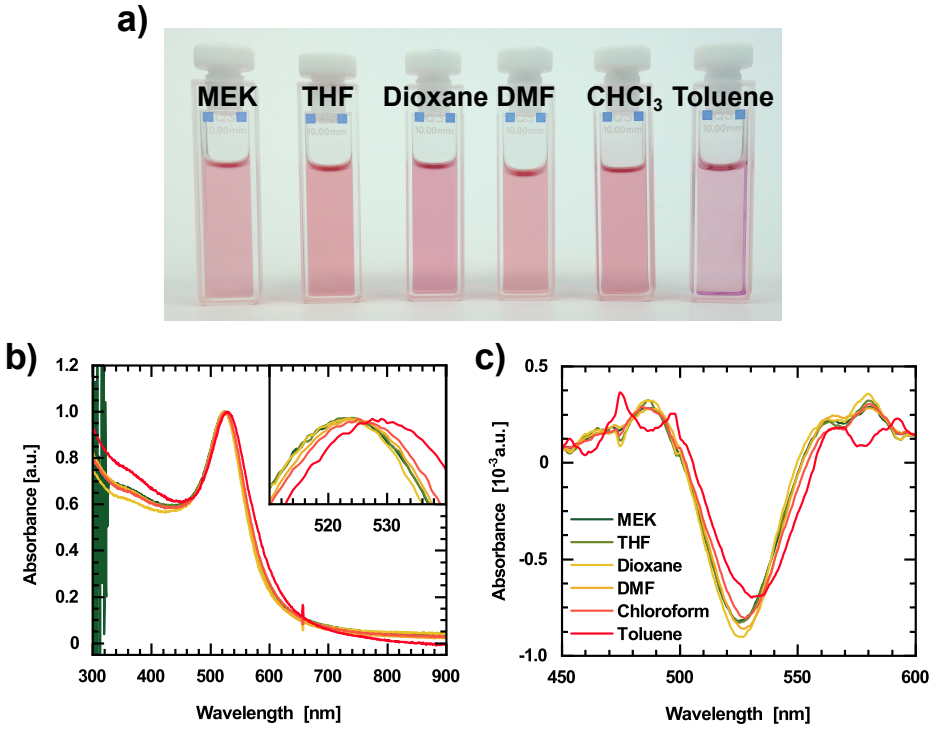

Figure 24: a) Photograph of AuNP@PS dispersed in various good solvents for PS. b) Normalized UV/Vis absorbance spectra of AuNP@PS_{18} in the same solvents. The inset shows an enlarged view of the LSPR peaks. c) Second derivatives of the UV/Vis spectra, showing the symmetric nature of the peaks in this representation, which was exploited for the accurate determination of LSPR wavelengths. Adapted with permission from Ref. [126]. Copyright 2021 American Chemical Society.

The UV-vis absorbance spectra of AuNP@PS were measured in these six solvents and for the six different molecular weights of ligand used in this thesis. The spectra for AuNP@PS_{18} are shown as an example in **Figure 24 b**. At first glance, looking at the full wavelength range, the spectra seem very similar. The differences in the short

wavelength region between 300 and 450 nm correspond to varying degrees of scattering from AuNP@PS in the solvents. Around the LSPR, differences are only visible when expanding the peak region, as shown in the inset. Notably, only the peak of AuNP@PS dispersed in toluene is significantly shifted compared to the others, which is another indication for the presence of aggregates in this solvent. Due to the small differences in LSPR wavelength between the solvents and the limited resolution of the spectrometer, the accurate determination of peak positions can be challenging. In an attempt to overcome this issue, the second derivatives of the spectra were formed, as shown in **Figure 24 c**. This method helps to isolate the LSPR peak from the underlying inter-band transitions and scattering to obtain a symmetric, Gaussian peak.[133, 134] This peak can easily be fitted to obtain the true LSPR wavelength in a very reliable fashion. Similarly to the observations made for the UV/Vis spectra, the second derivative curve for the sample dispersed in toluene differs significantly from those for the other five solvents. However, as the observable differences between LSPR wavelengths in different solvents and for the different ligand lengths are small, systematic trends are not directly apparent. In the following, the peak positions obtained from the second derivatives are analyzed in detail and compared to the behavior expected, based on theory and previous experimental evidence.

The LSPR of a small AuNP can be described by a simple dipole approximation, in which the resonance frequency or wavelength are determined by the dielectric functions of the particle and its environment.[34, 135, 136] For a simple dipole mode, resonance is achieved under the *Fröhlich condition* for $\mathrm{Re}(\epsilon) = -2\epsilon_\mathrm{m}$, where ϵ and ϵ_m are the dielectric function of the particle material and the relative permittivity of the medium respectively.[135] The relative permittivity of an ideal, i.e. non-absorbing, dielectric is related to the refractive index, n, as $n = \sqrt{\epsilon_\mathrm{m}}$.[136] In a more empiric context and over a small range of n, the change of LSPR wavelength, $\Delta\lambda$, can be related to the refractive index change Δn by a sensitivity factor, S.[136, 137]

$$\Delta\lambda = S\Delta n \tag{71}$$

Using a reference point $\lambda_0(n_0)$, Equation 71 can be rewritten as

$$\lambda = \lambda_0 + S(n - n_0) \tag{72}$$

In the case of AuNP@PS, n can be approximated as a linear combination of the refractive indices of the polymer and the solvent, n_{PS} and n_{S}, respectively. These are weighted by their corresponding volume fractions, ϕ_{PS} and ϕ_{S}, where $\phi_{\mathrm{PS}} + \phi_{\mathrm{S}} = 1$.[138]

$$n = n_{\mathrm{PS}}\phi_{\mathrm{PS}} + n_{\mathrm{S}}\phi_{\mathrm{S}} = n_{\mathrm{PS}}\phi_{\mathrm{PS}} + n_{\mathrm{S}}(1 - \phi_{\mathrm{PS}}) \tag{73}$$

Entering this expression into Equation 72, we obtain

$$\lambda = \lambda_0 + S[n_{\mathrm{PS}}\phi_{\mathrm{PS}} + n_{\mathrm{S}}(1 - \phi_{\mathrm{PS}}) - n_0] \tag{74}$$

Rearranging this expression to reflect that only n_{S} is a free variable shows that the apparent sensitivity, S', and the apparent reference wavelength, λ_0' are now functions of ϕ_{PS}, which may vary with solvent quality and molecular weight of the ligand. A complex, non-linear relationship between n_{S} and λ may therefore be observed. In addition, the sensitivity of AuNP@PS will always be smaller than the sensitivity of bare AuNPs, as $0 < \phi_{\mathrm{PS}} \leq 1$.

$$\lambda = \underbrace{\lambda_0 + S(n_{\mathrm{PS}}\phi_{\mathrm{PS}} - n_0)}_{\lambda_0'} + \underbrace{S(1 - \phi_{\mathrm{PS}})}_{\mathrm{S}'} n_{\mathrm{S}} \tag{75}$$

Figure 25 a shows the wavelengths of the LSPR absorbance maximum, λ_{LSPR}, for AuNP@PS with different ligand lengths, dispersed in six different solvents, as a function of the refractive index of the solvent. The corresponding solvents are labeled in **Figure 25 b**, which shows the average λ_{LSPR} from all $\overline{M}_{\mathrm{PS}}$.

In order of increasing n_{S} the solvents are MEK, THF, 1,4-dioxane, DMF, chloroform, and toluene. The used refractive indices at 20 °C are listed in **Table 3**. The data for AuNP@PS$_{6.5}$ is incomplete due to aggregation of these particles in MEK and toluene, which hindered accurate determination of λ_{LSPR} in these solvents. In general, the peak wavelengths for the shortest ligand are slightly longer than those of the other ligands,

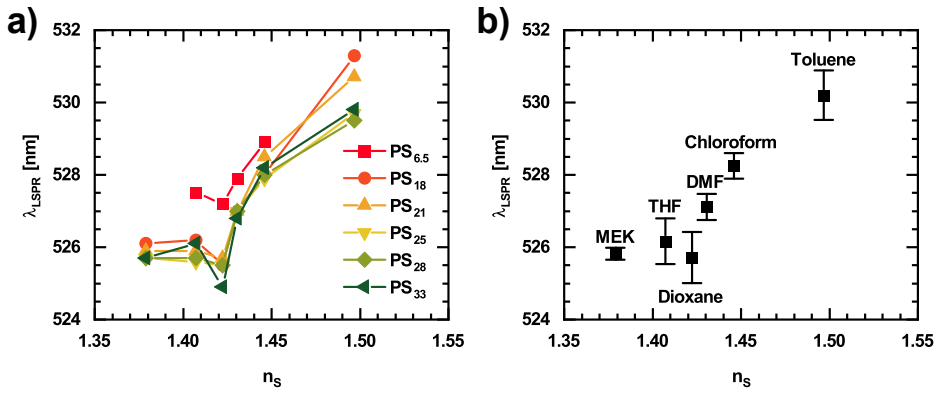

Figure 25: a) LSPR maximum wavelength of AuNP@PS with different ligand molecular weights at 20 °C in relation to the refractive index of the solvent. b) Average LSPR wavelength and standard deviation of all molecular weights.

which is another indication for aggregation, which often results in an apparent red-shift of the absorbance maximum. Comparing λ_{LSPR} in toluene, a tendency towards a red-shift with decreasing molecular weight of the ligand is also observed. In all other solvents, λ_{LSPR} is very similar, including a striking deviation from the general trend for an increase of λ_{LSPR} with increasing n_{S}.

As shown in equation 75, the apparent sensitivity, S', is strongly influenced by the volume fraction of polymer in the respective solvent. The apparent reference wavelength, λ_0', on the other hand is dominated by λ_0. Thus, linearization of the data can be attempted by plotting λ/n_{S} against $1/n_{\mathrm{S}}$, as shown in Equation 76. In this representation, λ_0' and S' will be the slope and y-intercept, respectively.

$$\frac{\lambda}{n_{\mathrm{S}}} = \left[\lambda_0 + S(n_{\mathrm{PS}}\phi_{\mathrm{PS}} - n_0)\right]\frac{1}{n_{\mathrm{S}}} + S(1-\phi_{\mathrm{PS}}) \tag{76}$$

The corresponding plots are shown in **Figure 26**. The more linear nature of this representation is obvious and has several implications. Firstly, λ_0 indeed seems to dominate the λ_0' term in Equations 75 and 76. We can therefore conclude that $\lambda_0 \gg S\Delta n$. Secondly, $S' = S(1-\phi_{\mathrm{PS}})$ has the strongest contribution to the non-linearity between λ and n_{S}. Since S can be considered a common constant for all AuNP@PS prepared from the same batch of AuNP, the deviation from linear behavior must in fact originate

from differences in effective ϕ_{PS} between solvents. The linear fit to the data in **Figure 26 b** yields a slope of $\lambda_0' = 479$ nm and an intercept of $S' = 34$ nm/RIU. As $n_0 = 0$ in this plot and with $\lambda_0' \approx \lambda_0$, the corresponding LSPR wavelength in vacuum ($n = 1$) is $\lambda_0' + S' = 513$ nm. Despite the overall good linearization in this representation, there still is a significant deviation of the data in dioxane.

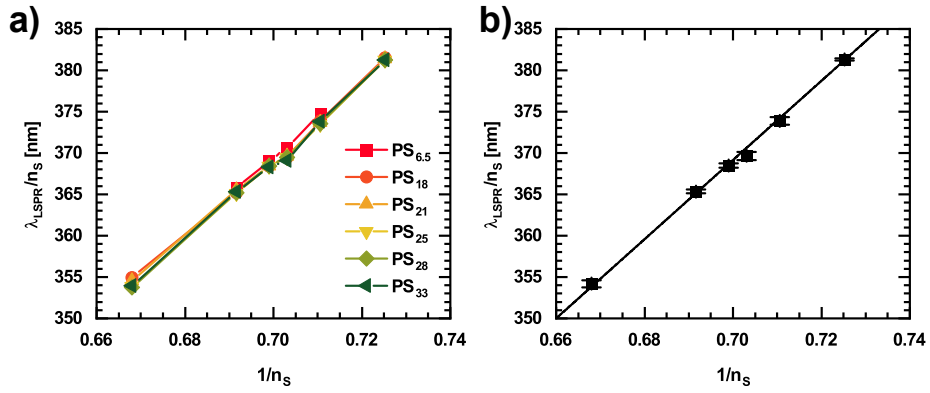

Figure 26: a) LSPR maximum wavelength of AuNP@PS with different ligand molecular weights normalized by the refractive index of the solvent in relation to the inverse refractive index of the solvent. b) Average normalized LSPR wavelength and standard deviation of all molecular weights. The solid black line is a linear fit to the data.

The found values for λ_0' and S' were used to construct the ideal linear behavior according to Equation 75. The residuals, $\lambda_{LSPR} - \lambda_{fit}$, of the average measured values and the values generated from the fit were calculated and are shown as black squares in **Figure 27 a**. The negative residuals for THF, dioxane, and DMF clearly show the deviation from the approximated linear behavior. As mentioned before, the polymer conformation and, thus, the effective volume fraction of polymer near the particle surface may differ between the solvents and be the reason for the observed deviations. Additionally, particle stability depends on solvent quality and varying degrees of aggregation of the particles may cause a more or less pronounced red-shift of the LSPR. In order to compare the observed behavior in different solvents with the solvent quality, the Flory-Huggins interaction parameters, χ, were calculated from tabulated data from Hansen solubility parameters according to Equation 2. The calculated values are shown as blue triangles in **Figure 27 a**. As discussed in section 2.1, a small value for

χ corresponds to a good solvent and vice versa. There is a striking similarity between the overall trend in $\lambda_{\mathrm{LSPR}} - \lambda_{\mathrm{fit}}$ and χ. Both plots exhibit a minimum for dioxane and a concave increase towards solvents with lower and higher refractive indices. The large theoretical solubility parameter for toluene does not match the experimentally observed good solubility of toluene. This is due to specific interactions between polymer and solvent in this particular case. Experimental values for χ of PS in toluene typically fall between 0.4 and 0.5.[119] The horizontal, dashed line in **Figure 27 a** corresponds to a wavelength difference of 0 nm as well as $\chi = 1/2$, i.e. perfect agreement with the linear fit and the interaction parameter of a θ solvent, respectively. From this, we can deduce that the linear approximation best describes the relation between λ_{LSPR} and n_{S} around the θ point. This seems logical, as the volume fraction at the θ temperature is less divergent than in a good solvent (see Equation 30). Changing the refractive index of the solvent while maintaining θ conditions should therefore lead to a relatively homogeneous change of n_{eff} throughout the polymer shell. It is reasonable to assume that better solvent quality results in a stretching of the polymer chains within the brush. Due to the limited reach of the plasmonic near-field and with $n_{\mathrm{PS}} > n_{\mathrm{S}}$ for all tested solvents, improving solvent quality should cause a decrease of n_{eff} and a blue-shift of λ.

The correlation between λ_{LSPR} and solvent quality is further demonstrated in **Figure 27 b**. Here, the deviation of the average experimental λ_{LSPR} from the linear approximation is shown in relation to $1-2\chi$, which corresponds to the dimensionless excluded volume parameter (see Equation 15). A value of $1 - 2\chi = 0$ again applies to θ conditions. The value for toluene was omitted due to the aforementioned disagreement between theoretical and experimental values for χ. Despite the large relative standard deviation of λ_{LSPR}, there is a distinctive trend for a blue-shift from the linear approximation as the excluded volume increases. This supports the hypothesis that the excluded volume effect reduced n_{eff} and therefore also λ_{LSPR}. This representation also highlights the good agreement between the linear approximation for the refractive index dependence of λ_{LSPR} with experimental values for θ solvents.

To conclude, we found that the UV/Vis absorbance spectra of AuNP@PS show a shift of the LSPR in relation to the refractive index of the solvent, which the particles

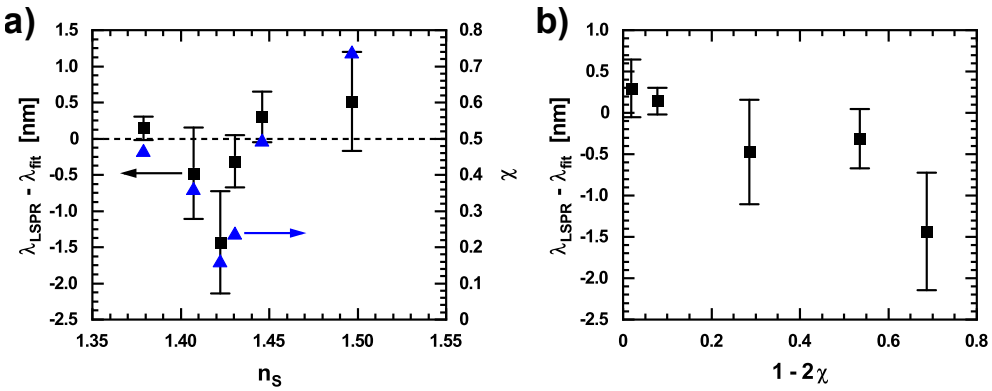

Figure 27: a) Difference between the average λ_{LSPR} and the linear approximation generated from fit parameters (black squares) and Flory solubility parameters calculated using Hansen solubility parameters (blue triangles) in relation to n_{S}. The scales of the left and right axis were scaled such that 0 nm of wavelength shift coincide with $\chi = 1/2$, as indicated by the dashed line. b) Difference between the average λ_{LSPR} and the linear approximation in relation to $1 - 2\chi$.

are dispersed in. The plasmonic shift does not exhibit the linear behavior regarding n_{S} that has been reported in literature. Nevertheless, a reciprocal plot allowed linearization and extraction of parameters for a linear approximation of the refractive index dependence of λ_{LSPR}. The deviation of the experimental values from this linear approximation appears to correlate with Flory interaction parameters of the used solvents. From this we can deduce that the excluded volume effect causes swelling of the PS ligand shell and thus a measurable decrease in n_{eff} surrounding the AuNP cores.

6.4 Thickness of the ligand shell of AuNP@PS

6.4.1 Influence of ligand molecular weight

The dimensions of AuNP@PS were investigated by dynamic light scattering (DLS). Most DLS measurements were carried out in DMF, which provided good particle stabilization and contrast. Thus, the hydrodynamic dimensions of single particles could be determined accurately. The angular dependency of decay constants, $\overline{\Gamma}$, and PDIs obtained by cumulant analysis of the measured correlation functions is shown in **Figure 28**. The q range represents angles from 30° to 140°. The $\overline{\Gamma}$ and PDI scales

are identical between samples for direct comparison.

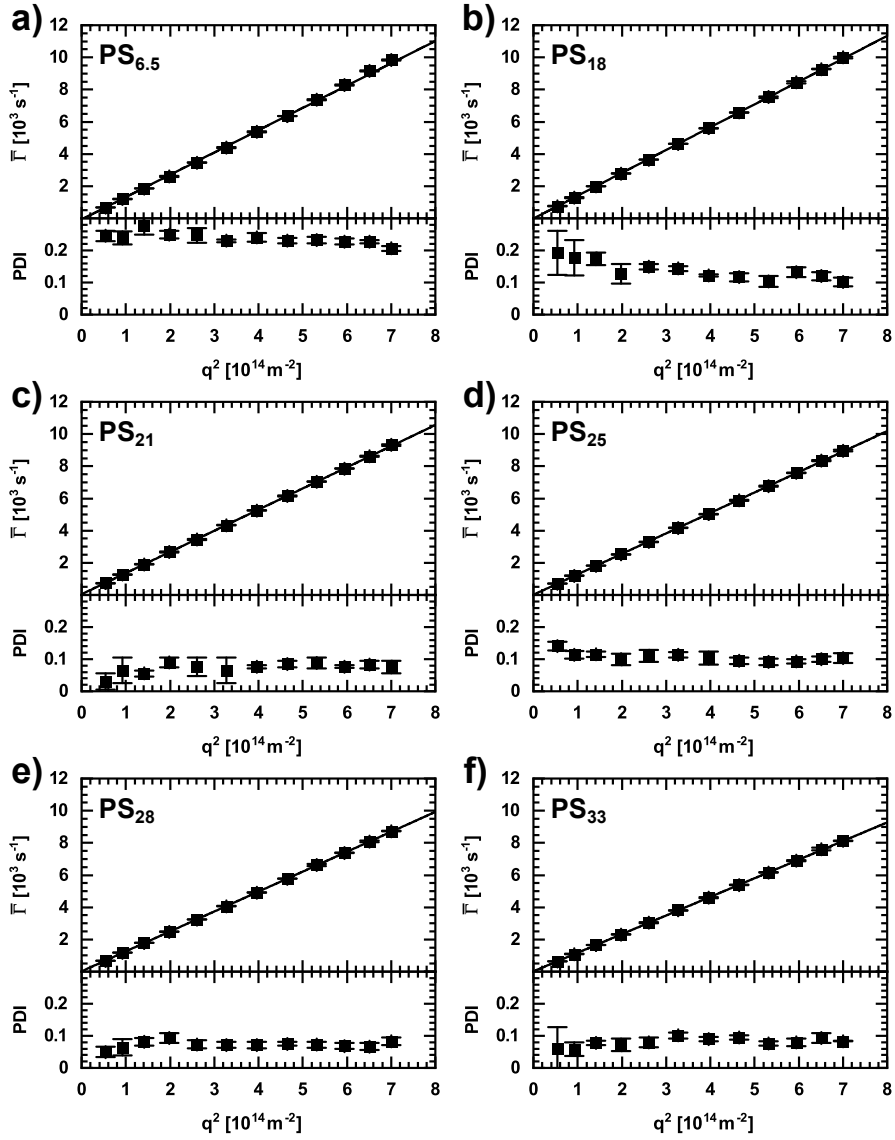

Figure 28: Angular dependency of the decay constants, $\overline{\Gamma}$, and PDIs measured for AuNP@PS in DMF at 20 °C. The linear fits to the decay constant data are used to determine the diffusion coefficient of the particles.

All six samples exhibit nearly proportional behavior of $\overline{\Gamma}$ in relation to q^2, which is indicative of purely Brownian diffusion. The intercept, $\overline{\Gamma}(0)$, is small in all cases.

The strongest deviation from ideal behavior is observed for the sample with $PS_{6.5}$ ligand, as indicated by the slight non-linearity of the data. This is an effect of a high polydispersity of up to 30%. Larger particles scatter more strongly in the low q range whereas small particles scatter almost isotropically. Therefore, the overall intensity and average $\overline{\Gamma}$ at small q over-represent large particles and aggregates and the slope is shallower. Towards large q, the small, single particles are slightly over-represented, resulting in an increase of the slope in this region of the plot. A similar observation can be made for AuNP@PS_{18}. In general, the PDI has a tendency to decrease and become less angle dependent with increasing molecular weight of the ligand. PDIs of less than 10% were found for samples with PS_{21} , PS_{28}, and PS_{33} ligand, which is remarkably low for particles of this size and given the relatively fuzzy surface presented by the polymer brush. It also confirms the reliability of the DLS data, as high PDIs reduce the accuracy and meaningfulness of $\overline{\Gamma}$.

The slopes of the linear fits to the $\overline{\Gamma}$ data represent the translational diffusion coefficients, D_t, of the particles. Using the Stokes-Einstein relation (Equation 44), R_h was calculated. **Figure 29** shows R_h and the brush height, $H = R_\mathrm{h} - R_\mathrm{c}$, where R_c is the radius of the gold core obtained from SAXS measurements. The errors of R_h obtained from the fit of D_t were implausibly small and were therefore estimated to be 5% of the corresponding value.

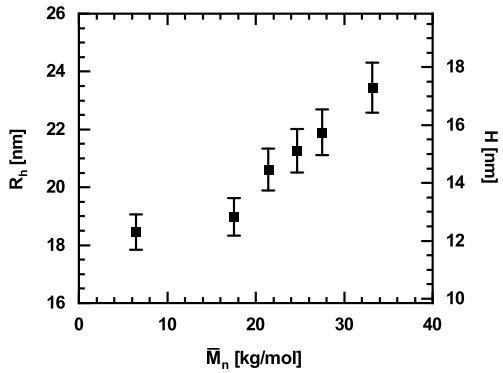

Figure 29: Hydrodynamic radii and brush heights of AuNP@PS in relation to the molecular weight of the ligand.

R_h and H increases with increasing molecular weight of the ligand. The radii determined for molecular weights ranging from 21 to 33 kg/mol appear to follow an almost linear relation. The values found for particles with $PS_{6.5}$ and PS_{18} ligands deviate above and below this apparent linear behavior, respectively. However, as the brush height also depends on the grafting density, quantitative analysis of the relationship between H and $\overline{M}_n$ is not useful at this point.

6.4.2 Influence of ligand excess

From preliminary experiments, a ligand excess of at least 20 chains per nm^2 of particle surface during the ligand exchange was deemed necessary in order to obtain stable particles for all ligand molecular weights. In this section, the influence of the ligand excess on the hydrodynamic radius of AuNP@PS is investigated in more detail. For this purpose, AuNP@PS were prepared using 10, 20, and 30 chains per nm^2 and PS_{18}, PS_{25}, and PS_{33} ligands to obtain a 3×3 parameter matrix. These particles were then examined by DLS in DMF and 1,4-dioxane. **Figure 30 a − c** shows angle dependent $\overline{\Gamma}$ and PDI plots for AuNP@PS with PS_{18}, PS_{25}, and PS_{33}, respectively. Each plot contains data for 10, 20, and 30, chains per nm^2. At first glance, there are only slight differences between measurements of AuNP@PS prepared with varying excess of the same ligand. All nine measurements exhibit a strong angle dependence of the PDI at low q^2. As discussed previously, this is an indication for larger aggregates or contaminations. However, these have only minor effect on $\overline{\Gamma}$, since linear behavior regarding q^2 is observed for all measurements. The results are summarized in **Figure 30 d**, where R_h and H are shown in relation to $\overline{M}_n$ and excess of the ligand. The data for an excess of 20 chains per nm^2 shows a similar trend regarding ligand molecular weight as shown in section 6.4.1. The exact values of R_h and H are close to those found for the main $\overline{M}_n$ dependence series in DMF. Using an excess of 10 chains per nm^2 resulted in slightly larger R_h for PS_{18} and PS_{25}, which could be a result of stronger particle aggregation due to decreased stabilization. In contrast to this, the very small R_h found for the $10 \times PS_{33}$ sample could be a direct consequence of the lower grafting density leading to less chain expansion. At the same time, the high molecular weight ligands appear to provide sufficient steric repulsion to prevent significant aggregation.

Samples with a ligand excess of 30 chains per nm^2 show a similar trend regarding $\overline{M}_n$ as samples with 20 chains per nm^2. However, a steeper increase of R_h with $\overline{M}_n$ can be observed, possibly due to even better stabilization of AuNP@PS with relatively short PS_{18} ligands.

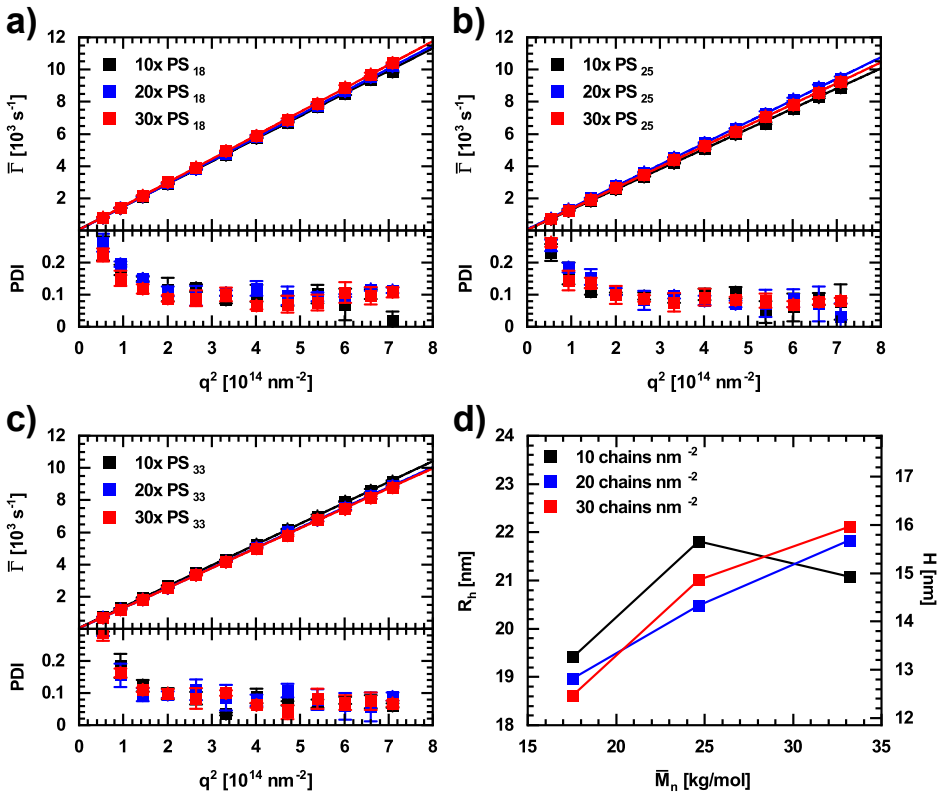

Figure 30: Angle dependent plots of $\overline{\Gamma}$ and PDI for AuNP@PS in DMF with a) PS_{18}, b) PS_{25}, and c) PS_{33} ligands, respectively. Each color corresponds to a different amount of ligand excess during ligand exchange. d) Plots of the hydrodynamic radius, R_h, and the brush height, H, in relation to molecular weight and excess of the ligand used.

The same samples were measured in dioxane. The data from cumulant analysis is shown in **Figure 31 a – c**. For samples with PS_{18} and PS_{25}, the $\overline{\Gamma}$ plots for different ligand excess again are similar. For particles with PS_{33} ligand, there is a clear difference between the slope of the plots. Moreover, the PDI for all samples in dioxane is larger than in DMF and there is a noticeable angle dependence over the entire q^2 range. In

contrast to the PDI in DMF, this variation is likely to be caused by small aggregates (i.e. dimers, trimers,...) and not by large aggregates or contaminations. **Figure 31 d** shows R_h and H from the measurement series in dioxane. Here, significant differences compared to the behavior in DMF can be observed. For an excess of 10 ligands per nm^2, there is a slightly decreasing trend for R_h and H with increasing $\overline{M}_n$. In contrast to this, R_h and H increase with $\overline{M}_n$ for an excess of 20 and 30 chains per nm^2, respectively. Consequently, there appears to be a stronger influence of ligand excess in dioxane than in DMF. This could be related to stronger swelling of the ligand shell in dioxane in combination with the aforementioned aggregation of particles.

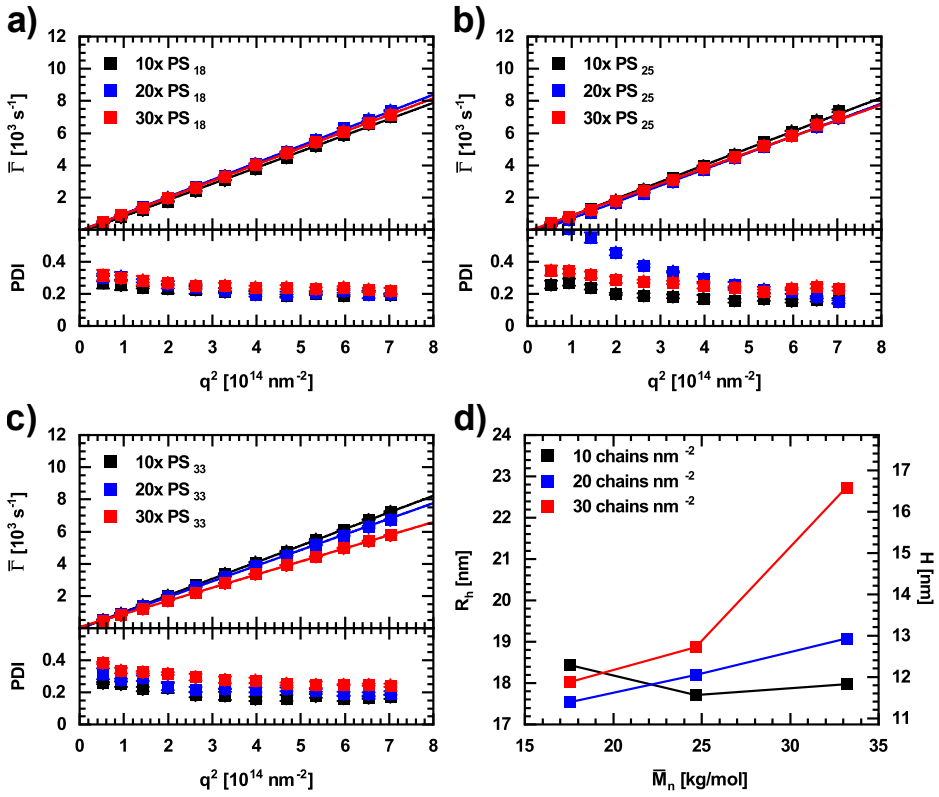

Figure 31: Angle dependent plots of $\overline{\Gamma}$ and PDI for AuNP@PS in 1,4-dioxane with a) PS_{18}, b) PS_{25}, and c) PS_{33} ligands, respectively. Each color corresponds to a different amount of ligand excess during ligand exchange. d) Plots of the hydrodynamic radius, R_h, and the brush height, H, in relation to molecular weight and excess of the ligand used.

6.4.3 Depolarized dynamic light scattering

Depolarized dynamic light scattering (DDLS) was used to gain information about the morphology of the particle clusters formed in 1,4-dioxane. If aggregation is mainly limited to (intermittent) dimer formation, as hypothesized, scattering by such anisotropic clusters should be separable by DLS measurements with crossed polarizers. In order to ensure the separability of translational and rotational diffusion, the correlation functions were plotted against $q^2\tau$, as shown in **Figure 32**.[139]

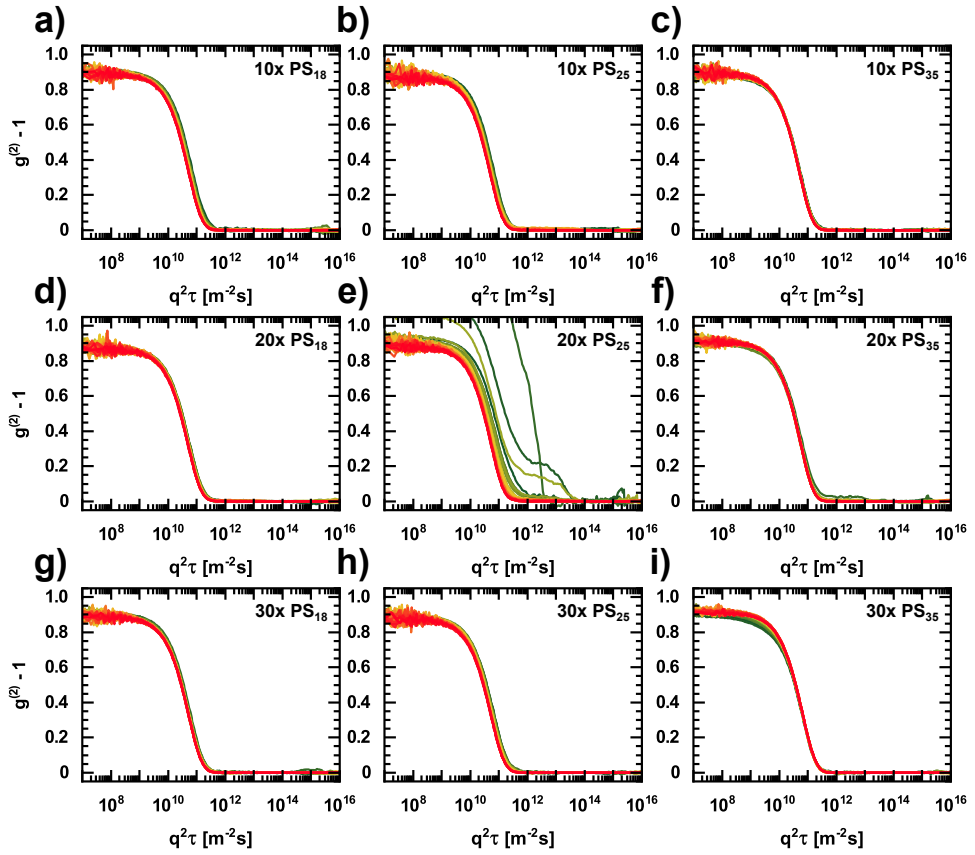

Figure 32: Autocorrelation functions of AuNP@PS measured in vv-geometry in dioxane. The curves for each sample are merged onto a master curve by re-scaling the x-axis to $q^2\tau$. q^2 increases from the dark green to the red curves.

For most samples, all autocorrelation functions fall onto a common master curve. Slight variations between autocorrelation functions are observed in particular for measurements at small scattering angles (green curves). More pronounced differences are only visible for the 20x PS_{25} sample. In all cases, these deviations can be attributed to larger contaminants in the samples. However, the plots demonstrate that D_t can be isolated from the measurements in vv-geometry, without significant contributions of rotational diffusion. This further validates the data discussed in previous section, in which the measurements in vv-geometry were discussed.

In the following, the focus will be on measurements in vh-geometry. **Figure 33 a – c** shows the average decay constants measured for AuNP@PS with varying ligand excess and ligand molecular weight. For an excess of 10 chains per nm^2 and the PS_{18} ligand no data was obtained due to low detector count rate. In general, count rates were small (<5 kHz) and acquisition times very long, e.g. 60 min per scattering angle. This also is the reason for the significant noise in the data for the PS_{25} ligand. The data for all three ligand molecular weights show a linear behavior of $\overline{\Gamma}$ regarding q^2. Overall, the values of $\overline{\Gamma}$ are approximately one order of magnitude larger than in vv-geometry. In addition, there is a significant offset at $q^2 = 0$, which relates to the rotational diffusion coefficient, D_r. Due to the poor signal quality during the measurements, the linear fits do not yield reliable values for D_t. Some of the fitted slopes are in fact negative, which is unphysical. However, since the main objective was to obtain information about the rotation and anisotropy of the clusters and the extrapolation to $q^2 = 0$ is not very sensitive towards the relatively small slopes, the fit parameters were not restricted. The values for D_r calculated from the fits are shown in **Figure 33 d**. There is an apparent trend towards smaller D_r for larger ligand excess, whereas the molecular weight does not seem to have a strong influence on rotation. As previously discussed, R_h of the particles measured in vv-geometry increased with the amount of ligand excess. The DDLS data are in good agreement with this, due to the fact that clusters of larger particles also rotate more slowly.

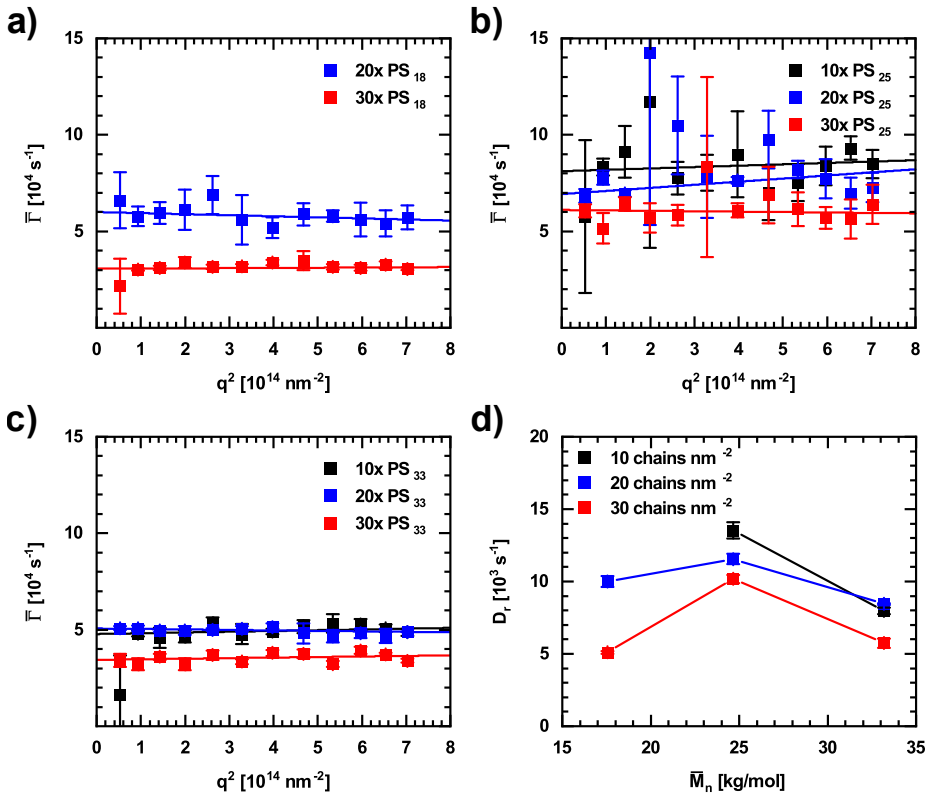

Figure 33: Angle dependent plots of $\overline{\Gamma}$ for DDLS measurements of AuNP@PS in 1,4-dioxane with a) PS_{18}, b) PS_{25}, and c) PS_{33} ligands, respectively. Each color corresponds to a different amount of ligand excess during ligand exchange. d) Plots of the rotational diffusion coefficient, D_r, in relation to molecular weight and excess of the ligand used.

The data from DLS and DDLS measurements in DMF and 1,4-dioxane are summarized as contour plots in **Figure 34**. The first two panels (**Figure 34 a – b**) show the brush height, H, calculated from R_h measured in DMF and dioxane respectively. The contour maps reveal very different behavior between the two solvents. Whereas H seems to depend on $\overline{M}_n$ for all amounts of ligand excess in DMF, H does not change over a wide parameter range in dioxane and only increases significantly for the $30\times PS_{33}$ sample. However, the range of values for H is very similar between the two. **Figure 34 c – d** show D_t and D_r from DDLS measurements in dioxane. Due to the aforementioned unphysical negative slopes of the linear fits to the angle dependent

data, only positive values of D_t are shown. Both contour maps show maxima along the 25 kg/mol axis. This could indicate that particles functionalized with this particular ligand were less stable in general and more prone to aggregation. As mentioned earlier, D_r decreases notably towards larger ligand excess.

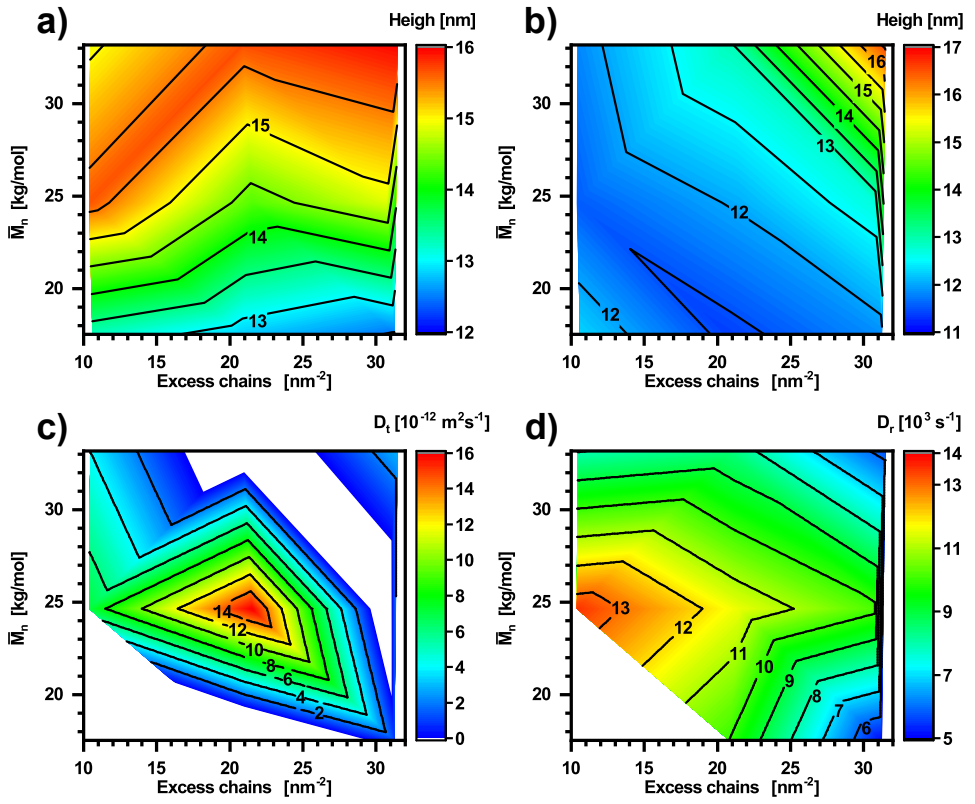

Figure 34: Brush height calculated from DLS measurements in a) DMF and b) dioxane. c) Translational diffusion coefficient, D_t, and d) rotational diffusion coefficient, D_r, from DDLS measurements in 1,4-dioxane. In all plots, the ligand excess is shown on the x-axis and the ligand molecular weight is shown on the y-axis. White areas correspond to missing or unphysical values.

6.5 Grafting density of the ligand shell of AuNP@PS

The polymer grafting density, σ, is one of the major parameters controlling the height of a polymer brush, as discussed in section 2.3. In general, the determination of grafting densities of polymer brushes at inorganic particle surfaces relies on measurements of their composition. The most used method is based on thermogravimetric analysis (TGA).[132] Assuming that only the organic polymer brush undergoes thermal decomposition during the TGA experiment, the weight fractions, w, of the polymer shell and the inorganic core are determined. From this, the number of chains per particle and, thus, the grafting density can be calculated. However, TGA is a sacrificial method that requires tens of milligrams of sample material to be thermally decomposed in order to obtain results with sufficient accuracy. Depending on the sample material, these quantities may be inaccessible. Therefore, alternative methods have been developed. One of the most promising techniques that has emerged in recent years is based on inductively coupled plasma optical emission spectroscopy (ICP-OES).[140] Good instrument calibration provided, ICP-OES can be used to very accurately measure the element composition of microgram quantities of sample material. The method used in the scope of this thesis is analytical ultracentrifugation (AUC) coupled with absorbance detection.[141] Due to their strong absorbance, AuNPs lend themselves for such AUC experiments, as long as the validity of the Lambert-Beer law can be ensured. In the case of AuNP dispersions, the absorbance in the violet and UV wavelength range, which is dominated by inter-band transitions, is proportional to the concentration $c_{\mathrm{Au^0}}$ of gold atoms. For strictly monodisperse particles, the particle concentration, c_{NP}, is proportional to $c_{\mathrm{Au^0}}$ and inversely proportional to the number of gold atoms per particle, $N_{\mathrm{Au^0}}$.

$$c_{\mathrm{NP}} = \frac{c_{\mathrm{Au^0}}}{N_{\mathrm{Au^0}}} \tag{77}$$

However, this approximation can fail for polydisperse particles during centrifugation. As demonstrated by Equations 78 – 80, the relative error of the number of gold atoms per particle, $N_{\mathrm{Au^0}}$, is three times as large as the relative error in particle radius.

$$N_{\mathrm{Au^0}} = \frac{V_{\mathrm{NP}}\,\rho_{\mathrm{Au}}\,N_{\mathrm{A}}}{M_{\mathrm{Au}}} = \frac{4\pi}{3}\,\frac{{R_{\mathrm{NP}}}^3\,\rho_{\mathrm{Au}}\,N_{\mathrm{A}}}{M_{\mathrm{Au}}} \tag{78}$$

$$\Delta N_{\mathrm{Au^0}} = 4\pi\,\frac{{R_{\mathrm{NP}}}^2\,\rho_{\mathrm{Au}}\,N_{\mathrm{A}}}{M_{\mathrm{Au}}}\Delta R_{\mathrm{NP}} = \frac{3\,N_{\mathrm{Au^0}}}{R_{\mathrm{NP}}}\,\Delta R_{\mathrm{NP}} \tag{79}$$

$$\frac{\Delta N_{\mathrm{Au^0}}}{N_{\mathrm{Au^0}}} = 3\,\frac{\Delta R_{\mathrm{NP}}}{R_{\mathrm{NP}}} \tag{80}$$

Hence, the concentration of particles that are larger than the average is overestimated and the concentration of particles that are smaller than average is underestimated. Moreover, the sedimentation coefficient, s, is proportional to the square of R_{h} (Equation 52) and larger particles sediment faster than smaller ones. Consequently, large and small particles separate and the simple relation in Equation 77 is no longer reliable, as the average $N_{\mathrm{Au^0}}$ now depends on time and position in the AUC cell. For the inverse Turkevich AuNPs used in this thesis, the particle concentration error introduced by polydispersity would be as large as 15 – 20%. However, this effect is mitigated by the polymer shell, as R_{h} and the particle density are dominated by the polymer brush. Thus, separation caused by the polydispersity of the cores is reduced and $N_{\mathrm{Au^0}}$ can again be approximated by an average value.

Figure 35 shows the radial absorbance profiles from sedimentation velocity experiments of AuNP@PS with different molecular weights of the ligand. The temporal evolution of the absorbance profile is indicated by the color coded data points. Green and red curves correspond to early and late stages of the sedimentation process, respectively. The time interval between the curves is $\Delta t \approx 8$ min. Black lines represent the solutions of the Lamm equation based on numerical c(s) distribution analysis.

During the sedimentation process, the sedimentation front, i.e. the area with the strongest radial gradient in absorbance, moves towards larger radii. Due to diffusion, the width of the sedimentation front increases over time. For large radii, the absorbance should reach a plateau value. However, the data for all measurements shows a distinct slope of the plateau region. This behavior is unusual and cannot be described by the c(s) method, as the deviation of the fits in these areas demonstrates.

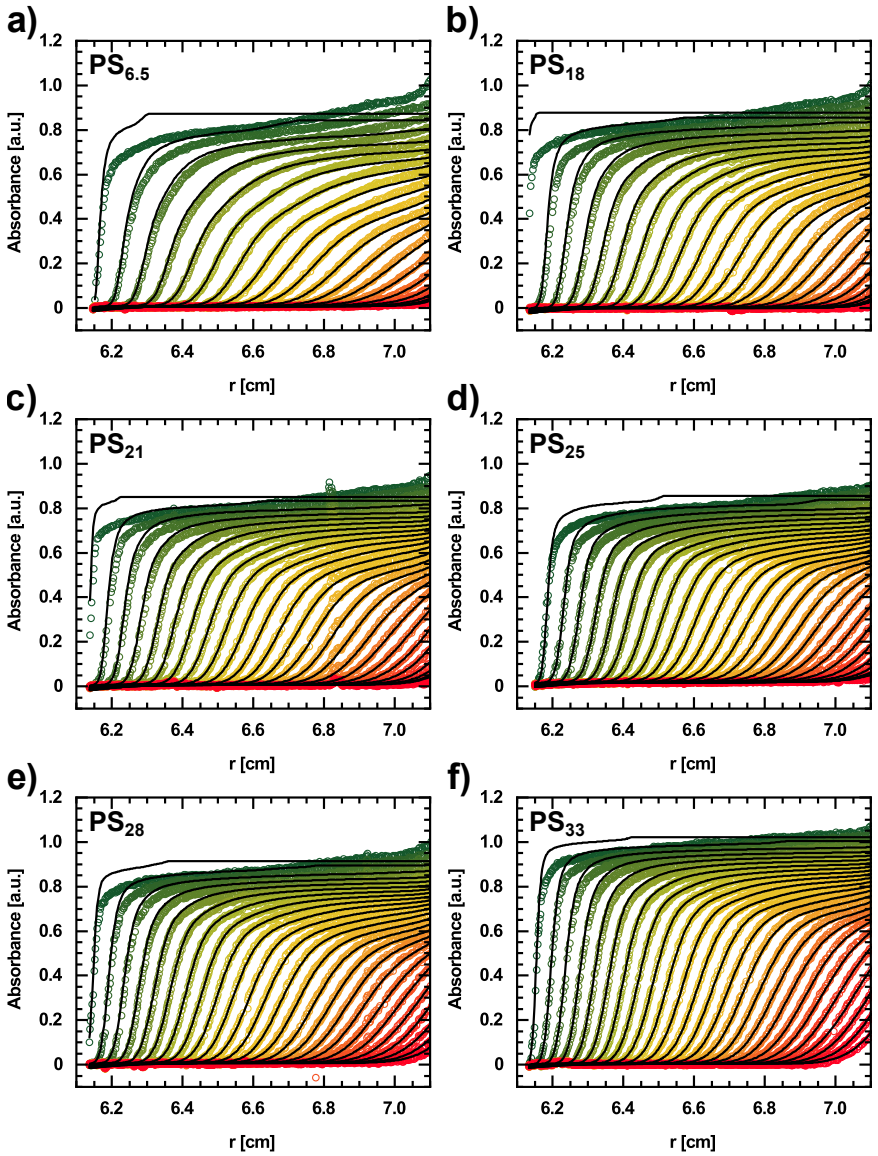

Figure 35: Radial absorbance profiles from sedimentation velocity experiments of AuNP@PS in DMF at 20 °C. The individual panels correspond to AuNP@PS with different ligand molecular weights. The color-coded data represents progression in time during the sedimentation process, with green and red data for early and late points in time respectively. The black lines correspond to the concentration profiles from the numerical solution of the Lamm equation, using the c(s) distribution method.

The origin of this slope is unclear but several explanations are possible. Firstly, the aforementioned approximation regarding the relation between absorbance and particle concentration may not hold and AuNP@PS with larger cores sediment more quickly, despite the influence of the polymer shell. Another possibility are aggregates that quickly sediment in the beginning of the process. This is supported by the observation that the fit curves deviate more at early stages of the process, whereas the absorbance profiles at later stages describe the data well. Moreover, the overall polydispersity of the AuNP@PS could broaden the sedimentation front, which should reflect in the c(s) distributions. Finally, the interparticle interactions could be the cause of the unusual behavior. Some of these interactions will be discussed in the context of small-angle x-ray scattering data in Section 6.6. Despite the poor fit of the absorbance plateau region, the c(s) distributions should be reliable, as they depend mostly on the movement of the sedimentation front. The distributions of sedimentation coefficients are shown in **Figure 36**.

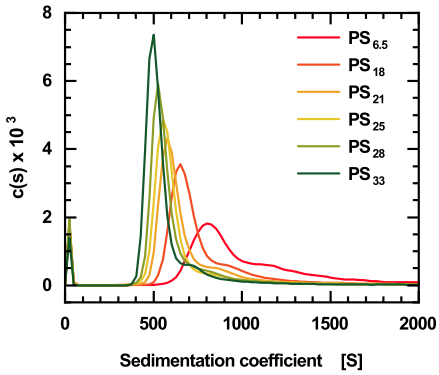

Figure 36: Distributions of sedimentation coefficients of AuNP@PS based on the c(s) distribution analysis algorithm.

All distributions show a single, Gaussian main peak and a shoulder at higher sedimentation coefficients. This shoulder can be attributed to aggregates, as they are larger than the single particles and, therefore, sediment more quickly. Whereas the shoulders are relatively well-defined for AuNP@PS with the five longest ligands, the shoulder in the c(s) distribution of AuNP@$PS_{6.5}$ is less well defined and stretches over a wider

range of sedimentation coefficients. This is in agreement with data from other methods, which indicate stronger aggregation of these particles compared to particles with longer ligands. The main peak of the distribution shifts towards smaller sedimentation coefficients with increasing molecular weight of the ligand. Consequently, the increase of hydrodynamic radius of the particles is overcompensated by the decreasing average density. This is possible due to the low density of the polymer shell, which consists of PS (1.05 g/cm^3) and DMF (0.95 g/cm^3 at 20 °C). In general, the sedimentation coefficients corresponding to the main peak range from approximately 500 to 850 S. For further calculations, the distributions were integrated over the entire range shown here in order to obtain weight average sedimentation coefficients, s_w, according to Equation 81.

$$s_\mathrm{w} = \frac{\sum c(s)\, s^2}{\sum c(s)\, s} \tag{81}$$

As demonstrated in section 2.6, the mean density of particles can be determined from sedimentation coefficients, if their hydrodynamic radius as well as the density and viscosity of the medium are known. In order to obtain the grafting density, first the density of the polymer shell, swollen with solvent, must be calculated. The mean density of the particles, ρ_part, depends on the densities of core and shell, ρ_core and ρ_shell, as well as their volume fractions, ϕ_core and ϕ_shell, as shown in Equation 82.

$$\rho_\mathrm{part} = \phi_\mathrm{core}\rho_\mathrm{core} + \phi_\mathrm{shell}\rho_\mathrm{shell} \tag{82}$$

With $\phi_\mathrm{core} = V_\mathrm{core}/V_\mathrm{part}$ and $\phi_\mathrm{shell} = V_\mathrm{shell}/V_\mathrm{part}$ this can be rewritten and solved for ρ_shell.

$$\rho_\mathrm{shell} = \frac{V_\mathrm{part}\rho_\mathrm{part} - V_\mathrm{core}\rho_\mathrm{core}}{V_\mathrm{shell}} \tag{83}$$

The volume of the gold core is $V_\mathrm{core} = 4/3\,\pi\, {R_\mathrm{core}}^3$ and the volume of the particle is the hydrodynamic volume, i.e. $V_\mathrm{part} = 4/3\,\pi\, {R_\mathrm{h}}^3$. Hence, the volume of the shell is $V_\mathrm{shell} = V_\mathrm{part} - V_\mathrm{core}$. The polymer mass per particle, m_poly, can be calculated in a similar fashion from the densities, ρ_poly and ρ_solv, and volumes, ϕ_poly and ϕ_solv of

polymer and solvent in the swollen shell.

$$\rho_{\text{shell}} = \phi_{\text{poly}}\rho_{\text{poly}} + \phi_{\text{solv}}\rho_{\text{solv}} \tag{84}$$

With $\phi_{\text{poly}} = V_{\text{poly}}/V_{\text{shell}}$, $\phi_{\text{solv}} = V_{\text{solv}}/V_{\text{shell}}$, and $V_{\text{poly}} = m_{\text{poly}}/\rho_{\text{poly}}$, Equation 84 can be solved for m_{poly}, as shown in Equation 85.

$$m_{\text{poly}} = \rho_{\text{poly}} V_{\text{shell}} \left(\frac{\rho_{\text{shell}} - \rho_{\text{solv}}}{\rho_{\text{poly}} - \rho_{\text{solv}}} \right) \tag{85}$$

Finally, σ is calculated according to Equation 86, where M_{n} is the number average molar mass of the ligand and N_{A} is Avogadro's number.

$$\sigma = \frac{m_{\text{poly}} N_{\text{A}}}{4\pi \, {R_{\text{core}}}^2 \, M_{\text{n}}} \tag{86}$$

Figure 37 a shows the calculated grafting densities in relation to the molecular weight of the ligand.

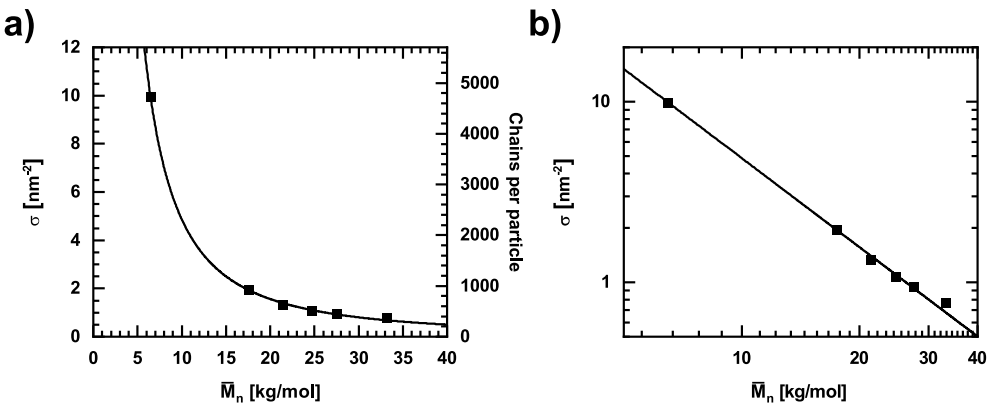

Figure 37: a) Calculated grafting densities, σ, and corresponding number of polymer chains per particle in relation to the molecular weight of the ligand. b) Double-logarithmic plot of the same data. The solid lines indicate the power law behavior.

The corresponding number of polymer chains per AuNP is also shown. σ decreases with increasing $\overline{M}_{\text{n}}$, with most values found between $\sigma = 1$ nm^{-2} and $\sigma = 2$ nm^{-2}. These values are plausible and are similar to values reported for similar systems of PS brushes on small, spherical particles.[50, 132] An exceptionally high value of almost 10

nm^{-2} was found for particles with $PS_{6.5}$ ligand. However, due to the broad distribution of s for this particle batch, the average density should be smaller than calculated. The solid line in the figure indicates the apparent power law behavior of σ regarding the molecular weight of the ligand with $\sigma \propto M^{-1.6}$. This is further demonstrated by the double-logarithmic plot in **Figure 37 b**. Apart from slight deviations at large $\overline{M}_n$, the data points seem to follow the linear relations given by the power law. The implications of this power law will be discussed in detail in the context of the overall brush scaling in section 7.

6.6 Stability and particle interactions of AuNP@PS

Small-angle X-ray scattering (SAXS) was employed in an attempt to further investigate the structure of AuNP@PS. However, the scattering length density (SLD) contrast represents a major challenge under common experimental conditions, i.e. Cu K_α radiation with $\lambda \approx 0.15$ nm. Whereas gold exhibits a very large SLD ($1.28 \cdot 10^{-2}$ nm^{-2}), the SLD of PS is much smaller ($9.59 \cdot 10^{-4}$ nm^{-2}) and comparable to that of organic solvents (e.g. $8.83 \cdot 10^{-4}$ nm^{-2} for DMF). As the scattering intensity is proportional to the squared SLD contrast (Equation 47), the contrast difference is further amplified. **Figure 38 a – b** shows the measured SAXS intensity profiles of AuNP@PS measured in DMF and dioxane. Data for all six different molecular weights of ligand from 6.5 to 33 kg/mol is shown. Due to the high SLD contrast, the intensity profiles are dominated by the polydisperse sphere form factor of the gold core, most notably distinguishable from the oscillations at $q > 0.5$ nm^{-1}. These features are identical for all samples, regardless of molecular weight of the ligand or solvent used. The average sphere radius and standard deviation of the Gaussian size distribution are 6.15 ± 0.35 nm, corresponding to the size of the gold core. The sphere form factor levels off in the Guinier plateau at small q. Whereas most of the intensity profiles measured in DMF exhibit a Guinier plateau, the radial intensity profiles measured in dioxane deviate more or less strongly from the expected behavior. An increase in intensity towards small q can be observed in most cases and even a small local maximum around $q = 0.2...0.3$ nm^{-1} is present for samples with $PS_{6.5}$ and PS_{25} ligands. These profiles could not be plausibly described by any of the available models for grafted polymer chains and the features seemed too pronounced to originate from the weak SLD contrast of the polymer. As the samples were fairly concentrated, the possibility of a structure factor contribution originating from particle-particle interactions was explored. Indeed, division of the intensity curves by the sphere form factor of the gold cores, $P(q)$, revealed periodic oscillations in the $I(q)/P(q)$ profiles, which are shown in **Figure 38 c – d**. Such features are typical for interacting particles in concentrated dispersion.

In agreement with the differences between intensity profiles measured in DMF and dioxane, the oscillations in the experimental $S(q)$ plots are more pronounced in diox-

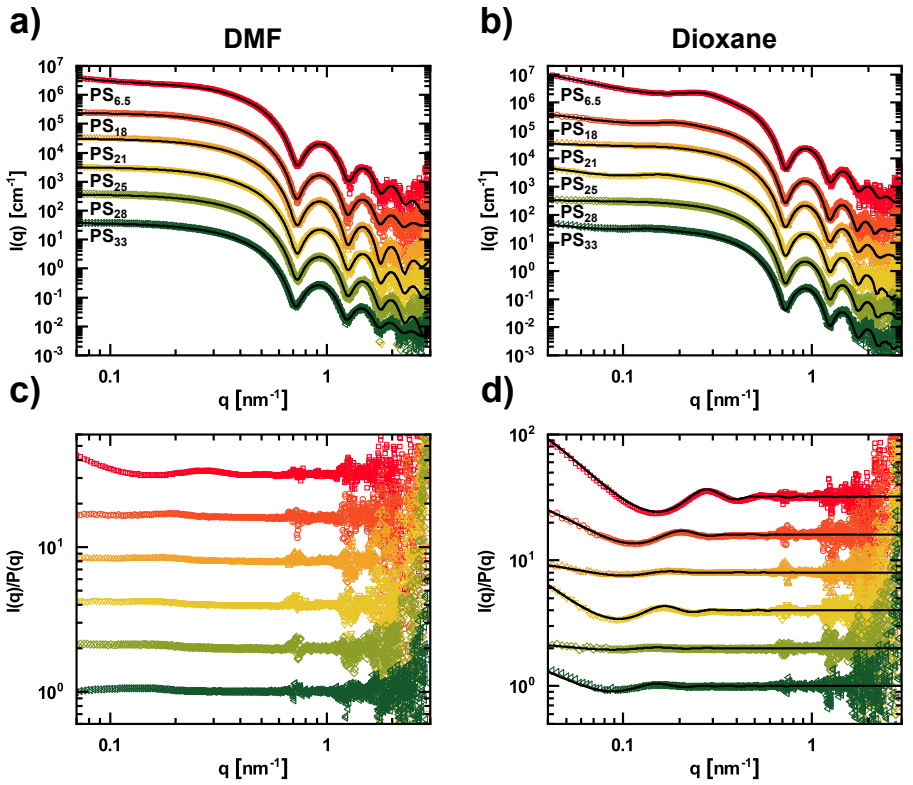

Figure 38: a – b) SAXS intensity curves of AuNP@PS with six different molecular weights of ligand measured in DMF and 1,4-dioxane. The black lines represent the corresponding fit to the data, including I_{inc}, $P(q)$, and $S(q)$. c – d) $I(q)$ divided by $P(q)$, representing the experimental structure factor. The black lines in d) correspond to the $S(q)$ profile of the SWP model calculated using the found parameters of the fit to the full intensity profile in b). Curves are offset for clarity. The measured intensities were similar for all samples and the $S(q)$ profiles all approach 0 for large q. Adapted with permission from Ref. [126]. Copyright 2021 American Chemical Society.

ane. Preliminary analysis of the first maxima of $S(q)$ for measurements in dioxane in relation to the molecular weight of the ligand suggested a systematic correlation. Hence, fitting the $I(q)$ profiles including the form factor of the cores and a structure factor was attempted. The increase in $S(q)$ towards small q is an indication for a sticky sphere interaction potential. The square well potential (SWP) was found to be able to fully describe the measured intensity profiles, as shown by the black fit lines in **Figure 38 a – b**. Using the found parameters for the SWP, the analytical approximation of

the corresponding $S(q)$ was calculated for measurements in dioxane and is shown as black lines in **Figure 38 d**. The good agreement between the measured profiles and the fit model can be seen. The main parameters obtained from the SWP model are the well depth, ϵ, the well width, Δ, and the hard sphere diameter $\sigma = 2R_{\mathrm{HS}}$. The geometrical interpretation of the SWP and a sketch of the potential model are shown in **Figure 39**.

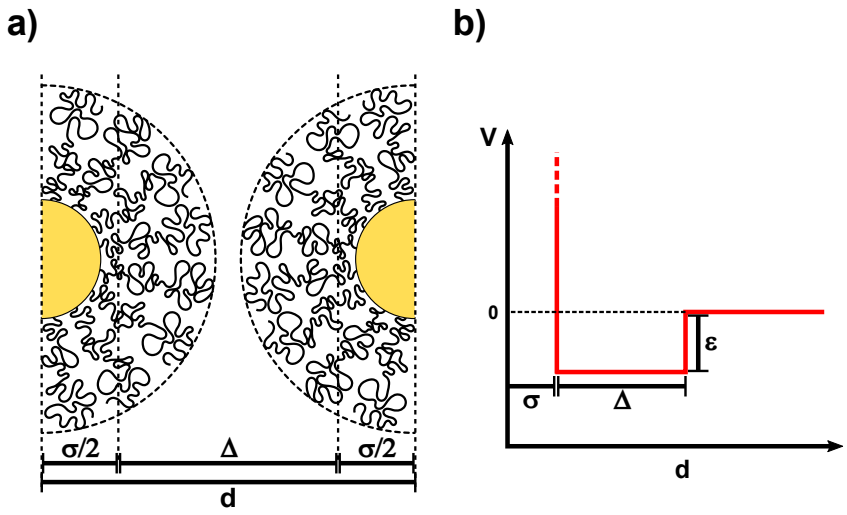

Figure 39: a) Sketch of two AuNP@PS at the onset of attractive SWP interaction at a center-to-center distance of $d = \sigma + \Delta$. b) Sketch of the potential energy profile according to the SWP model, showing all relevant parameters.

As the SWP describes pairwise interaction, the parameters can only be indirectly related to structural properties of individual AuNP@PS. It is important to note that, although AuNP@PS represent a hard core - soft shell system, σ in the SWP model does not necessarily relate to the diameter of the gold cores, D_{Au}. Equally, $\sigma + \Delta$ does not necessarily represent shell-shell contact, in particular if long-range attractive interactions, e.g. electrostatic, are present. **Figure 40** shows the SWP constructed from fit parameters found for AuNP@PS with ligand molecular weights between 6.5 and 33 kg/mol. Both the hard sphere contact, σ, and the potential onset, $\sigma + \Delta$ shift towards larger distances with increasing molecular weight. The only exception from this trend is the sample with PS_{33} ligand. Similarly, the potential well gets deeper

with increasing molecular weight of the ligand, although the depth of the well is larger than would be expected for stable particles. The well width, Δ, increases at first but decreases again for the two longest ligands.

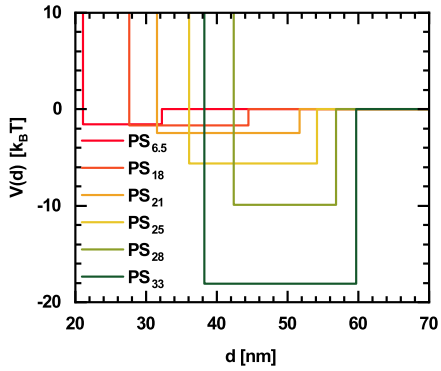

Figure 40: SWP potentials constructed from fit parameters for SAXS measurements of AuNP@PS in dioxane. A trend for larger σ and Δ with increasing molecular weight of the ligand is visible. Reproduced with permission from Ref. [126]. Copyright 2021 American Chemical Society.

In order to further interpret the SWP parameters with regard to structural properties, σ, Δ, and $\sigma + \Delta$ were normalized to the diameter D_{Au} of the gold cores and related to the molecular weight of the ligands, as shown in **Figure 41 a**. The plot allows several observations regarding the influence of the ligand length on the interaction potential. Firstly, all three parameters seem to follow a more or less linear trend, which is indicated by the straight lines. If these parameters are directly correlated with the structure and dimensions of the polymer brush, a power law could also be possible. Secondly, the hard sphere diameter, σ, reaches a value close to unity for $\overline{M}_{\mathrm{n}} \rightarrow 0$. This is plausible, since the hard sphere diameter expected in this case would be that of the gold core. However, the data also show that σ reaches much larger values for long ligand chains, thus the ligand shell contributes to hard sphere repulsion. Thirdly, the well width, Δ, remains more or less constant and in the order of D_{Au}. Hence, the reach of the attractive interaction does not depend strongly on the molecular weight of the ligand and the thickness of the ligand shell. The apparent intercept of $\Delta(0) \approx 1$ can only be explained by intrinsic interactions that do not

depend on the molecular weight of the ligands. **Figure 41 b** shows σ and $\sigma + \Delta$, normalized to the hydrodynamic diameter, D_h, of the particles.

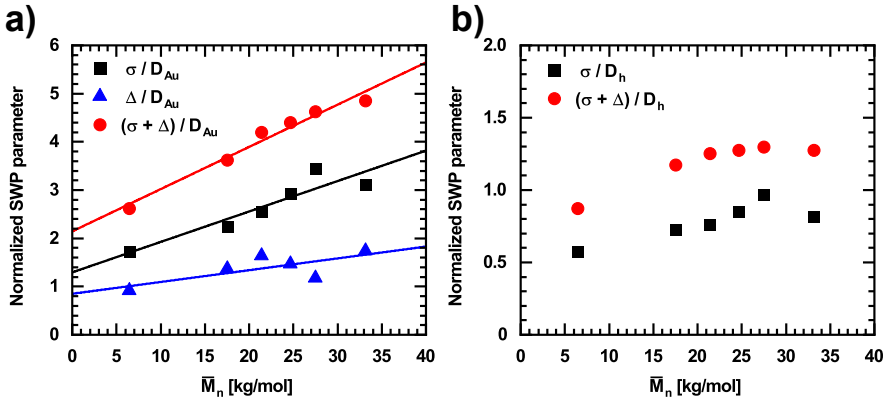

Figure 41: a) Plot of SWP parameters in relation to the molecular weight of the ligands. The parameters were normalized to the diameter, D_Au of the gold cores. The lines are a guide to the eye.. b) Plot of SWP parameters in relation to the molecular weight of the ligands. The parameters were normalized to the hydrodynamic diameter, D_h of the AuNP@PS.

Whereas the hard-sphere contact is much shorter than D_h, the overall range of the SWP exceeds D_h for all particles, except those with $PS_{6.5}$ ligands. Towards larger molecular weights, the ratio of $(\sigma+\Delta)/D_\mathrm{h}$ seems to approach a constant value between 1.2 and 1.3. This may indicate the presence of a universal size ratio, similar to the $R_\mathrm{g}/R_\mathrm{h}$ ratio in light scattering. At higher grafting densities and smaller brush heights, the AuNP@PS may approximately resemble hard spheres, with radii and interaction distances similar to R_h. With decreasing grafting density but increasing brush height, the overall volume fraction of polymer, especially in the outer regions of the brush, can be much lower. As this loose, outer brush exerts less friction, R_h will be smaller than the extend of the brush. The data shown suggests that the structure of the outer brush is similar for the longer ligands, leading to a constant ratio between the interaction range, $\sigma + \Delta$ and R_h.

In conclusion, the combined SWP onset, $\sigma + \Delta$, is defined mostly by the hard sphere radius rather than the well width. The reach of attractive interactions seems to have a large component that does not depend on $\overline{M}_\mathrm{n}$. Given the non-polar nature of dioxane,

this interaction could be promoted by the polar azide groups at the free chain ends, for instance in a mechanism similar to halogen bonding. This is further supported by the lack of a pronounced structure factor in more polar DMF. The increase in well depth with increasing chain length could be due to curvature effects, i.e. more free chain ends in direct contact for a larger radius of curvature. The overall stability of the particles is ensured by steric repulsion, which strongly depends on chain length.

6.7 Imaging of the ligand shell of AuNP@PS

So far, the structure and properties of AuNP@PS have been investigated relatively indirectly by scattering techniques and AUC. In this section, TEM microscopy is is employed to directly visualize the PS corona of AuNP@PS. The aim is to support the assumptions and conclusions made to this point, in particular regarding the influence of the molecular weight of the ligands on the structure of the polymer shell and the stabilization of AuNP@PS. **Figure 42** shows representative TEM images of AuNP@PS at 100,000× magnification.

The images show AuNPs with the same size and morphology as the as-prepared Turkevich particles (Figure 21). This is in agreement with SAXS data, which showed the retention of particle size after ligand exchange. Thus, the ligand exchange process does not affect particle morphology. In contrast to the TEM images of Turkevich particles, the AuNP@PS are well separated. The particle separation seems to increase with the molecular weight of the ligands from $PS_{6.5}$ to PS_{33}. This suggests that the height of the ligand shell and the range of interactions, as determined from DLS and SAXS measurements in dioxane, respectively, is at least partly reflected in the structures formed during TEM sample preparation. The low frequency of AuNP in close contact demonstrates the overall good stability of AuNP@PS. However, the apparent tendency of particles functionalized with $PS_{6.5}$ and PS_{18} to form larger aggregates during sample preparation complies with DLS data, which revealed the presence of aggregates for these two particle batches. Although very faint, there is a visible corona around the AuNP cores of the particles. The poor visibility of the polymer is due to the contrast mechanism in TEM, which is based on atomic number. The much higher atomic number of gold ($z = 79$) as compared to carbon ($z = 6$) results in the strong

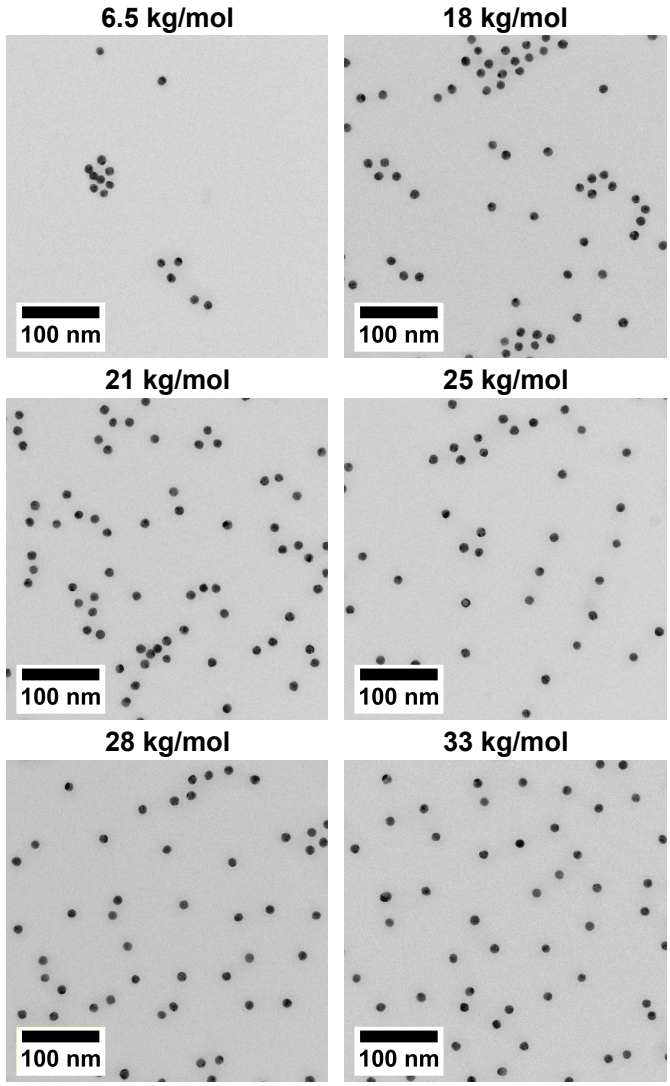

Figure 42: TEM images of AuNP@PS measured at 80 kV and 100,000× magnification. The samples were prepared from dispersion in DMF.

contrast between the cores and corona. In order to improve visibility, the contrast was digitally modified. These enhanced images are shown in **Figure 43**.

In the contrast-enhanced images, a light gray corona is now clearly visible around the AuNP cores. Additionally, the R_h of the particles is indicated as blue circles around the particle centers. The density of the corona appears the highest near the AuNP

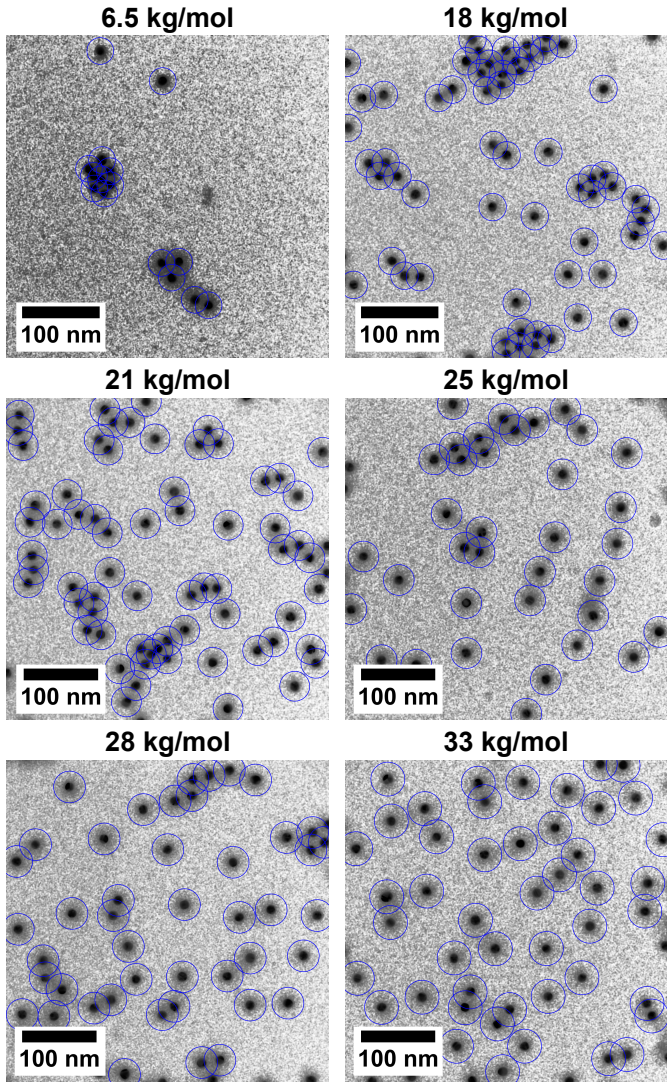

Figure 43: Digitally contrast-enhanced TEM images of AuNP@PS measured at 80 kV and 100,000× magnification. The samples were prepared from dispersion in DMF. The corresponding hydrodynamic radius of each particle batch is indicated by blue circles around the particle centers.

surface and gradually decreases outwards. The corona of particles functionalized with $PS_{6.5}$ appears to be particularly dense, which does agree with the much higher grafting densities found for this particle batch, as compared to particles functionalized with

all other ligands. A quantitative analysis of the radial profile of the corona is not feasible, as the contrast-enhancement algorithm changes pixel values non-linearly. In many cases, the corona is not radially symmetric but rather stretched to one side, which may be a result of the drying process during sample preparation. Generally, the coronas do not fill the hydrodynamic volume indicated by the blue circles. However, it should be noted that the faint corona observed in the original images seems to be larger and approximately equal to the R_h. The visibility of the corona in the original images therefore seems to originate mainly from a texture difference rather than a difference in average pixel values. From the inter-particle distances in relation to R_h, two distinct regimes of particle interaction can be defined. A majority of particle contacts exhibit a core-core distance of $d_\mathrm{cc} \approx R_\mathrm{h}$, indicating strong overlap between the polymer corona of adjacent particles. This regime of particle separation could therefore originate from polymer-polymer interactions upon drying. The second regime of interparticle-distance is found for $d_\mathrm{cc} \approx 2\ R_\mathrm{h}$, corresponding to shell-shell contact. The two distance regimes also roughly correspond to the hard-sphere contact distance, σ, and the total potential range, $(\sigma + \lambda)$, from the square-well potential model for AuNP@PS in dioxane, discussed in section 6.6.

In summary, it was possible to directly visualize the polymer corona of AuNP@PS using TEM, although digital image enhancement was required in order to improve visibility in print. A similar effect may be achievable by reactive staining of the PS corona. The images also provide further evidence of particle stabilization, as the gold cores of AuNP@PS are well separated, which was not observed for the as-prepared AuNPs. The separation distance between particles seems to loosely correlate with the hydrodynamic radius and, therefore, the chain length of the ligands.

7 Scaling of brush dimensions of AuNP@PS

This section deals with the scaling behavior of the polymer brush dimensions with regard to chain length and grafting density. For this purpose, DLS and AUC data, discussed in sections 6.4 and 6.5, will be combined to identify the scaling regime. Moreover, the mechanism of brush formation in this particular case will be elucidated. As a starting point, we will simply compare the dimensions of grafted PS chains, i.e. the brush height, to the dimensions measured in solution, discussed in Section 4.3. **Figure 44** shows the brush heights, H, calculated from DLS measurements of AuNP@PS, in relation to the chain dimensions of dissolved chains. H is given in multiples of $2R_{\mathrm{g,PS}}$ and $2R_{\mathrm{h,PS}}$, respectively. $R_{\mathrm{g,PS}}$ was calculated using Equation 20 and the experimental values for ν and b for PS in DMF.

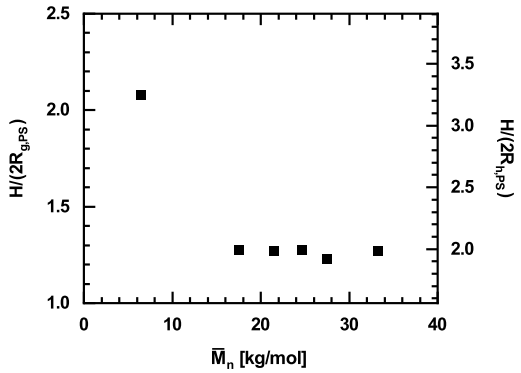

Figure 44: Ratio of brush heights relative to $2R_{\mathrm{g.PS}}$ and $2R_{\mathrm{h,PS}}$ of the free polymer chains in DMF.

For AuNP@PS with ligand molecular weights between 18 and 33 kg/mol, $H/2R_{\mathrm{g,PS}}$ falls in a narrow range of 1.2 to 1.3, corresponding to $H/2R_{\mathrm{h,PS}}$ of 1.9 to 2.1. Only particles with the $PS_{6.5}$ ligand deviate from this range, which is likely to be caused by particle aggregation, as discussed previously. Overall, it seems that the brushes are much higher than the hydrodynamic dimensions of the chains they are formed by. This points to significant chain stretching due to a high polymer volume fraction, which increases hydrodynamic drag compared to the corresponding Gaussian chains. The comparison of H with $2R_{\mathrm{g,PS}}$ is particularly interesting, as it shows that the brush

height measured by DLS is more closely related to $R_{g,PS}$ than $R_{h,PS}$. This indicates that there is a certain compactness to the ligand shell, which imposes much higher drag than a loose layer of Gaussian chains would. Qualitatively, this behavior can be compared to star polymers, for which the scaling of R_g and R_h is well-described.[77, 142, 143] Generally speaking, the R_g/R_h ratio decreases and approaches ~ 1.08, as the number f of arms of the star polymer increases.[77] This is counterbalanced by the length of the arms, with R_g/R_h approaching the value of ~ 1.5 known for Gaussian chains, as N increases.[143] Experimental results for large, multi-arm star polymers have demonstrated R_g/R_h ratios of ~ 1.3.[142] From this we can deduce that for the AuNP@PS discussed here, the overall R_h of the particles may indeed scale similar to star polymers with a large N and f. As the size of the AuNP core remains unchanged, this behavior directly reflects on scaling of the brush height.

In order to understand the structure of this polymer brush, the scaling behavior of the hydrodynamic brush height, $R_h - R_c$, in relation to N and σ will be examined in the following. As demonstrated, the brush height is likely to scale similar to a star polymer, rather than a locally flat brush. This is also supported by the small radius of the grafting surface and the high observed grafting densities. This also implies that the semi-dilute blob model, as discussed in section 2.3, may not be valid. Moreover, the dimensions of the free PS chains in DMF at room temperature were found to scale similarly to ideal chains under θ conditions. The significance of this detail becomes obvious when we remind ourselves of the absence of excluded volume effects under theta conditions. Excluded volume plays a major role in the degree of chain stretching in polymer brushes in good solvents. Ideal chains on the other hand can theoretically interpenetrate without penalty to the free energy of the chains. This is somewhat complicated by the notion that a clear definition of the θ state of star polymers is difficult. Daoud and Cotton have pointed out that despite scaling with $N^{1/2}$ locally, arms of star polymers in θ solvents can be compressed or stretched beyond their ideal conformation.[84] In other words, even ideal chains experience long-range interactions when confined in a brush.

First, we want to test whether the observed brush height scales in the SDPB regime. According to Wijmans and Zhulina, the brush height of a semi-dilute, spherical

polymer brush in good solvents and in θ solvents should scale with $N^{3/5}\sigma^{1/5}$ and $N^{1/2}\sigma^{1/4}$, respectively.[85] **Figure 45** shows the double-logarithmic plots of the experimental brush height compared to these two scaling laws. The slope of the scaling relation is approximated by a linear fit. Since the first two data points ($PS_{6.5}$ and PS_{18}) strongly deviate from the behavior of the remaining four, these points were excluded from the linear fit. In both representations, inclusion of all data points resulted in smaller slopes and a poor overall fit to the data. The deviation of the AuNP@PS with $PS_{6.5}$ and PS_{18} ligands from the linear trend can be related to particle aggregation, which may have affected both DLS and AUC measurements. This has been discussed in more detail in sections 6.4 and 6.5. For particles with ligands from PS_{21} to PS_{33}, there is good agreement with the linear fits. However, the data appears to exhibit a more systematic deviation from perfect linearity for the good solvent case in **Figure 45 a** than for the θ solvent case in **Figure 45 b**. The slopes are 1.2 and 2.2, respectively, whereas a slope of 1 would indicate good agreement with theoretical scaling in either case. For the good solvent SDPB scaling, a slope > 1 is unphysical and conflicts with the concept of semi-dilute conditions, as the scaling of the free chains in good solvent ($\nu \approx 3/5$) should be retained. For the θ solvent case, the large slope indicates poor agreement with SDPB scaling. Nevertheless, since the free chains scale almost ideally in DMF at room temperature, better agreement with the θ solvent SDPB scaling should be expected. The observation that the measured height scales significantly steeper than the θ solvent SDPB suggests that the brush is more concentrated and the polymer chains are more confined.

As the SDPB model does not seem to describe the scaling of the AuNP@PS, we now turn towards the evaluation according to the CPB model. As mentioned in Section 2.3, higher order interactions in the CPB regime render the solvent quality inconsequential for brush scaling. Moreover, the local flatness of dense curved brushes allows the formulation of a universal scaling law for flat and curved brushes in both good and θ solvents. Theory predicts scaling as $H \propto N\sigma^{1/2}$, whereas experiments and simulation may account for transitional behavior by means of an additional scaling factor, α, to obtain $H \propto (N\sigma^{1/2})^{\alpha}$.[81] As shown in **Figure 46**, plotting the brush

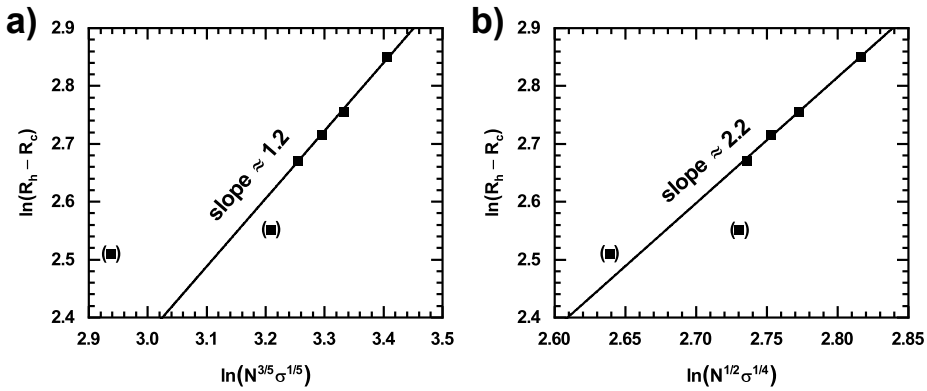

Figure 45: Double-logarithmic plots of the experimental hydrodynamic brush height of AuNP@PS in DMF according to semi-dilute brush scaling in a) good solvent and b) θ solvent. The first two points in brackets were excluded from the linear fits.

height accordingly yields a linear relation for the brush height of AuNP@PS with ligand molecular weights between 21 and 33 kg/mol. This is not surprising, as the CPB scaling resembles SDPB scaling in θ solvents, introducing only an additional factor of 2 in the log-log representation. Although the slope of 1.1 slightly exceeds the theoretical maximum of $\alpha = 1$, this result can be considered to be in good agreement with the CPB model. This is particularly true due to the range of grafting densities and the near-θ solvent conditions.

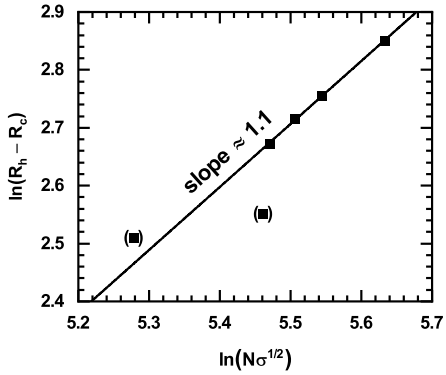

Figure 46: Double-logarithmic plot of the experimental hydrodynamic brush height of AuNP@PS in DMF according to concentrated brush scaling. The first two points were excluded from the linear fits.

Having identified the CPB as the most likely scaling regime, we attempt to model the structure of the polymer brush. Due to the presumed high polymer volume fractions, the classic concept of a brush constructed of a sequence of blobs has to be abandoned. Firstly, the blob size at high grafting densities becomes sufficiently small to only accommodate a very small number, g, of statistical segments. Moreover, even ideal chains experience significant stretching under such conditions. Hence, chain statistics deviate significantly from those of unperturbed chains, regardless of solvent quality.
In order to provide a more realistic model of the brush morphology, we employ a model of a brush filled by polymer chains with a continuous volume fraction profile, $\phi(z)$, rather than discrete blobs. $\phi(z)$ will be modeled according to an analytical approximation of SCFT result found in literature.[144]

$$\phi(z) = \phi(0)\left[1 - \left(\frac{z}{H}\right)^2\right]^{1/2} \qquad 0 \leq z \leq H \tag{87}$$

For $\phi(0)$ we will use the value according to Equation 30, i.e. $\phi(0) = \sigma^{1/2}b$. The corresponding volume fraction profiles are shown in **Figure 47 a**. The volume fraction profiles demonstrate the very gradual decrease of ϕ over a wide range of z, which is the result of higher order chain-chain interactions. For $PS_{6.5}$ and PS_{18} the initial volume fractions $\phi(0)$ are unphysically high, which complies with other data that suggests aggregation and therefore inaccurate values of H and σ. In general, AuNP@PS that are in good agreement with CPB scaling also yield plausible volume fraction profiles. There appears to be a mutual cross-over point at $z \approx 11 - 12$ nm.
We now define a distance dependent brush cross-section $A(z)$, which simply is the virtual surface area of a sphere with radius $R + z$, where R is the radius of the gold core.

$$A(z) = 4\pi(R + z)^2 \tag{88}$$

The total volume of the brush up to its full height H can be written as the integral of $A(z)$ over all z, shown in Equation 89.

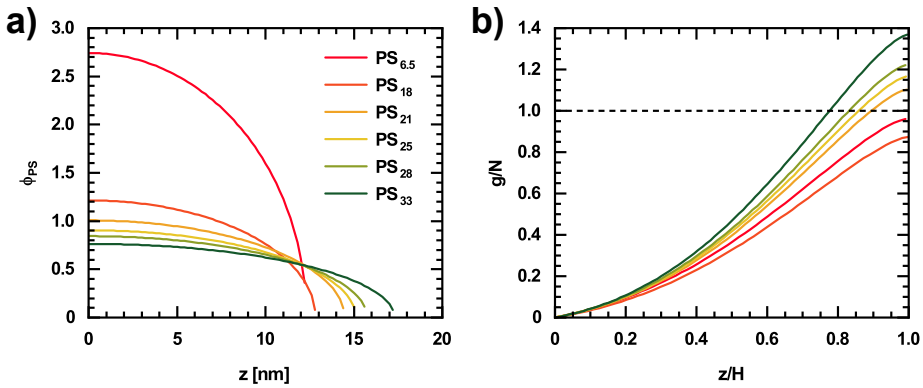

Figure 47: a) Polymer volume fraction profiles according to Equation 87. b) Cumulative segment number g relative to the experimental degree of polymerization N in relation to the relative height, z/H

$$V(H) = \int_0^H A\, dz = 4\pi \int_0^H (R+z)^2 dz \tag{89}$$

Correspondingly, the total volume of polymer, $V_{\mathrm{PS}}(H)$, is the brush volume, $V(H)$, weighted by the volume fraction, $\phi(z)$.[85]

$$V_{\mathrm{PS}}(H) = 4\pi \int_0^H \phi(z)(R+z)^2 dz \tag{90}$$

Inserting the expression from Equation 87, yields Equation 91.

$$V_{\mathrm{PS}}(H) = 4\pi\, \phi(0) \int_0^H \left[1 - \left(\frac{z}{H}\right)^2\right]^{1/2} (R+z)^2 dz \tag{91}$$

Finally, we determine the number of segments per chain, $g(H)$, using the segment volume, $V_{\mathrm{seg}} = V_{\mathrm{m}}/N_{\mathrm{A}}$, where V_{m} is the molar volume of the monomer. Normalization of the polymer volume to the number of chains per particle, f, is also necessary, with $f = 4\pi\sigma R^2$

$$g(H) = \frac{V_{\mathrm{PS}}(H)}{V_{\mathrm{seg}}\, f} = \frac{V_{\mathrm{PS}}(H)}{0.165\mathrm{nm}^3\, 4\pi\sigma R^2} \tag{92}$$

We can now verify the validity of the model if we plot g/N versus z/H, as shown in **Figure 47 b**. If the model accurately describes the AuNP@PS system in DMF, g should reach the full degree of polymerization, N, at $z = H$. This holds true for most particle batches within a margin of error of 20%. Only particles with PS_{33} ligands exhibit a larger deviation of approximately 40%. There seems to be a trend in the behavior, with g/N at $z = H$ increasing with molecular weight. The plot also illustrates that the outer layers of the brush contain the majority of chain segments, despite the larger volume fraction at small z. At this point it should be emphasized that the results of this approach strongly rely on the choice of $\phi(0)$. We used the conventional definition of $\phi(0) = \sigma^{1/2}b$.[85] The fact that the model seems to overestimate g, may indicate that the grafting densities are slightly lower than determined by AUC.

We will now turn to the thermodynamic aspects of the brush under these conditions. For simplicity, calculations will be averaged over an entire grafted chain, rather than using a SCFT approach to obtain local values along the chain. The CPB model is derived from the minimization of the free energy in relation to elastic and osmotic contributions. In the CPB regime, we can assume near-ideal behavior for the chains in the brush. For ideal chains, the free energy of elastic stretching, F_{el}, in relation to brush height is given by Equation 93.[57, 144] As shown, F_{el} scales with the square of the brush height.

$$\frac{F_{\mathrm{el}}}{k_{\mathrm{B}}T} = \frac{H^2}{b^2 N} \tag{93}$$

The osmotic contribution to free energy can be derived from the free energy of mixing. F_{mix} is given by the Flory-Huggins solution theory (Equation 1 in section 2.1). The osmotic pressure, Π, of a polymer solution (or within a brush) is the derivative of F_{mix} regarding volume.

$$\Pi = \frac{\partial F_{\mathrm{mix}}}{\partial V} \tag{94}$$

From a virial expansion of the Flory-Huggins equation followed by differentiation, we obtain Equation 95.[57] The first term in brackets becomes negligible for large N and

can be disregarded. The second term corresponds to excluded volume, i.e., two-body interactions and should vanish in θ conditions. The final term corresponds to three-body interactions.

$$\frac{\Pi}{k_\mathrm{B}T} \approx \frac{1}{b^3}\left[\frac{\phi}{N} + (0.5-\chi)\phi^2 + \frac{1}{3}\phi^3\right] \tag{95}$$

The osmotic energy is the product of Π and V. As we consider the free energy per chain, we use the brush volume per polymer chain, given by Equation 96. Here, R is the radius of the core particle and σ is the grafting density.

$$V = \frac{1}{3R^2\sigma}\left[(H+R)^3 - R^3\right] \tag{96}$$

Thus, the osmotic free energy per chain, F_os, can be expressed as shown in Equation 97.

$$\frac{F_\mathrm{os}}{k_\mathrm{B}T} \approx \frac{1}{3R^2\sigma b^3}\left[(H+R)^3 - R^3\right]\left[\frac{\phi}{N} + (0.5-\chi)\phi^2 + \frac{1}{3}\phi^3\right] \tag{97}$$

The average volume fraction ϕ of polymer is the volume of one polymer chain divided by the brush volume per chain. This is shown in Equation 98, where V_seg is the volume of one monomer unit.

$$\phi = \frac{V_\mathrm{seg}N}{V} = \frac{0.165\,\mathrm{nm}^3 N}{V} \tag{98}$$

The total free energy of the brush is the sum of elastic and osmotic contributions.

$$F_\mathrm{tot} = F_\mathrm{el} + F_\mathrm{os} \tag{99}$$

Figure 48 a shows the free energy profiles in relation to brush height for the six different batches of AuNP@PS. The brush height, at which the minimum occurs, increases with increasing molecular weight of the ligands, whereas the free energy at the minimum decreases with increasing molecular weight. The latter effect is probably caused by the higher grafting densities found for the shorter chains, as the minimum free energy is significantly higher for AuNP@$PS_{6.5}$, for which the calculated σ also is much higher than for the other five particle batches. **Figure 48 b** shows the positions

of the minima in relation to chain length in the double-logarithmic representation according to the CPB regime, which was introduced in **Figure 46**. The experimental data from that graph is also shown here for comparison (black squares). The modeled brush height (red triangles) follows a linear trend similar to the experimental data. The slopes of the linear fits are virtually identical but the model is offset towards larger brush height. The offset in the double-logarithmic graph corresponds to a constant factor between modeled and experimental brush height with $\Delta H = \exp[\Delta \ln(H)] \approx 1.6$. This discrepancy can be attributed to the simplistic calculation and the potential overestimation of σ from AUC measurements, discussed earlier. Both factors increase the average polymer volume fraction and exaggerate the osmotic contribution. The distinct value of the offset could also be further indication for the underestimation of H from DLS measurements, which was discussed in the beginning of this section.

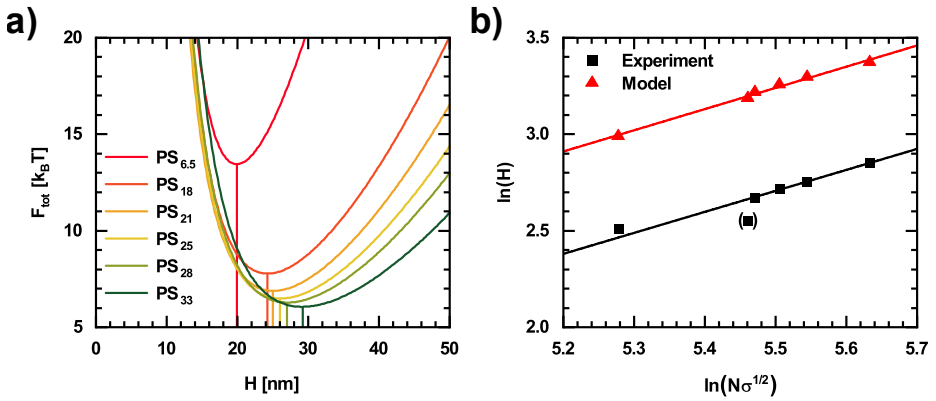

Figure 48: a) Total free energy per chain in relation to brush height calculated from elastic and osmotic contributions. The minima are indicated by drop lines. b) Scaling analysis of experimental (black squares) and modeled (red triangles) brush height in relation to chain length and grafting density. The modeled brush height scales with the same slope as the experimental data but is offset.

We can conclude that the brush of the AuNP@PS scales in the CPB regime. Within the margin of error, the experimental brush height scales with $N\sigma^{1/2}$. Moreover, an approximation of the volume fraction profiles for concentrated brushes is in good agreement with the experimental chain lengths and grafting densities. Unphysical values were obtained for AuNP@PS with $PS_{6.5}$ and PS_{18} ligands, which could be

a result of particle aggregation and overestimation of grafting densities. A detailed analysis based on the thermodynamics of the brush further demonstrated the good agreement between experimental and theoretical brush heights. It also suggests that the real brush height may be significantly larger than determined by DLS, which would also explain the overestimation of grafting densities. This is consistent with the large volume of the brush compared to the core particle. Although the combination of DLS and AUC used for this work certainly provides a good insight into the scaling regime, the absolute values obtained may differ from the real ones. More accurate values for brush heights and volume fraction profiles will only be accessible with small angle neutron scattering experiments, which are time-consuming and costly.

8 Functionalization of non-spherical particles with PS ligands

Whereas previous sections were limited to a discussion of polymer brushes on spherical AuNPs, the nature of the ligand exchange method developed within this thesis suggests a certain degree of universality regarding particle size and shape. Unlike with direct phase transfer methods, the particles are not required to penetrate a phase boundary and remain stabilized while doing so. In addition, syntheses of non-spherical AuNPs often are template-based methods in aqueous media and direct synthesis in organic solvents may not be possible for any desired particle morphology. Thus, hydrophobically stabilized non-spherical NPs are arguably even more difficult to obtain than their spherical counterparts. In order to evaluate the applicability of the two-step ligand exchange method to non-spherical particles, the functionalization of gold nanocubes (AuNCs) and gold nanorods (AuNRs) was tested. Both, AuNCs and AuNRs, were prepared by aqueous synthesis. Compared to the spherical AuNPs tested, the AuNCs and AuNRs are much larger. The AuNCs have an edge length of 87 ± 7 nm, whereas the AuNRs possess a length of 50 ± 10 nm and a diameter of 9.4 ± 0.5 nm, respectively. The ligand exchange itself was carried out in the same fashion as for spherical AuNPs, accounting for the respective surface area and amount of ligand required. Due to the much smaller surface-to-volume ratio of the AuNCs and AuNRs compared to the AuNPs functionalized previously, a smaller amount of PS-SH ligand was typically required.

In general, the ligand exchange was successful. AuNC@PS and AuNR@PS with ligand molecular weight ranging from 6.5 and 33 kg/mol were obtained. **Figure 49** shows exemplary TEM images of AuNC and AuNR functionalized with PS_{28} ligand. The TEM images highlight the significant difference in particle size, also in comparison to the spherical particles discussed earlier. In the case of AuNC@PS_{28} in **Figure 49 a**, the ligand shell is clearly visible. Due to the large particle size, the polymer layer seems thin. Variations in layer thickness may be a result of sample drying, although difference between grafting densities on different particle facets are also plausible.

For AuNR@PS_{28} in **Figure 49 b**, the ligand shell is not as visible. An indirect indication for its presence and the successful stabilization of the AuNR is the lack of parallel stacking, which is typical for surfactant stabilized rods. Instead, the AuNR are randomly scattered and overlay in some cases. The image also shows a number of spherical particles, which are a side product of AuNR synthesis and difficult to remove entirely.

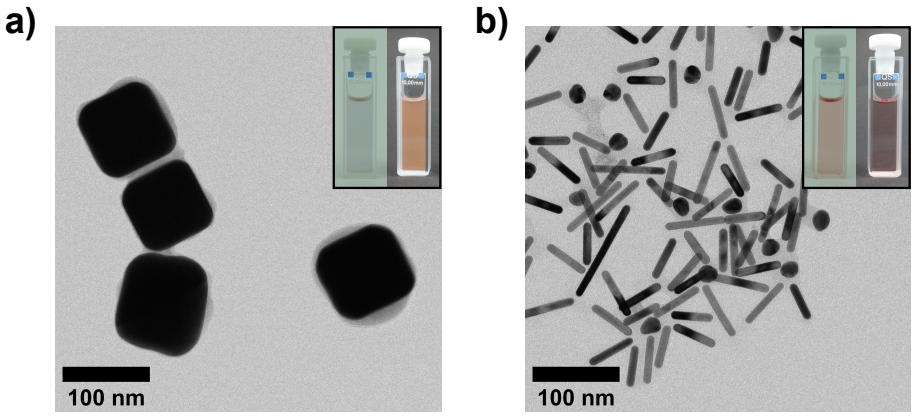

Figure 49: a) TEM image of AuNC@PS_{28} with the polymer clearly visible on the particle surface. b) TEM image of AuNR@PS_{28}. The insets show photographs of AuNC@PS and AuNR@PS dispersed in DMF with bright and dark backgrounds respectively.

The insets in **Figure 49** show photographs of dispersions of AuNC@PS and AuNR@PS in DMF respectively. A bright and a dark background were chosen to highlight specific characteristics of the different particles. Large AuNC mainly scatter light, which can be seen most clearly with a dark background. AuNR, on the other hand, are similar in appearance to spherical AuNP, as the main LSPR band lies outside the visible wavelength range. **Figure 50** shows the UV/Vis absorbance spectra of AuNC@PS and AuNR@PS in DMF. The differently colored spectra correspond to the molecular weights of the ligands, from 6.5 kg/mol in red to 33 kg/mol in dark green. The spectra for AuNC@PS in **Figure 50 a** are very similar across different ligand molecular weights. Compared to the spectra of spherical AuNP@PS in **Figure 24**, the LSPR

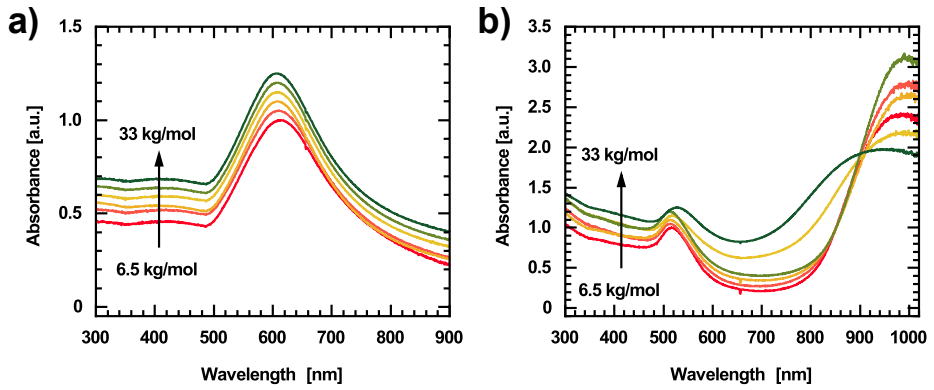

Figure 50: a) Normalized UV/Vis absorbance spectra of AuNC@PS in DMF. b) UV/Vis absorbance spectra of AuNR@PS in DMF, normalized to the transverse LSPR mode peak. In both panels the spectra for different molecular weights of PS ligand are offset along the y-axis.

peak is shifted towards longer wavelengths and broader, which is a result of the larger size of the AuNCs. The spectra suggest that the AuNC@PS are equally well stabilized, regardless of the ligand length. A slightly different observation can be made for the spectra of AuNR@PS in **Figure 50 b**. These spectra were normalized to the transverse LSPR mode, here found at wavelengths between 500 and 550 nm. Whereas the transverse mode appears similar between the different ligand molecular weights, the longitudinal modes in the red and near-infrared part of the spectrum differ significantly. Firstly, the longitudinal modes for AuNR functionalized with PS_{25} and PS_{33} ligands are much broader than those of the other four samples. Secondly, the absorbance ratios between longitudinal and transverse modes do not follow a trend with regard to ligand length. For PS_{25} and PS_{33}, the absorbance ratio is 1.7 and 2.1, respectively, whereas the ratio is between 2.4 and 3.0 for the other molecular weights. Both observations hint towards differences in the stability between particle batches, as broadening of the LSPR relative to peak intensity is typically observed during particle aggregation. In other words, AuNR@PS_{25} and AuNR@PS_{33} seem to be less stabilized than the other batches of AuNR@PS.

The behavior of AuNC@PS and AuNR@PS dispersed in toluene allow further observations. The corresponding UV/Vis spectra are shown in **Figure 51**. For AuNC@PS,

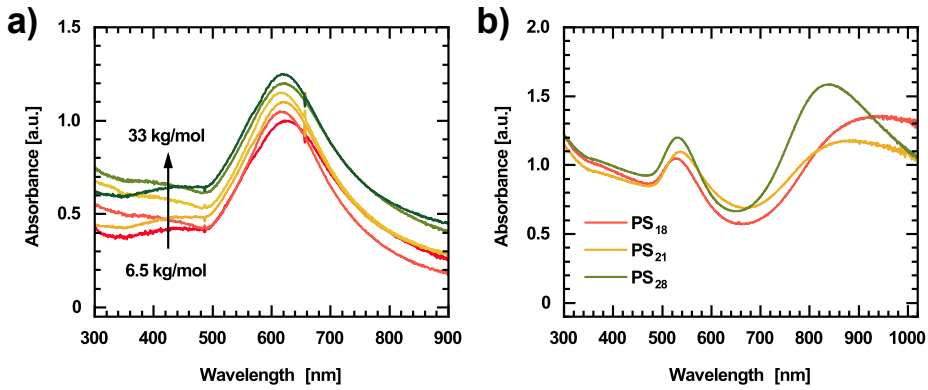

Figure 51: a) Normalized UV/Vis absorbance spectra of AuNC@PS in toluene. b) UV/Vis absorbance spectra of AuNR@PS in toluene, normalized to the transverse LSPR mode peak. In both panels the spectra for different molecular weights of PS ligand are offset along the y-axis.

the spectra are similar to those measured in DMF, although larger irregularities between ligand lengths can be observed, indicating slight differences in stabilization. In contrast, only one half of the batches of AuNR@PS could be stabilized in toluene at all, including those functionalized with PS_{18}, PS_{21}, and PS_{28}. Notably, AuNR@PS_{25} and AuNR@PS_{33}, which already exhibited deviations from the general trends when dispersed in DMF, are not among the batches stabilized in toluene. Additionally, there is no clear trend for stabilization in toluene regarding the molecular weight of the ligands, which suggests that the observed differences in stabilization are a result of batch-to-batch variation, rather than a systematic effect related to ligand length. As a whole, all these observations are in agreement with those made for spherical AuNP@PS, which also appear to be less stabilized in nonpolar solvents, such as toluene. In the case of AuNR@PS, it could be possible that the grafting density at the sides of the rods is relatively low, such that the AuNR are more prone to aggregation. Another aspect is the fairly small diameter of the rods, which results in large curvature of the brush, compared to the spherical AuNP. The larger divergence of polymer volume fraction with distance from the surface of the rods may promote attractive interactions, as observed in SAXS measurements of AuNP in dioxane in section 6.6.

Overall, the experiments have shown that the ligand exchange protocol can be ap-

plied to non-spherical AuNP of considerably larger size than the Turkevich particles used in most of this thesis. The insufficient stabilization of AuNR, in particular in toluene, may be linked to the geometry of the grafting surface. The range of molecular weights of ligands available may have been inappropriate for sufficient stabilization of such large particles. Despite these issues, the method has significant potential, which should be explored for other particles sizes and geometries in the future. A generalized approach for the functionalization of a broad variety of particle types may have great implications for the development and screening of functional nano-composite materials.

9 Kinetics of polymer ligand binding

9.1 Implications of ligand binding kinetics for brush structure

The previous sections, in particular the discussion of the scaling of the brush height in relation to N and σ, have demonstrated a strong dependence of the grafting density on the chain length of the ligands. As the molar concentration of PS during the ligand exchange was identical for all molecular weights, the ligand exchange procedure appears to follow an intrinsically self-limiting mechanism. Doubtlessly, one cause of this limitation are the high polymer volume fractions achieved near the particle surface. Higher grafting densities would further increase the osmotic pressure within the brush and require further stretching of the PS chains to compensate. This seems energetically unfavorable. Equally, high polymer volume fractions increase the barrier for a chain to diffuse and attach to the particle surface. An investigation of the kinetics of the polymer ligand binding process can help understand the formation mechanism and the influence of ligand molecular weight on the brush structure. We will consider the binding of long, end-functionalized polymer chains as a reversible adsorption process. In equilibrium, the number of adsorbed chains should be related to the concentration of chains in the bulk phase, the surface coverage, i.e., grafting density, and the adsorption enthalpy. The adsorption process in brush formation ideally is specific to the functional chain end, whereas the chain itself and therefore the majority of the molecule does not interact with the surface. Nevertheless, the polymer chain can play a significant role in brush formation, as chain-chain interactions strongly contribute to the energetic landscape of the process. In a way, brush formation therefore is a three-dimensional sorption process rather than a typical, two-dimensional one. Correspondingly, the kinetics of this process are rather complex and only few theoretical models haven been proposed so far, notably the one by Christian Ligoure and Ludwik Leibler.[145] Their approach is characterized by a time-variable potential barrier created by the forming brush, which new chains have to penetrate in order to reach the surface. This leads to a complex, numerical description of the adsorption kinetics. Depending on the starting and equilibrium conditions, they identify several regimes in which the numerical results can be approximated by much simpler, analytical solutions. As will

be demonstrated in this section, low ligand concentrations and correspondingly low grafting densities allow such simplifications.

9.2 Approach for binding kinetics measurements

In the previous section, the optical properties of AuNP@PS were discussed, in particular regarding the refractive index of the environment. Since ligand binding induces a change of the local refractive index, utilizing the LSPR wavelength to monitor binding kinetics would represent an elegant experimental approach, that does not require any modifications to the particles or polymers. There are, however, certain limitations. The single-phase ligand exchange mechanism requires AuNPs to be decorated with PVP as auxiliary ligand. Although a change in refractive index may still occur during the exchange of PVP with PS, the change will be small compared to the change observed for a brush forming on a bare particle surface. Moreover, in order to accurately replicate the conditions under which the ligand exchange takes place, the concentration of PS ligands in the bulk phase has to be high, further reducing the refractive index contrast between the bulk phase and the forming brush. Consequently, the LSPR shift expected during such an experiment would be fairly small. Other effects, such as particle aggregation, also affect the absorbance spectrum and are difficult to correct for. An absorbance-based kinetic experiment using an unmodified system under similar conditions as the preparative exchange process is therefore not feasible. Better sensitivity could be achieved using an easily measurable property of a modified system. Fluorescently labeling the PS ligands introduces a very specific optical property that is unique to the PS ligands without interfering with the kinetically relevant parts of the ligand, i.e., the surface-binding end-group and the main chain material. Additionally, fluorescence detection usually is very sensitive and reliable over a wide range of signal intensities. In order to monitor kinetics, the fluorescence properties of the label must change during the binding process, which is achieved by the strong optical interaction between plasmonic AuNPs and fluorophores. Both, self-quenching of adjacent dye labels of bound ligand chains as well as non-radiative energy transfer from the fluorophore to the particle are relevant mechanisms.[146] Efficient quenching of the dye labels near the particle surface is achieved, if there is sufficient spectral

overlap between the emission of the dye and the LSPR of the particle. However, the strong absorbance of AuNPs gives rise to an inherent issue regarding fluorescence measurements, namely a strong *inner filter effect*. The molar extinction coefficient of AuNPs is several orders of magnitude larger than that of a typical organic dye, such that the AuNPs absorb a much larger fraction of the incident light than the dye. Consequently, the emission intensity is greatly reduced, in particular if AuNPs and dye are present in similar concentrations. The magnitude of the inner filter effect is a function of concentration, wavelength, and path length. Moreover, a strong inner filter effect also changes the shape of the emission spectrum.

Due to the strong inner filter effect under the desired experimental conditions, the kinetic investigation in bulk was not considered feasible. Instead, the AuNPs were immobilized on a glass substrate that was kept outside the light path. The decrease of fluorescence intensity in the bulk phase, containing the dye-labeled ligand chains, was measured as the ligands bind to the particle surface. Knowing the starting concentration of ligand and the number of AuNPs on the substrate, absolute values for bulk ligand concentration, and number of bound ligands per AuNPs can be calculated for each point in time. The primary aims of this series of experiments were to investigate the influence of ligand molecular weight and the mechanism of ligand binding.

9.3 Immobilization and characterization of AuNPs on glass substrates

For the immobilization of AuNPs on glass substrates, AuNPs were prepared according to the inverse Turkevich method described in Section 5. These particles were not functionalized with PVP and kept in aqueous dispersion. Glass substrates were treated with RCA-1 solution to clean and activate the surface, which was then functionalized with APTMS to introduce amine groups on the surface. These amine groups aid in the irreversible adsorption of AuNPs via electrostatic interactions and specific, covalent binding to the AuNP surface. Once the AuNPs are bound, the residual amine groups have to be removed or capped, in order to avoid interactions between the ligands and the surface. A scheme of the process is shown in **Figure 52**.

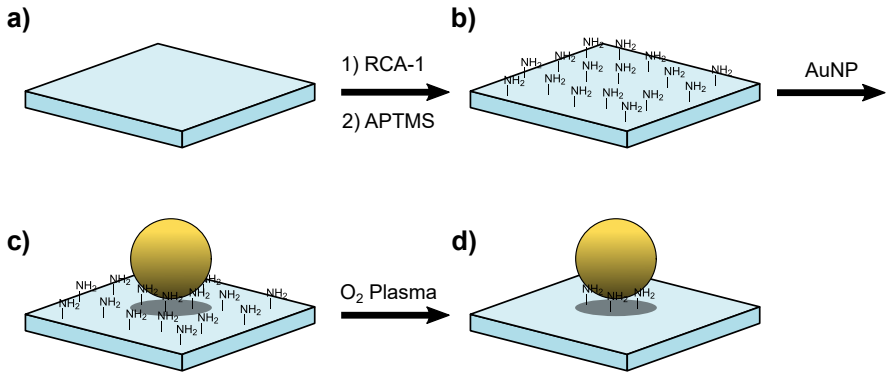

Figure 52: Preparation scheme for substrate-supported AuNPs. a) Glass substrates have oxygen rich surfaces which are activated by RCA-1 cleaning. b) Functionalization with APTMS results in amine functionalized glass surfaces. c) The AuNPs adsorb onto the surface and are held by coordination of amine groups and van-der-Waals forces. d) Plasma treatment removes exposed amine groups.

A homogeneous and reproducible surface coverage with AuNPs was required for this experiment, as all parameters, except for the ligand molecular weight, were to be kept constant. The silanization and proper cleaning of the substrates before applying the AuNPs was found to be critical. A rough APTMS layer or residues of excess APTMS caused quick aggregation of AuNPs during the application step. In order to address these issues, the silanization protocol was optimized for short incubation times at room temperature by acetic acid catalysis. Formation of APTMS aggregates was suppressed by thoroughly drying the activated glass slides and staining chambers used for the functionalization and by usage of high-purity methanol as solvent. The curing and cleaning procedure included multiple stages of sonication in ethanol and water. The final surfaces were smooth and showed a high affinity for binding AuNPs. Despite amine functionalization on both sides of the substrates, only one side was supposed to be loaded with AuNPs. Therefore, one side of the substrates was covered with AuNP dispersion. The concentration of this dispersion was chosen for quantitative adsorption of AuNPs to be possible, thus increasing reproducibility. In order to find a good compromise between a high particle number density and sufficiently large inter-particle distances, a series of particle deposition experiments from dispersions

of different concentrations was conducted. **Figure 53 a** shows the particle number densities of AuNPs measured by AFM in relation to the theoretical number of AuNPs added per μm^{-2} of substrate surface area, as estimated from the absorbance of the AuNP dispersion.[109, 110] The data exhibits a roughly linear correlation between predicted and measured particle numbers. Overall, the calculated and measured particle number densities are in a very similar range. However, there appear to be some systematic discrepancies. The negative offset of measured compared to calculated particle numbers and the slope of approximately 1.2 indicate some degree of inaccuracy in the calculation of particle numbers from absorbance spectra. Additionally, the particles tended to aggregate at very low concentrations, which may have been caused by the low buffer capacity of such dilute dispersions. Thus, the particles are more sensitive to pH changes and impurities on the surface and prone to aggregation. At the same time, excessively high particle concentrations lead to incomplete adsorption. Therefore, the system seems to exhibit a threshold behavior at low concentrations and saturation at high concentrations.

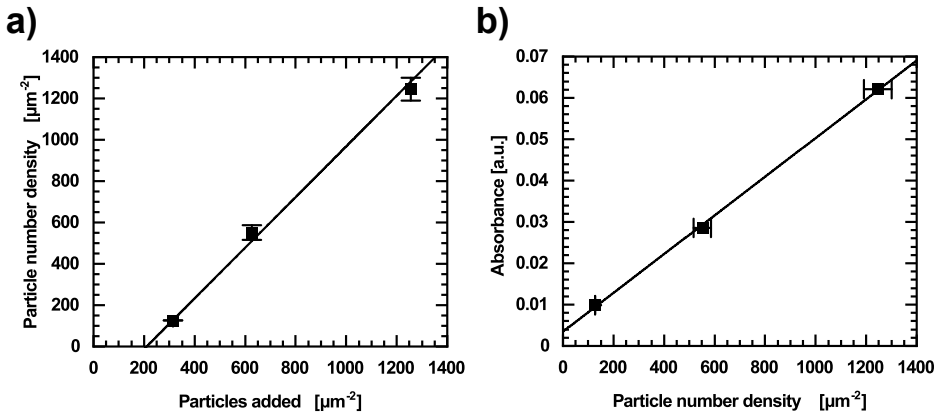

Figure 53: a) Particle number density of AuNPs on amine-functionalized glass substrates measured by AFM in relation to the estimated particle number added per surface area. b) Absorbance intensities of the LSPR maximum of AuNP immobilized on amine-functionalized glass substrates.

Figure 53 b shows the absorbance at the LSPR maximum measured by UV/Vis spectroscopy of substrates functionalized with different concentrations of AuNPs. During

the measurements, the samples were immersed in toluene for refractive index matching, as an inhomogeneous refractive index environment (in this case the glass/air interface) adversely affects the plasmon excitation. As expected, the absorbance values are fairly low and correspond to transmission values larger than 85%. Within the range of concentrations used, the LSPR absorbance intensity is almost proportional to the particle number density from AFM measurements. Hence, the Lambert-Beer law applies for these particle number densities. Due to plasmon coupling, the absorbance spectrum changes at small interparticle distances, i.e. high particle number densities, and the proportionality vanishes. This experiment also confirms the homogeneity of the samples, as the AFM data, which has a rather small statistical sample size, correlates well with the ensemble averaged UV/Vis data. A particle number density of 600-800 μm^{-2} was chosen as ideal compromise between large particle surface area and sufficient interparticle distance. In the following, the reproducibility and homogeneity of the samples used for the kinetic investigation is discussed in more detail. Five glass slides were covered with AuNP dispersion and AFM images were measured in the center and towards the edge of each substrate. Sample homogeneity can be divided into two criteria. On one hand, inhomogeneity can describe the difference in particle number densities near the center and the edge of the substrate, respectively. On the other hand, the order and distribution of particles within one small scan region can be more or less homogeneous, for instance due to cluster formation. In contrast to this, reproducibility describes the the similarity of the average particle number densities and structural homogeneity between individual samples. First, we will focus on the homogeneity within each sample and reproducibility between samples. **Figure 54 a** shows a bar chart of the particle number densities determined from all measured AFM images. The data is grouped into two scans measured on each of the five samples.
The values for the particle number density range from approximately 600 to 750 μm^{-2}, with most values between 650 and 700 μm^{-2}. The average particle number density and standard deviation are 684 ± 40 μm^{-2}, as indicated by the dashed horizontal line and gray area, respectively. There is no significant variation between individual samples, indicating good reproducibility. Additionally, a first coarse assessment of the homogeneity withing each sample suggests that there is no systematic difference

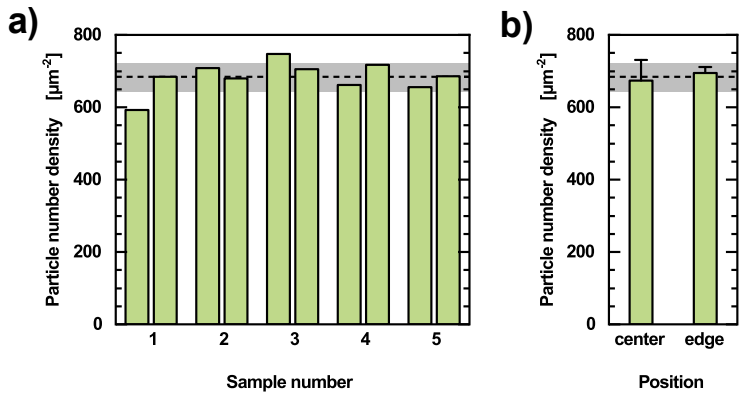

Figure 54: a) Particle number density of AuNPs on amine-functionalized glass substrates measured by AFM. Two scans per sample were measured. b) Average particle number densities and standard deviation near the center and near the edge of all substrates, respectively. The dashed horizontal line and gray area represent the total average from all scans on all substrates and the corresponding standard deviation, respectively. Reproduced from Ref. [147] with permission from the Royal Society of Chemistry.

between particle number densities in center and edge regions of the samples. This is further demonstrated in **Figure 54 b**, which shows the average number densities of all center and all edge scans and corresponding standard deviations, respectively. The values are 673 ± 52 µm^{-2} for the center scans and 695 ± 15 µm^{-2} for edge scans. Whereas the average values are similar and close to the overall average, the standard deviations are very different. This is caused by the very low particle number density for the center scan of sample 1. Overall, there is no significant difference between center and edge positions.

We will now take a closer look at the local homogeneity and order of the samples. Only the first sample will be discussed in detail here. The data for the remaining samples can be found in the **Appendix**. As sample 1 showed the largest difference in particle number density between the two scan regions, a difference in the order and homogeneity may be observed. **Figure 55** shows AFM height images and image analysis for the first sample. The left and right half correspond to the center and edge region, respectively.

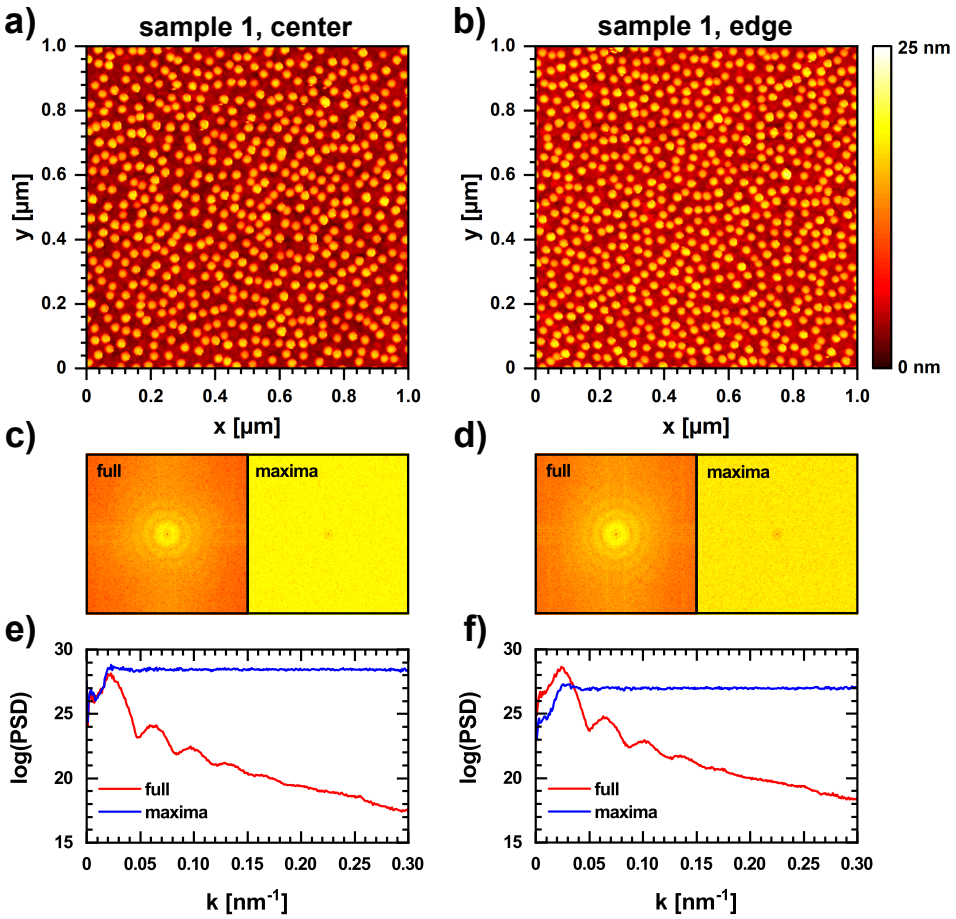

Figure 55: a – b) AFM height images of the center and edge region of sample 1 of a series of AuNP on amine functionalized glass substrates. c – d) FFTs of the same height images (full) and of the particle position maps (maxima). e –f) Power spectral density (PSD) curves obtained from radial averaging of the FFTs around the center point. Whereas the FFT of the full AFM image contains features related to the particle size, the FFT of the position map is almost flat, indicating the absence of order in the particle arrangement. Reproduced from Ref. [147] with permission from the Royal Society of Chemistry.

Despite the discrepancy in particle number density, there is no visible structural difference between the particle arrangement in the scans. The FFTs of the height images both exhibit concentric rings. These FFTs comprise a convolution of particle size and shape as well as structural parameters of the arrangement, similar to form and struc-

ture factors in scattering. In order to isolate the structural information, the AFM images are reduced to a map of particle positions by automated detection of height maxima. The FFTs of these particle maps are also shown. In contrast to the FFTs of the full image, there are no features apart from a region of reduced probability in the center of the FFT. The difference between the FFTs of full images and height maxima maps is further demonstrated by **Figure 55 e** and **f**. These plots show the power spectral density (PSD) functions, which were generated by radial averaging of the FFTs. The PSD indicates the presence of correlation and periodicity in relation to the wave vector, $k = \lambda^{-1}$. Small k correspond to long-range correlation and vice versa. In the PSD representation, the absence of correlation between particle positions is highlighted by the flat PSD profiles. We can therefore deduce that the concentric rings in the FFTs of the full images simply are a result of the consistent particle size. The particles assume neither a crystalline nor glassy state, as there is no preferred nearest-neighbor distance, which would express as a single ring in the FFT. Apart from the constraint of finite particle size, the particles form a random arrangement without a preferred distance. Within the range of particle number densities of this sample series, this random arrangement is retained. The samples therefore exhibit a high degree of structural homogeneity. In conjunction with excellent reproducibility, these samples are well suited for the kinetics experiments.

9.4 Kinetic measurements and analysis

The kinetics experiments were conducted using $PS_{6.5}$, PS_{21}, and PS_{33} ligands. These were partly functionalized with ATTO 488 fluorescent dye, a Rhodamine derivative, by copper-free azide-alkyne coupling. The degree of labeling was below 10%, as full labeling increases the chance of undesired electrostatic interactions between the charged dye moieties of adjacent chains. **Figure 56** shows normalized fluorescence spectra of PS_{21}-ATTO488 in DMF. The emission and excitation spectra show the typical line shape and mirror symmetry of Rhodamine derivatives, which are a result of the Franck-Condon principle for transition probabilities.[148] The fluorescence maxima are at wavelengths of 513 and 533 nm for excitation and emission, respectively, representing a redshift of 13 nm compared to the reference value in water, while the Stokes shift of 20 nm is retained. Rhodamine derivatives are known for their solvatochromism and sensitivity towards their chemical environment. Although the ATTO line of Rhodamine derivatives mitigates these effects, they still are are partly present. In order to minimize the influence of such effects on the kinetics measurements, spectra were measured in synchronous mode. In this mode, excitation and emission wavelength are scanned simultaneously, using a fixed wavelength offset which typically is chosen as the Stokes shift. As shown in **Figure 56**, synchronous scans of Rhodamine derivatives create a very symmetrical Gaussian peak, which can be easily fitted to increase accuracy of intensity and wavelength determination. Due to the narrowness of the peak, scans can be performed over a smaller wavelength range and therefore faster than a full scan of the broad emission peak, improving the temporal resolution. Additionally, spectral features originating from other sources, that exhibit a different Stokes shift, are screened by synchronous measurements. For instance, Raman peaks of the solvent can have a major contribution to the measured fluorescence intensity of very dilute dye solutions.

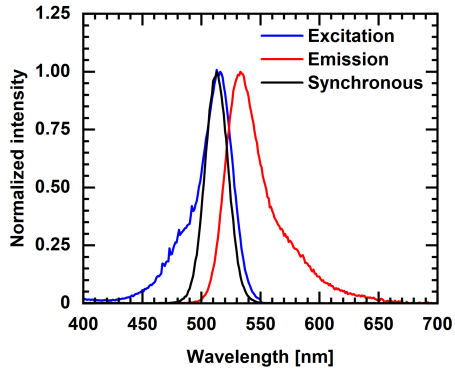

Figure 56: Fluorescence spectra of PS_{21}-ATTO488 in DMF. Reproduced from Ref. [147] with permission from the Royal Society of Chemistry.

Figure 57 shows the fluorescence intensity curves for the kinetics experiments with $PS_{6.5}$, PS_{21}, and PS_{33} ligands. The first row, **a** – **c**, shows the raw fluorescence intensity, which was defined as the fitted height of the peak in the synchronous scan, for the entire duration of the experiments in a lin-lin representation. As the experiment was repeated three times with each molecular weight of the ligand, the data for a total of nine runs is shown. For better clarity, the curves are offset by 2000 counts. Qualitatively, all curves exhibit a similar progression. Apart from the deliberate offset, the intensities at $t = 0$ were similar. Differences originate from a varying degree of dye labeling. There are some fluctuations and sudden steps in the intensity profiles. Potential causes include condensation on the outside of the quartz cells, contaminants detached from the sample, and fluctuations of the light source and detector due to extended operating times. In some instances, a continuous but slow increase of intensity over time was observed. This was attributed to changes of the properties of the solution, for instance pH changes as a result of leakage of contaminants from the substrates. This is also supported by a sudden shift of the peak wavelength that frequently appeared after the substrates were immersed in the solutions. Additionally, chemical changes of the dye-labeled polymers may have occurred, such as hydrolysis of the polymer-dye bonding by free amine residues in the DMF used. Fitting of the data was limited to regions that were free of such artifacts.

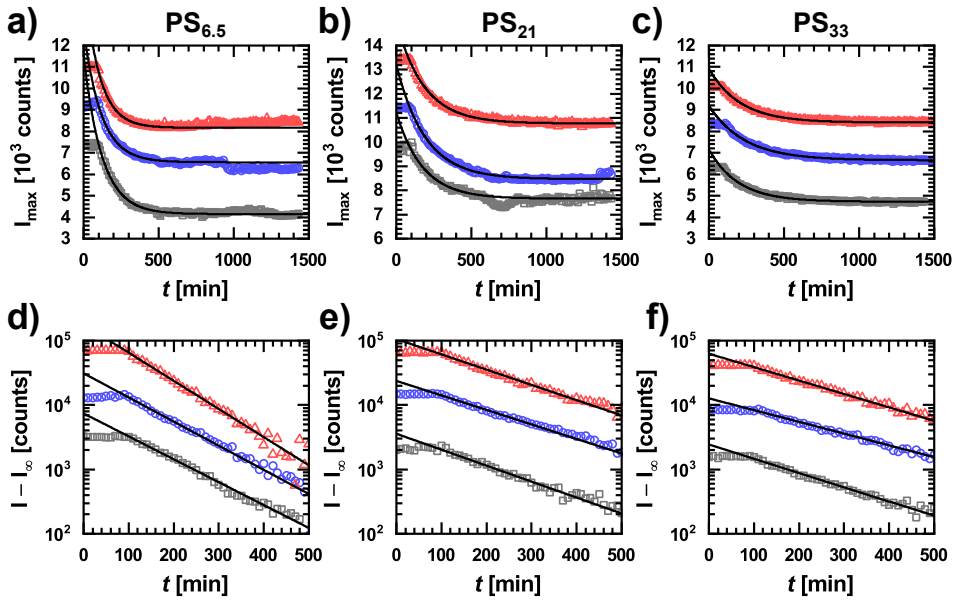

Figure 57: a –c) Fluorescence intensity curves for the ligand binding experiments with $PS_{6.5}$, PS_{21}, and PS_{33} respectively. The curves of individual runs of the triplicate measurements are offset along the intensity axis for better clarity. d – f) Semi-logarithmic plots of the fluorescence intensity during the first 500 minutes of the experiments, corrected for the baseline intensity, I_∞. The curves for each molecular weight are offset for clarity. The black lines in all figures correspond to the single exponential fit to the data. Reproduced from Ref. [147] with permission from the Royal Society of Chemistry.

All curves were fitted with the single-exponential function shown in Equation 100. Here, I_0 is the starting intensity, I_∞ is the plateau intensity at infinite time, k_{eff} is the effective rate constant, and t_0 is the starting time, at which the substrate was immersed in the solution.

$$I(t) = I_\infty + (I_0 - I_\infty)\exp[-k_{\text{eff}}\,(t - t_0)] \tag{100}$$

The fits are shown as black lines in the plots. In general, there is a noticeable dependence of the intensity difference $I_0 - I_\infty$ and the reaction rate on the molecular weight of the ligands. The longer the polymer chain, the slower the binding and the smaller the overall intensity change over time. This already indicates that the number

of chains binding to each AuNP also depends on ligand length, which will be discussed later. Within the first 500 minutes of the experiments, all measured intensity profiles can be described by a single-exponential decay. In the plateau region at longer experiments times, the aforementioned artifacts have a greater impact on the intensity. In order to linearize the data, the intensity is reduced by I_∞. As demonstrated by Equation 101, the data should linearize in a semi-logarithmic representation.

$$\ln[I(t) - I_\infty] = \ln[I_0 - I_\infty] - k_{\text{eff}}\,(t - t_0) \tag{101}$$

The semi-logarithmic plots are shown in **Figure 57 d – f**. Indeed, the curves are linear in the time range from t_0 to $t = 500$ min. Deviations from linearity, observed for the PS_{21} in particular, highlight other influences on fluorescence intensity. However, the single-exponential nature of the intensity profiles is confirmed, indicating a pseudo-first order mechanism. The substantial plateau intensities, I_∞, suggest that the ligand binding either is an equilibrium process or is otherwise limited to low conversions. The values for k_{eff} from curve fitting are summarized in **Table 9**. There is a trend for a decrease of the effective rate constant with increasing molecular weight of the ligand. This implies a significant effect of chain length on the overall reaction kinetics. Individual values for the three runs with each ligand are fairly similar and the standard deviation of the average effective rate constants, $\overline{k}_{\text{eff}}$, is below 10% for all three ligands. In general, the rate constants are very small, corresponding to average reaction half-lives, $\overline{T}_{1/2}$, in the order of several hours. Due to the incomplete ligand binding and high I_∞ values, the half-life is of limited utility and only provides an impression of the time scales of the process.

Table 9: Summary of effective rate constants, k_{eff}, from the single-exponential fits to the fluorescence intensity curves.

Ligand	k_{eff} [10^{-5} s^{-1}]	$\overline{k}_{\text{eff}}$ [10^{-5} s^{-1}]	$\overline{T}_{1/2}$ [s]
$PS_{6.5}$	16.8 ± 0.4 13.7 ± 0.3 14.4 ± 0.3	15 ± 1	4600 ± 300
PS_{21}	9.5 ± 0.5 9.1 ± 0.2 8.7 ± 0.2	9.1 ± 0.4	7600 ± 300
PS_{33}	8.5 ± 0.2 7.0 ± 0.1 8.0 ± 0.1	7.8 ± 0.6	8900 ± 700

Both, the slow reaction rates and apparent chain length dependency, hint towards a diffusion-limited process. As the solution was stirred during the experiment, it is unlikely that this diffusion-limitation is a result of the immobilization of AuNPs on a substrate. In order to test this hypothesis, a Smoluchowski-type approach for diffusion-controlled reactions was used.[149–152] This model separates the reaction into two subsequent elemental steps; diffusion and activation. The general reaction scheme is shown in Equation 102. In the diffusion step, the reactants approach and form a contact pair. This process is reversible with an equilibrium constant of $K = k_{\text{d}}^{+}/k_{\text{d}}^{-}$, the value of which depends on the interaction strength between A and B. Thus, once the contact pair is formed, the reactants can separate again or continue to react in the activation-limited second step with the rate constant k_a.

$$\text{A} + \text{B} \underset{k_{\text{d}}^{-}}{\overset{k_{\text{d}}^{+}}{\rightleftharpoons}} \text{AB} \xrightarrow{k_{\text{a}}} \text{C} \tag{102}$$

Assuming a steady state for the first reaction step, the effective rate constant for the reaction $\text{A} + \text{B} \longrightarrow \text{C}$ can be approximated according to Equation 103.[153–156]

$$k_{\text{eff}} \approx \frac{k_{\text{d}} k_{\text{a}}}{k_{\text{d}} + k_{\text{a}}} \tag{103}$$

The two elemental reaction rates can be separated by inversion of k_{eff}.

$$\frac{1}{k_{\text{eff}}} = \frac{1}{k_{\text{a}}} + \frac{1}{k_{\text{d}}} \tag{104}$$

Whereas k_{eff} is a directly measurable quantity, the values of k_{a} and k_{d} are not easily obtainable. A common approach is the identification of diffusive and activation contributions by their different dependence on experimental parameters, most notably temperature and viscosity of the medium. Since viscosity only affects the diffusion-limited step, measurement of k_{eff} in relation to a change in viscosity can be used to obtain k_{a} from the extrapolation to $\eta = 0$. k_{d} can then be calculated using Equation 104. Moreover, the Smoluchowski model provides a formalism for the calculation of k_{d} based on the geometric and diffusion properties of the reactions. As shown in Equation 105, k_{d} is defined a product of interaction radius, r, and the effective diffusion coefficient, D_{eff}, of the system.[149, 154]

$$k_{\text{d}} = 4\pi r D_{\text{eff}} \tag{105}$$

For simple systems, such as monoatomic reactants, r is the sum of the radii, r_{A} and r_{B}, of the reactants and D_{eff} is the sum of diffusion coefficients of the reactants. Using the Stokes-Einstein relation, Equation 106 is obtained. The significance of the viscosity and relative size of the reactants is clearly visible.

$$k_{\text{d}} \approx \frac{2k_{\text{B}}T}{3\eta} \frac{(r_{\text{A}} + r_{\text{B}})^2}{r_{\text{A}}\, r_{\text{B}}} \tag{106}$$

However, this model does not account of anisotropic reactivity or steric effects. More complex models, in particular for enzyme kinetics, have attempted to adopt the Smoluchowski model by including rotation and reactivity parameters. The system used for the ligand binding experiments allows for another simplification. Due to the fact that one reactant, i.e. the AuNPs, are immobilized, only the diffusion of the polymer chains has to be considered. Rather than varying the viscosity of the medium, the chain length and thus the diffusion coefficient, D_{t}, of the polymer chains is altered. Conveniently, D_{t} can be measured directly by DLS. Although the reaction radius is unknown, it can be assumed constant. Consequently, the k_{d} is likely to be proportional

to D_t. Introducing an unknown reactivity prefactor, β, we obtain Equation 107.

$$k_d = \beta D_t \tag{107}$$

This expression is now inserted into Equation 104.

$$\frac{1}{k_{eff}} = \frac{1}{k_a} + \frac{1}{\beta D_t} \tag{108}$$

Thus, a plot of $1/k_{eff}$ against $1/D_t$ should allow us to separate the diffusive and activation contributions to the effective rate constant. **Figure 58** shows the plot according to Equation 108 for the data from this series of experiments. The data points closely follow the linear fit, indicating the applicability of a modified Smoluchowski model. There is a significant ordinate offset, which corresponds to $1/k_a$, whereas the slope of the fit corresponds to $1/\beta$. The values for slope and offset are $(6.73 \pm 0.01)\ 10^{-7}$ m^2 and $(2.00 \pm 0.02)\ 10^3$ s respectively.

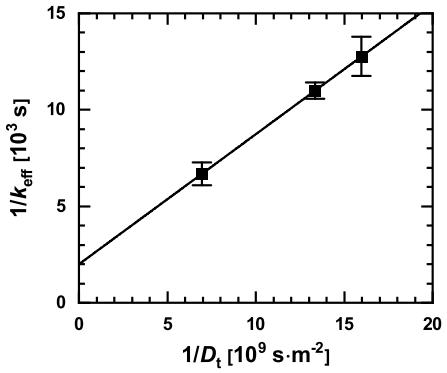

Figure 58: Reciprocal plot of the average effective rate constant, $\overline{k}_{eff}$, in relation to the diffusion coefficient of the polymer ligands. Reproduced from Ref. [147] with permission from the Royal Society of Chemistry.

Using Equation 108, we can now calculate k_a and the individual values for k_d for each molecular weight of ligands. The values are summarized in **Table 10**.

The calculated rate constants support the hypothesis of a diffusion-limited process. All k_d are significantly smaller than k_a and the influence on molecular weight on k_d is apparent. From the range of values one can already deduce that the process remains

Table 10: Summary of calculated rate constant of activation and diffusion-limited steps, k_a and k_d, during the ligand binding experiment.

k_a [10^{-5} s^{-1}]	k_d [10^{-5} s^{-1}]		
	$PS_{6.5}$	PS_{21}	PS_{33}
50.1 ± 0.3	21.3 ± 0.4	11.1 ± 0.2	9.3 ± 0.1

diffusion-limited even for small molecular weights of the ligand. In fact, the theoretical cross-over chain length, at which $k_\mathrm{a} = k_\mathrm{d}$, is approximately 12 monomer units, corresponding to a molecular weight of 1250 g/mol. This represents an interesting result, as this chain length is very similar to the statistical segment length of PS in DMF at experimental conditions. Although this may be coincidental, there are also relevant physical implications. Entanglements are not possible for such short chains even at the high local concentrations near the particle surface. Within a statistical segment the chains assume a stretched, approximately linear conformation. Ligoure and Leibler postulate that the adsorption kinetics of end-on grafted chains are determined by the reptation-like diffusion of chains through the forming brush.[145] Without entanglements, reptation does not take place. Instead, the chains should retain diffusion according to the Rouse model all the way to the particle surface, irrespective of the grafting density of the pre-existing brush. This is reflected in the theoretical model for the repulsive potential created by the brush, which vanishes for brush heights in the order of the segment length.

9.5 Characterization of ligand layers by AFM

The morphology of the samples after the kinetics experiments was investigated by AFM force mapping in dry state. Using this technique rather than the tapping mode shown previously, soft and hard features of the samples can be resolved and distinguished. The height images are shown in **Figure 59**. The panels show images from scans before the experiment (**a**) and after the kinetics experiment with $PS_{6.5}$ (**b**), PS_{21} (**c**), and PS_{33} (**d**), respectively.

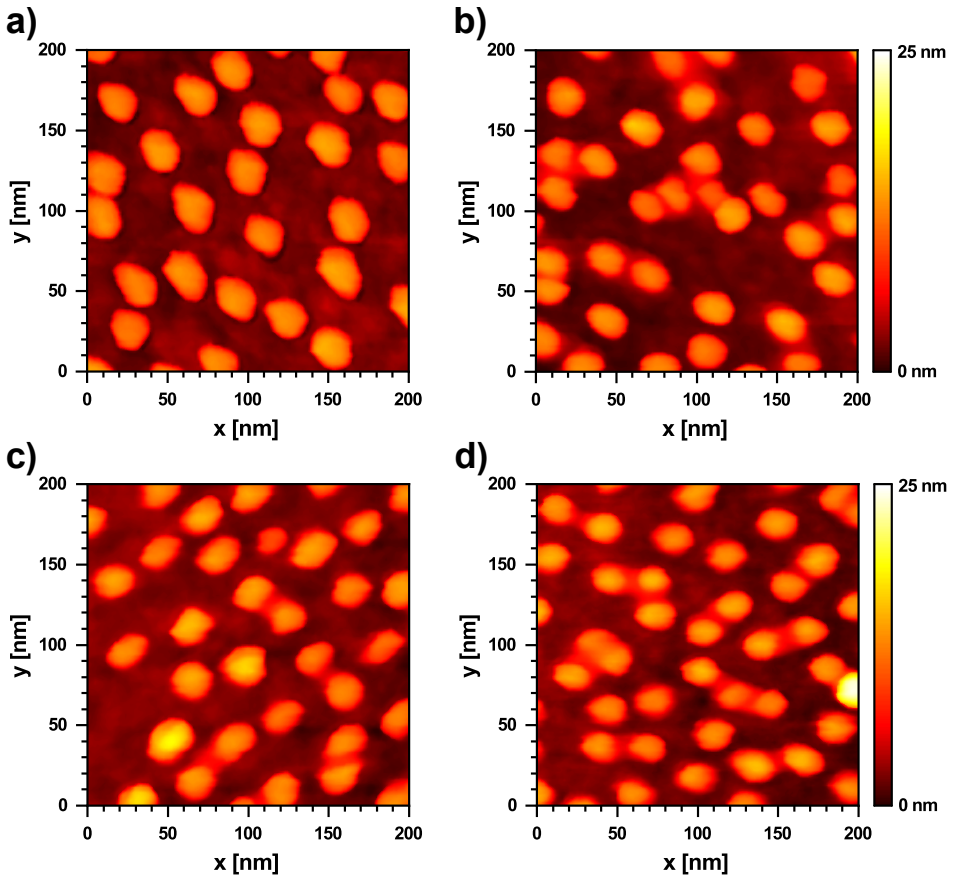

Figure 59: AFM height images of glass substrates with immobilized AuNP. a) Shows a sample before, the other images show samples after the kinetics experiments with b) $PS_{6.5}$, c) PS_{21}, and d) PS_{33}, respectively. Reproduced from Ref. [147] with permission from the Royal Society of Chemistry.

All images show AuNPs on the substrate. The slightly larger and elongated shape of the particles in **a** is an artifact as a result of thermal drift. In contrast to the images for samples after the experiment, i.e., with bound PS ligands, the outlines of the AuNPs are much clearer for the sample before the experiments. The height on the edges of the particle outlines appears to drop off more abruptly. For samples after ligand binding, the particle outlines are much smoother. Additionally, the outlines of particles that are sufficiently close to each other appear to merge, in particular for samples with PS_{21} and PS_{33} ligands. The diameter and height of the particles slightly

exceeds the expected value of approximately 12 nm, which could indicate a layer on top of the particles or merely be a result of tip-sample convolution. Nevertheless, all these observations are a first indication for the presence of polymer around and in between the particles.

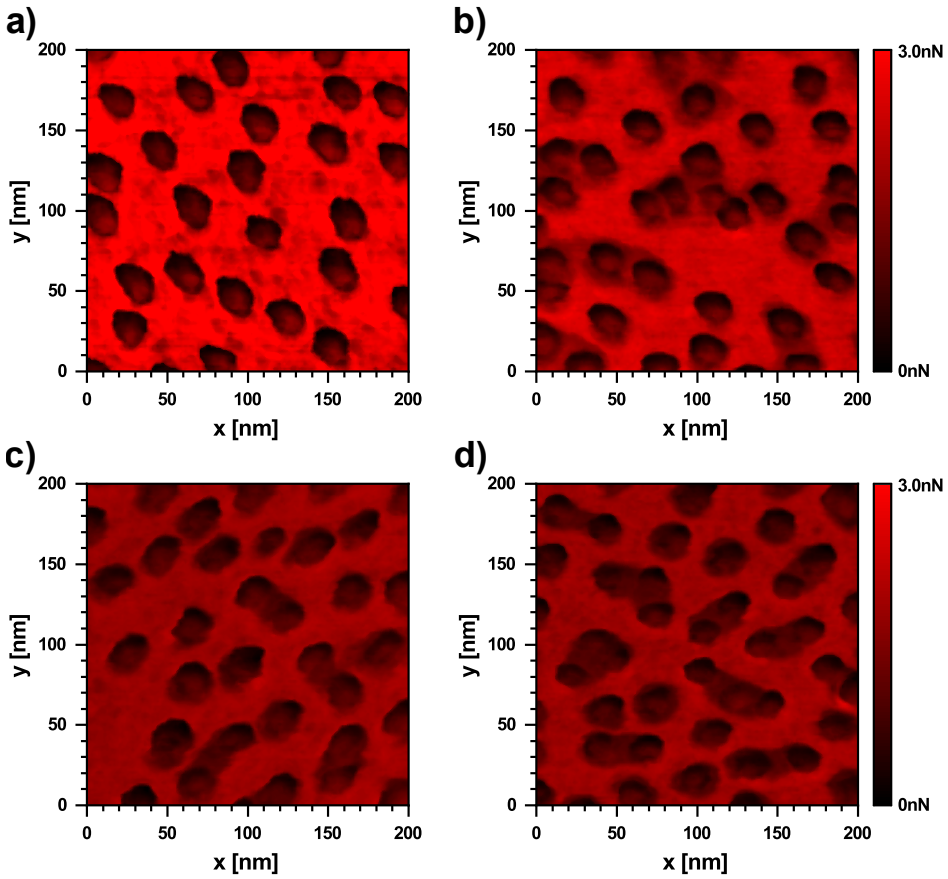

Figure 60: AFM adhesion images of glass substrates with immobilized AuNP. a) Shows a sample before, the other images show samples after the kinetics experiments with b) $PS_{6.5}$, c) PS_{21}, and d) PS_{33}, respectively. Reproduced from Ref. [147] with permission from the Royal Society of Chemistry.

A clearer picture of the particle morphology is obtained from the adhesion force images of the same scans, which are shown in **Figure 60**. As the AFM probe is retracted from the sample, adhesion forces hold the tip of the probe on the sample surface.

Once the adhesion forces are overcome by the straining probe, the tip is released from the surface in a sudden motion. The minimum in the force curve, i.e., the maximum adhesion force, is used as pixel value to construct the image. In the figure, dark and bright red areas correspond to small and large adhesion forces, respectively. In all four images, the substrate exhibits much stronger adhesion than the area on and around the AuNPs. Since adhesion forces are strongly influenced by the geometry of the interface between the probe and the sample at a given point, flat surfaces tend to exhibit stronger adhesion than angled surfaces. This is also demonstrated by the brighter, more adhesive areas on top of the AuNPs as compared to the sloped sides. Similar to the height images, the particle outlines in the adhesion image of the sample before any ligand binding appear to be much clearer and well contrasted against the substrate. Depending on the molecular weight of the ligand used, there is a dark corona around the AuNP outlines for samples after ligand binding. Again, samples with PS_{21} and PS_{33} ligands show merging of the particle outlines, which can now be identified as bridging between AuNPs by substance with slightly different adhesiveness. It is reasonable to assume that this substance is indeed polymer, which is located exclusively around the AuNPs. Although not very pronounced, there appears to be a trend towards less adhesion and more bridging for increasing molecular weight of the ligand. The reduced adhesion on the polymer domains may be a result of the poor interface between probe and polymer and the flexibility of the chains, which can act as a form of lubricant for the motion of the probe. As a result, particles functionalized with the shorter chains exhibit strong adhesion on the AuNP surface and the surrounding corona, whereas the particles carrying longer chain ligands exhibit weaker adhesion, due to screening of the smooth glass and gold surfaces by polymer. To summarize, AFM images of samples before and after the kinetics experiments were able to demonstrate that the PS ligands specifically bind to the AuNP surface, rather than adsorbing non-specifically on the entire surface. Although the thickness of the polymer layer is small, the adhesion contrast allowed a clear distinction of the polymer from the AuNPs and the substrate. An influence of ligand length can be observed, with more pronounced polymer coronas and bridging between neighboring particles for the longer ligands.

10 Conclusion and outlook

Throughout this thesis, various aspects of the formation and properties of AuNP@PS with high polymer grafting densities have been elucidated. In this concluding section, the fundamental findings from the different methods used will be summarized and brought into context. Finally, some remarks on the limitations of the work presented here and suggestions for future investigation will be given.

In order to achieve good statistical precision during the characterization of AuNP@PS, a well-defined system with narrow size and molecular weight distribution of particles and polymers, respectively, was required. Spherical AuNPs were prepared following the inverse Turkevich method. This protocol allowed the large scale synthesis of AuNPs in aqueous medium with an extraordinary degree of control and reproducibility. Across multiple syntheses with batch sizes ranging from 300 mL to 4.5 L, particle diameters between 12 and 13 nm and standard deviations of less than 1 nm within one batch were consistently achieved. The particle size was assessed by TEM and SAXS, with both methods providing identical values for the particle size within one standard deviation. AuNPs prepared by this method exhibit a high degree of sphericity. They are less faceted than particles prepared by the conventional Turkevich method. The LSPR peak was usually located at a wavelength of 515.5 nm in water with only little variation between batches. Notably, this represents a slight blue-shift compared to conventional Turkevich particles of similar size, possibly as a result of low polydispersity and the absence of non-spherical particles.

PS ligands were prepared using RAFT polymerization of styrene in bulk, tuning the molecular weight of the ligands by variation of the monomer/CTA ratio and reaction conversion. The obtained polymers exhibit number average molecular weights from 6.5 to 33 kg/mol with $\overline{M}_\mathrm{w}/\overline{M}_\mathrm{n}$ ratios between 1.1 and 1.2. Synthesis was facilitated by the low reaction rate, which allowed monitoring the conversion via NMR and stopping the reaction at the desired molecular weights. A trithiocarbonate carrying an azide group on the initiating chain end was chosen as CTA. After hydrolysis of the trithiocarbonate group, α,ω-functionalized PS ligands with a thiol on one terminus and the azide on the other were obtained.

The direct phase transfer method, commonly used for the functionalization of AuNPs with small, hydrophobic ligands, has proven to be unreliable when used with longer, end-functionalized polymer chains, such as those used in this work. One reason is the relative inaccessibility of the functional end group within a polymer coil. Moreover, a high polymer concentration usually is required to overcome the high interfacial tension between water and non-polar organic solvents and to stabilize AuNPs during their transition into the organic phase. Substantial energy input (mechanical, thermal) may also be required to force the particles across the interface. The lack of control over the process and the large amounts of polymer required to successfully transfer small volumes of aqueous particle dispersion into the organic phase ultimately motivated the development of a novel, two-step, single phase approach.

In order to enable ligand exchange in a single organic phase under equilibrium conditions, the AuNPs were first functionalized with PVP as an auxiliary ligand. This polymer is readily available, is soluble in water as well as a wide range of organic solvents, and adsorbs to gold surfaces via polydentate coordination of the pyrrolidone groups. AuNP@PVP were transferred to DMF by centrifugation and solvent exchange. The particles were found to be stable in DMF for several months. The ligand exchange with PS ligands was performed in DMF by simply mixing the particles and the ligands. The purification involved selective precipitation of PS functionalized particles and subsequent purification by centrifugation. Although this method is time-consuming, it reliably produced AuNP@PS in quantities of up to 20 mg per batch. The obtained particles demonstrated exceptional stability, as they can be vacuum dried or centrifuged under harsh conditions and be fully redispersed in a wide rang of solvents. Elemental analysis of the dried product showed a low nitrogen content and a H/C ratio close to that of PS, indicating successful displacement of PVP by the thiol terminated ligands.

The optical properties of AuNP@PS in relation to ligand length and solvent were investigated by UV/Vis spectroscopy. In a homogeneous environment the wavelength of the LSPR maximum redshifts approximately linearly with increasing refractive index of the medium. This has been confirmed by experimental data for various AuNP systems in the past. However, a more complex behavior was observed for AuNP@PS

when they were dispersed in different solvents, including MEK, THF, DMF, dioxane, chloroform, and toluene, corresponding to a refractive index range from 1.379 to 1.497. Rather than a monotonous, linear increase with n, a distinct blueshift of the LSPR maximum was observed for the transition from THF to dioxane, to DMF, which occurred for all ligand lengths. This unusual behavior was attributed to a specific influence of the solvents on the structure of the polymer brush, changing the effective refractive index around the gold core beyond the difference in solvent refractive index. It was found that the influence of different brush swelling could be mitigated by a reciprocal plot. This plot confirmed the validity of the linear approximation under the assumption that the volume fraction of polymer and solvent are invariable and supported the initial hypothesis of a change of these volume fractions in the case of AuNP@PS. The lack of reports on similar behavior in the literature can be related to the large effective volume fraction of PS in the studied system. Using parameters from the reciprocal plot, the ideal, linear behavior for a fixed polymer volume fraction was constructed. The effect of brush swelling could be isolated from the refractive index change of the solvent. A comparison of the deviation of experimental values from the fit with theoretical values for the excluded volume of PS in the corresponding solvent suggests that larger excluded volume and thus stronger swelling decrease the volume fraction of polymer and cause the blueshift through a reduction of the effective refractive index. The UV/Vis spectra also confirmed the stability of AuNP@PS, as there was no evidence for aggregation in most solvents and for most ligand lengths. Only particles with $PS_{6.5}$ ligand could not be stabilized in all solvents. AuNP@PS dispersed in very non-polar solvents were observed to aggregate over time, possibly due to residual water promoting hydrophobic interactions.

The structure of the ligands shell in DMF was investigated using a combination of DLS and AUC. In general, the hydrodynamic radius of AuNP@PS increased with increasing molecular weight of the PS chains, indicating an increase in brush height. As the influence of molecular weight was not as pronounced as the range of molecular weights would suggest, the grafting density seemed to vary significantly in relation to ligand molecular weight. This was confirmed by sedimentation velocity experiments, which provided values for the average particle density. Calculations based on DLS and AUC

data allowed a good estimation of grafting densities, which ranged from 0.75 to 2 nm^{-2} and appeared to follow a power law regarding $\overline{M}_n$. These values are within the range of grafting densities reported for polymeric ligands of similar molecular weight and on particles with similar dimensions as those used in this work. Overall, the grafting densities obtained from the combination of DLS and AUC are 2-4 times larger than those estimated from elemental analysis of an earlier batch of particles. The main difference in terms of preparation is the much longer reaction time for the particles characterized by DLS and AUC of 10 days instead of 3 days for particles characterized by elemental analysis. This is in agreement with kinetic experiments, which suggest fairly slow adsorption of PS ligands. The intrinsic limitations of the experimental methods should also be highlighted. Elemental analysis directly measures the mass of C, H, N, and S in the sample. Although the brush mostly consists of these elements, the residual mass of gold can only be extrapolated. On the other hand, interpretation of AUC data strongly depends on the choice of model and input parameters. As most of the relevant parameters were known and the fit curves generally described the evolution of the sedimentation front, the calculated grafting densities should be reasonably accurate. One shortcoming of the combination of DLS and AUC is the restriction to hydrodynamic dimensions. Since R_h of a polymer chain in solution is many times smaller than its physical size, AuNP@PS can be expected to exhibit a similar behavior, in particular for the relatively loose outer regions of the brush structure. In terms of methodology, we can conclude that TGA remains the gold standard for the determination of absolute grafting densities. Alternative methods, such as AUC or elemental analysis, should be calibrated against TGA, whenever possible.

The scaling of brush height in relation to chain length and grafting density was analyzed. As DLS and AUC measurements were performed close to θ conditions, the brush height should scale as $H \propto N^{1/2}\sigma^{1/4}$ for a semi-dilute brush and $H \propto N\sigma^{1/2}$ for a concentrated brush. The CPB scaling relation accurately described AuNP@PS with ligand molecular weights between 21 and 33 kg/mol, while slight aggregation of particles with shorter ligands rendered those data points unreliable. Using two different approaches, the consistency of CPB scaling with experimental data was tested. Firstly, the volume fraction profiles of the polymer brush were modeled, based on an

analytical approximation of SCFT results. The integrated monomer number density was in good agreement with the experimentally determined segment number in the brush, confirming that the theoretical volume fraction profiles can plausibly describe the brush structure. Secondly, the experimental data was used to approximate the free energy of chain stretching in relation to brush height. The minima of these free energy profiles correspond to the most likely brush height. These calculations precisely reproduced the experimental $H \propto N\sigma^{1/2}$ scaling, while systematically over-estimating the brush height by approximately 50%. Interestingly, this factor is similar to the $R_\mathrm{g}/R_\mathrm{h}$ ratio of polymers in θ conditions and points towards the potential discrepancy between hydrodynamic and physical dimensions of AuNP@PS. In addition, both approaches for the verification of CPB scaling strongly depend on the definition of the polymer volume fraction ϕ_0 at the particle surface. The commonly found expression $\phi_0 = \sigma^{1/2}b$ was used in this work, which yielded fairly high and, in some cases, unphysical values for ϕ_0.

SAXS measurements in DMF and 1,4-dioxane enabled further insight into the structure and properties of the polymer brushes. Due to the low contrast between scattering length densities of the solvents and PS compared to the very high scattering length density of gold, the polymer brush has a negligible contribution to the scattering intensity. However, the structure factor, caused by interaction of particles, was found to contain the signature of the polymer brush. The structure factor contribution was much less pronounced in DMF than in dioxane, which may be related to solvent quality or polarity. A square well potential model was used to describe the structure factor. The fits were in excellent agreement with experimental data. The well depth and width increased with $\overline{M}_\mathrm{n}$ of the ligand. The onset of the repulsive interaction also shifted towards larger distances. In conjunction with data from DLS and AUC, we can deduce that the range and strength of interactions strongly correlates with ligand length. Weaker interactions are observed for a thinner but denser brush, whereas a thicker, looser brush results in stronger attractive particle interactions. The nature of these interactions is difficult to discern. However, as they are stronger in non-polar dioxane than in very polar DMF, hydrophobic interactions due to residual water or dipole interactions of the azide groups at the free chain ends should be considered. Notably,

the range of attractive interactions exceeds the R_h of the particles in most cases, which is another indication for the underestimation of particle and brush dimensions by DLS. Further evidence of brush structure and particle interactions was found in TEM images of AuNP@PS. Although the poor contrast of PS rendered the brush barely visible compared to the gold cores, the large inter-particle distances indirectly demonstrated the presence of the brush and its overall repulsive potential. The core-core separation roughly matches the extent of polymer brush. Correlation of the particle separation with the R_h obtained from DLS measurements revealed two distinctive length scales of aggregation. The first length scale corresponds to shell-shell contact, i.e. a particle separation of $d = 2R_h$. The second length scale is on the order of $d = R_h$ and is also similar to the hard sphere contact length determined by SAXS measurements. Therefore, the repulsive potential effectively prevents particles from approaching further, even upon drying. This also suggests that the hard sphere contact length is governed by the high polymer concentration in the inner brush and the inability of the chains in this region to be compressed much further. A comparison between the different samples with varying $\overline{M}_n$ of the ligands indicates that AuNP@PS functionalized with shorter polymer chains are more likely to approach to this hard sphere barrier, whereas particles with longer chains tend to remain at shell-shell contact upon drying. This is in agreement with DLS and AUC data, which showed a higher tendency of particles with short ligands to aggregate in dispersion.

The striking correlation between chain length of the ligand and grafting density motivated the kinetic investigation of the brush formation mechanism. For this purpose, the adsorption of fluorescently labeled PS ligands with different molecular weights onto immobilized AuNP was followed by fluorescence spectroscopy. The initial concentration of PS ligand and the available particle surface were kept constant. There was a distinctive change in binding kinetics between the different ligands. With shorter polymer chains, the adsorption process was faster and more chains were adsorbed in total. However, a large portion of polymer remained in solution for all chain lengths, thus an equilibrium was reached before quantitative adsorption could occur. The overall long times required to reach equilibrium indicate significant hindrance of the adsorption process. Using a Smoluchowski-type model for diffusion limited reaction kinetics, the

rate constants of diffusion and activation could be separated. This revealed a common rate constant of activation for all three tested ligands, whereas the diffusion rate constant increased with decreasing chain length. A major role of chain entanglements on the kinetics was deduced from the transition point between diffusion and activation dominated behavior, which also is in excellent agreement with theoretical models. Despite differences between reaction conditions of the kinetic investigation and the ligand exchange protocol in bulk, developed for this work, the mechanistic model may be applied to both. It provides an explanation for the observed decrease in grafting density with increasing chain length. The adsorption of long polymer chains is more limited by kinetic hindrance generated by the forming brush itself.

To conclude, this work presented a robust method for the preparation of AuNPs functionalized with PS ligands for use in organic media. The properties of the particles as well as the structure and formation mechanism of the polymer were investigated by various methods, including imaging, scattering, and spectroscopy. The molecular weight of the polymeric ligands was found to have a large effect on dimensions, stability, and optical properties of the investigated AuNP@PS. Due to a high grafting density of polymer chains on the particle surface, the brush structure is dominated by polymer-polymer interactions. These interactions also play a role in particle stability, as the dense inner brush creates a repulsive pair potential, whereas the lower volume fraction in the outer brush promotes attractive interactions between particles. The formation of the brush was found to be limited by the diffusion of polymer chains to the particle surface. This diffusion is hindered as more and more chains adsorb, which causes the ligand binding process to be self-limiting. Since the molecular weight of the ligands also affects their diffusion characteristics, the grafting density and brush height achievable through this process are determined by the chain length of the ligands.

This work only touched on a small parameter set for both synthesis and characterization of polymer functionalized particles. Most experiments were limited to one size and morphology of AuNP, a maximum of six different molecular weights of PS ligand, and only a few solvents, most notably DMF and dioxane at room temperature. The influence of preparation conditions, e.g. the concentrations and ratios of particles and ligands, was investigated only as such was necessary to reproducibly obtain stable

particles. Experimental results from DLS, SAXS, and UV/Vis spectroscopy suggest a significant influence of solvent quality on brush structure and particle stability. A more detailed investigation of the effect of solvent and temperature on the properties of AuNP@PS could help to understand to what extend structural and energetic parameters contribute to particle stability. For instance, the presented data suggests that particle aggregation is dominated by polymer-polymer interactions, which vary with solvent quality and polarity. A comparison of particle interactions and stability in various solvents at their respective θ temperature with PS may reveal such effects. Similarly, the use of other polymers as ligand material may lead to interesting variations on the observed behavior. Furthermore, the grafting density could be altered to examine the transition between semi-dilute and concentrated brush regimes, in particular with short chain ligands or on larger AuNPs to allow simplification to a locally flat brush. Future investigations of the ligand binding kinetics should also include a variation of temperature and solvent viscosity. The influence of diffusion in bulk as compared to diffusion through the forming brush as well as the activation energies may thus be elucidated.

References

[1] Freestone, I.; Meeks, N.; Sax, M.; Higgitt, C. The Lycurgus Cup — A Roman Nanotechnology. *Gold Bull.*, **2007**, *40* (4), 270–277. doi: 10.1007/BF03215599.

[2] Wagner, F. E.; Haslbeck, S.; Stievano, L.; Calogero, S.; Pankhurst, Q. A.; Martinek, K. P. Before Striking Gold in Gold-Ruby Glass. *Nature*, **2000**, *407* (6805), 691–692. doi: 10.1038/35037661.

[3] Molina, G.; Murcia, S.; Molera, J.; Roldan, C.; Crespo, D.; Pradell, T. Color and Dichroism of Silver-Stained Glasses. *J. Nanoparticle Res.*, **2013**, *15* (9), 1932. doi: 10.1007/s11051-013-1932-7.

[4] Liz-Marzán, L. M. *Colloidal Synthesis of Plasmonic Nanometals*. Jenny Stanford Publishing, New York, 1st edition, 2020. ISBN: 9780429295188. doi: 10.1201/9780429295188.

[5] Spinelli, P.; Ferry, V. E.; van de Groep, J.; van Lare, M.; Verschuuren, M. A.; Schropp, R. E. I.; Atwater, H. A.; Polman, A. Plasmonic Light Trapping in Thin-Film Si Solar Cells. *J. Opt.*, **2012**, *14* (2), 024002. doi: 10.1088/2040-8978/14/2/024002.

[6] Mandal, P.; Sharma, S. Progress in Plasmonic Solar Cell Efficiency Improvement: A Status Review. *Renew. Sustain. Energy Rev.*, **2016**, *65*, 537–552. doi: 10.1016/j.rser.2016.07.031.

[7] Hsu, S.-W.; Rodarte, A. L.; Som, M.; Arya, G.; Tao, A. R. Colloidal Plasmonic Nanocomposites: From Fabrication to Optical Function. *Chem. Rev.*, **2018**, *118* (6), 3100–3120. doi: 10.1021/acs.chemrev.7b00364.

[8] Oulton, R. F. Surface Plasmon Lasers: Sources of Nanoscopic Light. *Mater. Today*, **2012**, *15* (1), 26–34. doi: 10.1016/S1369-7021(12)70018-4.

[9] Kravets, V. G.; Kabashin, A. V.; Barnes, W. L.; Grigorenko, A. N. Plasmonic Surface Lattice Resonances: A Review of Properties and Applications. *Chem. Rev.*, **2018**, *118* (12), 5912–5951. doi: 10.1021/acs.chemrev.8b00243.

[10] Azzam, S. I.; Kildishev, A. V.; Ma, R.-M.; Ning, C.-Z.; Oulton, R.; Shalaev, V. M.; Stockman, M. I.; Xu, J.-L.; Zhang, X. Ten Years of Spasers and Plasmonic Nanolasers. *Light. Sci. Appl.*, **2020**, *9* (1), 90. doi: 10.1038/s41377-020-0319-7.

[11] Stiles, P. L.; Dieringer, J. A.; Shah, N. C.; van Duyne, R. P. Surface-Enhanced Raman Spectroscopy. *Annu. Rev. Anal. Chem.*, **2008**, *1* (1), 601–626. doi: 10.1146/annurev.anchem.1.031207.112814.

[12] Stewart, M. E.; Anderton, C. R.; Thompson, L. B.; Maria, J.; Gray, S. K.; Rogers, J. A.; Nuzzo, R. G. Nanostructured Plasmonic Sensors. *Chem. Rev.*, **2008**, *108* (2), 494–521. doi: 10.1021/cr068126n.

[13] Cialla, D.; März, A.; Böhme, R.; Theil, F.; Weber, K.; Schmitt, M.; Popp, J. Surface-Enhanced Raman Spectroscopy (SERS): Progress and Trends. *Anal. Bioanal. Chem.*, **2012**, *403* (1), 27–54. doi: 10.1007/s00216-011-5631-x.

[14] Taylor, A. B.; Zijlstra, P. Single-Molecule Plasmon Sensing: Current Status and Future Prospects. *ACS Sens.*, **2017**, *2* (8), 1103–1122. doi: 10.1021/acssensors.7b00382.

[15] Gormley, A. J.; Larson, N.; Sadekar, S.; Robinson, R.; Ray, A.; Ghandehari, H. Guided Delivery of Polymer Therapeutics Using Plasmonic Photothermal Therapy. *Nano Today*, **2012**, *7* (3), 158–167. doi: 10.1016/j.nantod.2012.04.002.

[16] Mackey, M. A.; Ali, M. R. K.; Austin, L. A.; Near, R. D.; El-Sayed, M. A. The Most Effective Gold Nanorod Size for Plasmonic Photothermal Therapy: Theory and In Vitro Experiments. *J. Phys. Chem. B*, **2014**, *118* (5), 1319–1326. doi: 10.1021/jp409298f.

[17] Masson, J.-F. Surface Plasmon Resonance Clinical Biosensors for Medical Diagnostics. *ACS Sens.*, **2017**, *2* (1), 16–30. doi: 10.1021/acssensors.6b00763.

[18] Mirvakili, S. M.; Langer, R. Wireless On-Demand Drug Delivery. *Nat. Electron.*, **2021**, *4* (7), 464–477. doi: 10.1038/s41928-021-00614-9.

[19] Vert, M.; Doi, Y.; Hellwich, K.-H.; Hess, M.; Hodge, P.; Kubisa, P.; Rinaudo, M.; Schué, F. Terminology for Biorelated Polymers and Applications (IUPAC Recommendations 2012). *Pure Appl. Chem.*, **2012**, *84* (2), 377–410. doi: 10.1351/PAC-REC-10-12-04.

[20] Everett, D. H. Manual of Symbols and Terminology for Physicochemical Quantities and Units, Appendix II: Definitions, Terminology and Symbols in Colloid and Surface Chemistry. *Pure Appl. Chem.*, **1972**, *31* (4), 577–638. doi: 10.1351/pac197231040577.

[21] Masters, B. R. *Superresolution Optical Microscopy: The Quest for Enhanced Resolution and Contrast*. Springer International Publishing, Cham, 2020. ISBN: 978-3-030-21691-7. doi: 10.1007/978-3-030-21691-7.

[22] Turkevich, J.; Hillier, J. Electron Microscopy of Colloidal Systems. *Anal. Chem.*, **1949**, *21* (4), 475–485. doi: 10.1021/ac60028a009.

[23] Butt, H. J.; Berger, R.; Bonaccurso, E.; Chen, Y.; Wang, J. Impact of Atomic Force Microscopy on Interface and Colloid Science. *Adv. Colloid Interface Sci.*, **2007**, *133* (2), 91–104. doi: 10.1016/j.cis.2007.06.001.

[24] Ducker, W. A.; Senden, T. J.; Pashley, R. M. Direct Measurement of Colloidal Forces Using an Atomic Force Microscope. *Nature*, **1991**, *353* (6341), 239–241. doi: 10.1038/353239a0.

[25] Glatter, O. *Scattering Methods and Their Application in Colloid and Interface Science*. Elsevier, 2018. ISBN: 978-0-12-813580-8. doi: 10.1016/B978-0-12-813580-8.00016-X.

[26] Li, T.; Senesi, A. J.; Lee, B. Small Angle X-Ray Scattering for Nanoparticle Research. *Chem. Rev.*, **2016**, *116* (18), 11128–11180. doi: 10.1021/acs.chemrev.5b00690.

[27] Degiorgio, V.; Piazza, R. Light Scattering in Colloid and Interface Science. *Curr. Opin. Colloid Interface Sci.*, **1996**, *1* (1), 11–16. doi: 10.1016/S1359-0294(96)80038-0.

[28] Schärtl, W. *Light Scattering from Polymer Solutions and Nanoparticle Dispersions*. Springer, Berlin, Heidelberg, 2007. ISBN: 978-3-540-71951-9. doi: 10.1007/978-3-540-71951-9.

[29] Teixeira, J. Introduction to Small Angle Neutron Scattering Applied to Colloidal Science. In Chen, S.-H.; Huang, J. S.; Tartaglia, P., editors, *Structure and Dynamics of Strongly Interacting Colloids and Supramolecular Aggregates in Solution*, pages 635–658. Springer Netherlands. ISBN: 978-94-011-2540-6. doi: 10.1007/978-94-011-2540-6_32.

[30] Ballauff, M. SAXS and SANS Studies of Polymer Colloids. *Curr. Opin. Colloid Interface Sci.*, **2001**, *6* (2), 132–139. doi: 10.1016/S1359-0294(01)00072-3.

[31] Feigin, L. A.; Svergun, D. I.; Taylor, G. W. *Structure Analysis by Small-Angle X-Ray and Neutron Scattering*. Springer US, Boston, MA, 1987. ISBN: 978-1-4757-6624-0. doi: 10.1007/978-1-4757-6624-0.

[32] Thomas, J. M. The Birth of X-Ray Crystallography. *Nature*, **2012**, *491* (7423), 186–187. doi: 10.1038/491186a.

[33] Borisov, S. V.; Podberezskaya, N. V. X-Ray Diffraction Analysis: A Brief History and Achievements of the First Century. *J. Struct. Chem.*, **2012**, *53* (1), 1–3. doi: 10.1134/S0022476612070013.

[34] Kreibig, U.; Vollmer, M. *Optical Properties of Metal Clusters*. Springer, Berlin, Heidelberg, 1995. ISBN: 978-3-662-09109-8. doi: 10.1007/978-3-662-09109-8.

[35] Pomogailo, A. D.; Kestelman, V. N. *Metallopolymer Nanocomposites*. Springer, Berlin, Heidelberg, 2005. ISBN: 978-3-540-26523-8. doi: 10.1007/b137740.

[36] Butt, H.; Graf, K.; Kappl, M. *Physics and Chemistry of Interfaces*. Wiley-VCH, Weinheim, 2003. ISBN: 9783527404131. doi: 10.1002/3527602313.

[37] Alemán, J. V.; Chadwick, A. V.; He, J.; Hess, M.; Horie, K.; Jones, R. G.; Kratochvíl, P.; Meisel, I.; Mita, I.; Moad, G.; Penczek, S.; Stepto, R. F. T. Definitions of Terms Relating to the Structure and Processing of Sols, Gels, Networks,

and Inorganic-Organic Hybrid Materials (IUPAC Recommendations 2007). *Pure Appl. Chem.*, **2007**, *79* (10), 1801–1829. doi: doi:10.1351/pac200779101801.

[38] Jiang, F.; Muscat, A. J. Ligand-Controlled Growth of ZnSe Quantum Dots in Water During Ostwald Ripening. *Langmuir*, **2012**, *28* (36), 12931–12940. doi: 10.1021/la301186n.

[39] Clark, M. D. Growth Laws for Surfactant-Coated Nanocrystals: Ostwald Ripening and Size Focusing. *J. Nanoparticle Res.*, **2014**, *16* (2), 2264. doi: 10.1007/s11051-014-2264-y.

[40] Vigderman, L.; Zubarev, E. R. High-Yield Synthesis of Gold Nanorods with Longitudinal SPR Peak Greater than 1200 nm Using Hydroquinone as a Reducing Agent. *Chem. Mater.*, **2013**, *25* (8), 1450–1457. doi: 10.1021/cm303661d.

[41] Wu, S.-H.; Chen, D.-H. Synthesis of High-Concentration Cu Nanoparticles in Aqueous CTAB Solutions. *J. Colloid Interface Sci.*, **2004**, *273* (1), 165–169. doi: 10.1016/j.jcis.2004.01.071.

[42] Wu, H.-L.; Kuo, C.-H.; Huang, M. H. Seed-Mediated Synthesis of Gold Nanocrystals with Systematic Shape Evolution from Cubic to Trisoctahedral and Rhombic Dodecahedral Structures. *Langmuir*, **2010**, *26* (14), 12307–12313. doi: 10.1021/la1015065.

[43] De La Encarnacion Bermudez, C.; Haddadi, E.; Rampazzo, E.; Petrizza, L.; Prodi, L.; Genovese, D. Core–Shell Pluronic-Organosilica Nanoparticles with Controlled Polarity and Oxygen Permeability. *Langmuir*, **2021**, *37* (16), 4802–4809. doi: 10.1021/acs.langmuir.0c03531.

[44] Sokolsky-Papkov, M.; Kabanov, A. Synthesis of Well-Defined Gold Nanoparticles Using Pluronic: The Role of Radicals and Surfactants in Nanoparticles Formation. *Polymers*, **2019**, *11* (10), 1553.

[45] Johnson, S. R.; Evans, S. D.; Brydson, R. Influence of a Terminal Functionality on the Physical Properties of Surfactant-Stabilized Gold Nanoparticles. *Langmuir*, **1998**, *14* (23), 6639–6647. doi: 10.1021/la9711342.

[46] Strong, L.; Whitesides, G. M. Structures of Self-Assembled Monolayer Films of Organosulfur Compounds Adsorbed on Gold Single Crystals: Electron Diffraction Studies. *Langmuir*, **1988**, *4* (3), 546–558. doi: 10.1021/la00081a009.

[47] Karg, M.; Schelero, N.; Oppel, C.; Gradzielski, M.; Hellweg, T.; von Klitzing, R. Versatile Phase Transfer of Gold Nanoparticles from Aqueous Media to Different Organic Media. *Chem. Eur. J.*, **2011**, *17* (16), 4648–4654. doi: 10.1002/chem.201003340.

[48] Wuelfing, W. P.; Gross, S. M.; Miles, D. T.; Murray, R. W. Nanometer Gold Clusters Protected by Surface-Bound Monolayers of Thiolated Poly(ethylene glycol) Polymer Electrolyte. *J. Am. Chem. Soc.*, **1998**, *120* (48), 12696–12697. doi: 10.1021/ja983183m.

[49] Ehlert, S.; Taheri, S. M.; Pirner, D.; Drechsler, M.; Schmidt, H.-W.; Förster, S. Polymer Ligand Exchange to Control Stabilization and Compatibilization of Nanocrystals. *ACS Nano*, **2014**, *8* (6), 6114–6122. doi: 10.1021/nn5014512.

[50] Corbierre, M. K.; Cameron, N. S.; Lennox, R. B. Polymer-Stabilized Gold Nanoparticles with High Grafting Densities. *Langmuir*, **2004**, *20* (7), 2867–2873. doi: 10.1021/la0355702.

[51] Prencipe, G.; Tabakman, S. M.; Welsher, K.; Liu, Z.; Goodwin, A. P.; Zhang, L.; Henry, J.; Dai, H. PEG Branched Polymer for Functionalization of Nanomaterials with Ultralong Blood Circulation. *J. Am. Chem. Soc.*, **2009**, *131* (13), 4783–4787. doi: 10.1021/ja809086q.

[52] Rahme, K.; Chen, L.; Hobbs, R. G.; Morris, M. A.; O'Driscoll, C.; Holmes, J. D. PEGylated Gold Nanoparticles: Polymer Quantification as a Function of PEG Lengths and Nanoparticle Dimensions. *RSC Adv.*, **2013**, *3* (17), 6085–6094. doi: 10.1039/C3RA22739A.

[53] Niemeyer, C. M.; Ceyhan, B. DNA-Directed Functionalization of Colloidal Gold with Proteins. *Angew. Chem. Intl. Ed.*, **2001**, *40* (19), 3685–3688. doi: 10.1002/1521-3773(20011001)40:19⟨3685::AID-ANIE3685⟩3.0.CO;2-E.

[54] Abad, J. M.; Mertens, S. F. L.; Pita, M.; Fernández, V. M.; Schiffrin, D. J. Functionalization of Thioctic Acid-Capped Gold Nanoparticles for Specific Immobilization of Histidine-Tagged Proteins. *J. Am. Chem. Soc.*, **2005**, *127* (15), 5689–5694. doi: 10.1021/ja042717i.

[55] Jenkins, A. D.; Kratochvíl, P.; Stepto, R. F. T.; Suter, U. W. Glossary of Basic Terms in Polymer Science (IUPAC Recommendations 1996). *Pure Appl. Chem.*, **1996**, *68* (12), 2287–2311. doi: doi:10.1351/pac199668122287.

[56] Flory, P. J. *Principles of Polymer Chemistry.* Cornell University Press, Ithaca, NY, 1953. ISBN: 978-0-8014-0134-3.

[57] Michael Rubinstein, R. H. C. *Polymer Physics.* Oxford University Press, Oxford, 2003. ISBN: 978-0-19-852059-7.

[58] Turkevich, J.; Stevenson, P. C.; Hillier, J. A Study of the Nucleation and Growth Processes in the Synthesis of Colloidal Gold. *Discuss. Faraday Soc.*, **1951**, *11* (0), 55–75. doi: 10.1039/DF9511100055.

[59] Polte, J.; Ahner, T. T.; Delissen, F.; Sokolov, S.; Emmerling, F.; Thünemann, A. F.; Kraehnert, R. Mechanism of Gold Nanoparticle Formation in the Classical Citrate Synthesis Method Derived from Coupled In Situ XANES and SAXS Evaluation. *J. Am. Chem. Soc.*, **2010**, *132* (4), 1296–1301. doi: 10.1021/ja906506j.

[60] Wuithschick, M.; Birnbaum, A.; Witte, S.; Sztucki, M.; Vainio, U.; Pinna, N.; Rademann, K.; Emmerling, F.; Kraehnert, R.; Polte, J. Turkevich in New Robes: Key Questions Answered for the Most Common Gold Nanoparticle Synthesis. *ACS Nano*, **2015**, *9* (7), 7052–7071. doi: 10.1021/acsnano.5b01579.

[61] Brust, M.; Walker, M.; Bethell, D.; Schiffrin, D. J.; Whyman, R. Synthesis of Thiol-Derivatised Gold Nanoparticles in a Two-Phase Liquid–Liquid System. *Chem. Commun.*, **1994**, (7), 801–802. doi: 10.1039/C39940000801.

[62] Jana, N. R.; Peng, X. Single-Phase and Gram-Scale Routes Toward Nearly

Monodisperse Au and Other Noble Metal Nanocrystals. *J. Am. Chem. Soc.*, **2003**, *125* (47), 14280–14281. doi: 10.1021/ja038219b.

[63] Rowe, M. P.; Plass, K. E.; Kim, K.; Kurdak, C.; Zellers, E. T.; Matzger, A. J. Single-Phase Synthesis of Functionalized Gold Nanoparticles. *Chem. Mater.*, **2004**, *16* (18), 3513–3517. doi: 10.1021/cm035049t.

[64] Mayya, K. S.; Caruso, F. Phase Transfer of Surface-Modified Gold Nanoparticles by Hydrophobization with Alkylamines. *Langmuir*, **2003**, *19* (17), 6987–6993. doi: 10.1021/la034018+.

[65] Lista, M.; Liu, D. Z.; Mulvaney, P. Phase Transfer of Noble Metal Nanoparticles to Organic Solvents. *Langmuir*, **2014**, *30* (8), 1932–1938. doi: 10.1021/la404569h.

[66] Sánchez-Iglesias, A.; Grzelczak, M.; Altantzis, T.; Goris, B.; Pérez-Juste, J.; Bals, S.; van Tendeloo, G.; Donaldson, J., Stephen H.; Chmelka, B. F.; Israelachvili, J. N.; Liz-Marzán, L. M. Hydrophobic Interactions Modulate Self-Assembly of Nanoparticles. *ACS Nano*, **2012**, *6* (12), 11059–11065. doi: 10.1021/nn3047605.

[67] Grzelczak, M.; Sánchez-Iglesias, A.; Liz-Marzán, L. M. A General Approach Toward Polymer-Coated Plasmonic Nanostructures. *CrystEngComm*, **2014**, *16* (40), 9425–9429. doi: 10.1039/C4CE00724G.

[68] Yockell-Lelièvre, H.; Desbiens, J.; Ritcey, A. M. Two-Dimensional Self-Organization of Polystyrene-Capped Gold Nanoparticles. *Langmuir*, **2007**, *23* (5), 2843–2850. doi: 10.1021/la062886b.

[69] Goulet, P. J. G.; Bourret, G. R.; Lennox, R. B. Facile Phase Transfer of Large, Water-Soluble Metal Nanoparticles to Nonpolar Solvents. *Langmuir*, **2012**, *28* (5), 2909–2913. doi: 10.1021/la2038894.

[70] Choueiri, R. M.; Galati, E.; Thérien-Aubin, H.; Klinkova, A.; Larin, E. M.; Querejeta-Fernández, A.; Han, L.; Xin, H. L.; Gang, O.; Zhulina, E. B.; Ru-

binstein, M.; Kumacheva, E. Surface Patterning of Nanoparticles with Polymer Patches. *Nature*, **2016**, *538* (7623), 79–83. doi: 10.1038/nature19089.

[71] Ullrich, S.; Scheeler, S. P.; Pacholski, C.; Spatz, J. P.; Kudera, S. Formation of Large 2D Arrays of Shape-Controlled Colloidal Nanoparticles at Variable Interparticle Distances. *Part. Part. Syst. Charact.*, **2013**, *30* (1), 102–108. doi: 10.1002/ppsc.201200065.

[72] Alkilany, A. M.; Caravana, A. C.; Hamaly, M. A.; Lerner, K. T.; Thompson, L. B. Phase Transfer of Citrate Stabilized Gold Nanoparticles Using Nonspecifically Adsorbed Polymers. *J. Colloid Interface Sci.*, **2016**, *461*, 39–44. doi: 10.1016/j.jcis.2015.09.010.

[73] Eichinger, B. E.; Flory, P. J. Thermodynamics of Polymer Solutions. Part 1.—Natural Rubber and Benzene. *J. Chem. Soc. Faraday Trans.*, **1968**, *64* (0), 2035–2052. doi: 10.1039/TF9686402035.

[74] Müller, E. A.; Rasmussen, P. Densities and Excess Volumes in Aqueous Poly(ethylene glycol) Solutions. *J. Chem. Eng. Data*, **1991**, *36* (2), 214–217. doi: 10.1021/je00002a019.

[75] Siddiqui, S. A.; Needles, H. L. Solubility Parameters. *Text. Res. J.*, **1982**, *52* (9), 570–579. doi: 10.1177/004051758205200904.

[76] Hansen, C. M. The Universality of the Solubility Parameter. *Product R&D*, **1969**, *8* (1), 2–11. doi: 10.1021/i360029a002.

[77] Teraoka, I. *Polymer Solutions: An Introduction to Physical Properties.* John Wiley & Sons Inc., New York, 2002. ISBN: 978-0-471-38929-3.

[78] Mo, Y. A Critical Analysis on the Rotation Barriers in Butane. *J. Org. Chem.*, **2010**, *75* (8), 2733–2736. doi: 10.1021/jo1001164.

[79] Weber, A. C. J.; de Lange, C. A.; Meerts, W. L.; Burnell, E. E. The Butane Condensed Matter Conformational Problem. *Chem. Phys. Lett.*, **2010**, *496* (4), 257–262. doi: 10.1016/j.cplett.2010.07.014.

[80] Akcasu, A. Z.; Han, C. C. Molecular Weight and Temperature Dependence of Polymer Dimensions in Solution. *Macromolecules*, **1979**, *12* (2), 276–280. doi: 10.1021/ma60068a022.

[81] Dukes, D.; Li, Y.; Lewis, S.; Benicewicz, B.; Schadler, L.; Kumar, S. K. Conformational Transitions of Spherical Polymer Brushes: Synthesis, Characterization, and Theory. *Macromolecules*, **2010**, *43* (3), 1564–1570. doi: 10.1021/ma901228t.

[82] Alexander, S. Adsorption of Chain Molecules With a Polar Head a Scaling Description. *J. Phys. (France)*, **1977**, *38* (8), 983–987. doi: 10.1051/jphys:01977003808098300.

[83] de Gennes, P. G. Conformations of Polymers Attached to an Interface. *Macromolecules*, **1980**, *13* (5), 1069–1075. doi: 10.1021/ma60077a009.

[84] Daoud, M.; Cotton, J. Star Shaped Polymers : A Model for the Conformation and Its Concentration Dependence. *J. Phys. (France)*, **1982**, *43* (3), 531–538. doi: 10.1051/jphys:01982004303053100.

[85] Wijmans, C. M.; Zhulina, E. B. Polymer Brushes at Curved Surfaces. *Macromolecules*, **1993**, *26* (26), 7214–7224. doi: 10.1021/ma00078a016.

[86] Binder, K. Scaling Concepts for Polymer Brushes and Their Test With Computer Simulation. *Eur. Phys. J. E*, **2002**, *9* (3), 293–298. doi: 10.1140/epje/i2002-10076-2.

[87] Lo Verso, F.; Yelash, L.; Egorov, S. A.; Binder, K. Effect of the Solvent Quality on the Structural Rearrangement of Spherical Brushes: Coarse-Grained Models. *Soft Matter*, **2012**, *8* (15), 4185–4196. doi: 10.1039/C2SM06836B.

[88] Shim, D.; Cates, M. E. Finite Extensibility and Density Saturation Effects in the Polymer Brush. *J. Phys. (France)*, **1989**, *50* (24), 3535–3551. doi: 10.1051/jphys:0198900500240353500.

[89] Berne, B. J.; Pecora, R. *Dynamic Light Scattering with Applications to Chemistry, Biology, and Physics*. John Wiley & Sons Inc., New York, 1976. ISBN: 9780486411552.

[90] Stetefeld, J.; McKenna, S. A.; Patel, T. R. Dynamic Light Scattering: A Practical Guide and Applications in Biomedical Sciences. *Biophys. Rev.*, **2016**, *8* (4), 409–427. doi: 10.1007/s12551-016-0218-6.

[91] Ferreira, D.; Bachelard, R.; Guerin, W.; Kaiser, R.; Fouché, M. Connecting Field and Intensity Correlations: The Siegert Relation and How to Test It. *Am. J. Phys.*, **2020**, *88* (10), 831–837. doi: 10.1119/10.0001630.

[92] Frisken, B. J. Revisiting the Method of Cumulants for the Analysis of Dynamic Light-Scattering Data. *Appl. Opt.*, **2001**, *40* (24), 4087–4091. doi: 10.1364/AO.40.004087.

[93] Ross Hallett, F. Particle Size Analysis by Dynamic Light Scattering. *Food Res. Int.*, **1994**, *27* (2), 195–198. doi: 10.1016/0963-9969(94)90162-7.

[94] Sharma, R. V.; Sharma, K. C. The Structure Factor and the Transport Properties of Dense Fluids Having Molecules with Square well Potential, a Possible Generalization. *Physica A*, **1977**, *89* (1), 213–218. doi: 10.1016/0378-4371(77)90151-0.

[95] Cölfen, H.; Völkel, A. Analytical Ultracentrifugation in Colloid Chemistry. In Lechner, M. D.; Börger, L., editors, *Analytical Ultracentrifugation VII*, pages 31–47. Springer. ISBN: 978-3-540-45197-6.

[96] Schuck, P.; Zhao, H.; Brautigam, C. A.; Ghirlando, R. *Basic Principles of Analytical Ultracentrifugation*. CRC Press, Boca Raton, 2015. ISBN: 9780429091827. doi: 10.1201/b19028.

[97] Schuck, P.; Zhao, H. *Sedimentation Velocity Analytical Ultracentrifugation*. CRC Press, Boca Raton, 2017. ISBN: 9781315268705. doi: 10.1201/b21988.

[98] Schuck, P. Size-Distribution Analysis of Macromolecules by Sedimentation Velocity Ultracentrifugation and Lamm Equation Modeling. *Biophys. J.*, **2000**, *78* (3), 1606–1619. doi: 10.1016/S0006-3495(00)76713-0.

[99] Gutiérrez, Y.; Brown, A. S.; Moreno, F.; Losurdo, M. Plasmonics Beyond Noble Metals: Exploiting Phase and Compositional Changes for Manipulating Plasmonic Performance. *J. Appl. Phys.*, **2020**, *128* (8), 080901. doi: 10.1063/5.0020752.

[100] Kelly, K. L.; Coronado, E.; Zhao, L. L.; Schatz, G. C. The Optical Properties of Metal Nanoparticles: The Influence of Size, Shape, and Dielectric Environment. *J. Phys. Chem. B*, **2003**, *107* (3), 668–677. doi: 10.1021/jp026731y.

[101] Murray, W. A.; Barnes, W. L. Plasmonic Materials. *Adv. Mater.*, **2007**, *19* (22), 3771–3782. doi: 10.1002/adma.200700678.

[102] Müller, M. B.; Kuttner, C.; König, T. A. F.; Tsukruk, V. V.; Förster, S.; Karg, M.; Fery, A. Plasmonic Library Based on Substrate-Supported Gradiential Plasmonic Arrays. *ACS Nano*, **2014**, *8* (9), 9410–9421. doi: 10.1021/nn503493c.

[103] Nesvadba, P. Radical Polymerization in Industry. In *Encyclopedia of Radicals in Chemistry, Biology and Materials*. Wiley. ISBN: 9780470971253. doi: 10.1002/9781119953678.rad080.

[104] Grubbs, R. B.; Grubbs, R. H. 50th Anniversary Perspective: Living Polymerization – Emphasizing the Molecule in Macromolecules. *Macromolecules*, **2017**, *50* (18), 6979–6997. doi: 10.1021/acs.macromol.7b01440.

[105] Chiefari, J.; Chong, Y. K.; Ercole, F.; Krstina, J.; Jeffery, J.; Le, T. P. T.; Mayadunne, R. T. A.; Meijs, G. F.; Moad, C. L.; Moad, G.; Rizzardo, E.; Thang, S. H. Living Free-Radical Polymerization by Reversible Addition-Fragmentation Chain Transfer: The RAFT Process. *Macromolecules*, **1998**, *31* (16), 5559–5562. doi: 10.1021/ma9804951.

[106] Barner-Kowollik, C. *Handbook of RAFT Polymerization*. Wiley-VCH, Weinheim, 2008. ISBN: 9783527622757. doi: 10.1002/9783527622757.

[107] Schulz, F.; Homolka, T.; Bastús, N. G.; Puntes, V.; Weller, H.; Vossmeyer, T. Little Adjustments Significantly Improve the Turkevich Synthesis of Gold Nanoparticles. *Langmuir*, **2014**, *30* (35), 10779–10784. doi: 10.1021/la503209b.

[108] Ojea-Jiménez, I.; Bastús, N. G.; Puntes, V. Influence of the Sequence of the Reagents Addition in the Citrate-Mediated Synthesis of Gold Nanoparticles. *J. Phys. Chem. C*, **2011**, *115* (32), 15752–15757. doi: 10.1021/jp2017242.

[109] Honold, T.; Skrybeck, D.; Wagner, K. G.; Karg, M. Fully Reversible Quantitative Phase Transfer of Gold Nanoparticles Using Bifunctional PNIPAM Ligands. *Langmuir*, **2017**, *33* (1), 253–261. doi: 10.1021/acs.langmuir.6b03874.

[110] Hendel, T.; Wuithschick, M.; Kettemann, F.; Birnbaum, A.; Rademann, K.; Polte, J. In Situ Determination of Colloidal Gold Concentrations with UV–Vis Spectroscopy: Limitations and Perspectives. *Anal. Chem.*, **2014**, *86* (22), 11115–11124. doi: 10.1021/ac502053s.

[111] Fustin, C.-A.; Duwez, A.-S. Dithioesters and Trithiocarbonates Monolayers on Gold. *J. Electron Spectros. Relat. Phenomena*, **2009**, *172* (1), 104–106. doi: 10.1016/j.elspec.2009.03.009.

[112] Wu, Y.; Zhou, Y.; Zhu, J.; Zhang, W.; Pan, X.; Zhang, Z.; Zhu, X. Fast Conversion of Terminal Thiocarbonylthio Groups of RAFT Polymers to "Clickable" Thiol Groups via Versatile Sodium Azide. *Polym. Chem.*, **2014**, *5* (19), 5546–5550. doi: 10.1039/C4PY00732H.

[113] Kern, W.; Puotinen, D. A. Cleaning Solutions Based on Hydrogen Peroxide for use in Silicon Semiconductor Technology. *RCA Reviews*, **1970**, *31* (2), 187–206.

[114] Bressler, I.; Kohlbrecher, J.; Thunemann, A. F. SASfit: A Tool for Small-Angle Scattering Data Analysis Using a Library of Analytical Expressions. *J. Appl. Crystallogr.*, **2015**, *48* (5), 1587–1598. doi: 10.1107/S1600576715016544.

[115] Kohlbrecher, J.; Studer, A. Transformation Cycle Between the Spherically Symmetric Correlation Function, Projected Correlation Function and Differential Cross Section as Implemented in SASfit. *J. Appl. Crystallogr.*, **2017**, *50* (5), 1395–1403. doi: 10.1107/S1600576717011979.

[116] Marchetti, A.; Preti, C.; Tagliazucchi, M.; Tassi, L.; Tosi, G. The N,N-Dimethylformamide/Ethane-1,2-diol Solvent System. Density, Viscosity, and Ex-

cess Molar Volume at Various Temperatures. *J. Chem. Eng. Data*, **1991**, *36* (4), 360–365. doi: 10.1021/je00004a005.

[117] Bernal-García, J. M.; Guzmán-López, A.; Cabrales-Torres, A.; Estrada-Baltazar, A.; Iglesias-Silva, G. A. Densities and Viscosities of (N,N-Dimethylformamide + Water) at Atmospheric Pressure from (283.15 to 353.15) K. *J. Chem. Eng. Data*, **2008**, *53* (4), 1024–1027. doi: 10.1021/je700671t.

[118] Contreras S, M. Densities and Viscosities of Binary Mixtures of 1,4-Dioxane with 1-Propanol and 2-Propanol at (25, 30, 35, and 40) °C. *J. Chem. Eng. Data*, **2001**, *46* (5), 1149–1152. doi: 10.1021/je010045v.

[119] Barton, A. F. M. *CRC Handbook of Solubility Parameters and Other Cohesion Parameters*. Routledge, New York, 2nd edition, 1991. doi: 10.1201/9781315140575.

[120] Tornøe, C. W.; Meldal, M. Peptidotriazoles: Copper(I)-Catalyzed 1,3-Dipolar Cycloadditions on Solid-Phase. In Lebl, M.; Houghten, R. A., editors, *Peptides: The Wave of the Future*, pages 263–264. Springer Netherlands. ISBN: 978-94-010-0464-0. doi: 10.1007/978-94-010-0464-0_119.

[121] Meldal, M.; Tornøe, C. W. Cu-Catalyzed Azide-Alkyne Cycloaddition. *Chem. Rev.*, **2008**, *108* (8), 2952–3015. doi: 10.1021/cr0783479.

[122] Agard, N. J.; Prescher, J. A.; Bertozzi, C. R. A Strain-Promoted [3 + 2] Azide-Alkyne Cycloaddition for Covalent Modification of Biomolecules in Living Systems. *J. Am. Chem. Soc.*, **2004**, *126* (46), 15046–15047. doi: 10.1021/ja044996f.

[123] Li, K.; Fong, D.; Meichsner, E.; Adronov, A. A Survey of Strain-Promoted Azide-Alkyne Cycloaddition in Polymer Chemistry. *Chem. Eur. J.*, **2021**, *27* (16), 5057–5073. doi: 10.1002/chem.202003386.

[124] Nair, D. P.; Podgórski, M.; Chatani, S.; Gong, T.; Xi, W.; Fenoli, C. R.; Bowman, C. N. The Thiol-Michael Addition Click Reaction: A Powerful and Widely Used Tool in Materials Chemistry. *Chem. Mater.*, **2014**, *26* (1), 724–744. doi: 10.1021/cm402180t.

[125] Skrabania, K.; Miasnikova, A.; Bivigou-Koumba, A. M.; Zehm, D.; Laschewsky, A. Examining the UV-Vis Absorption of RAFT Chain Transfer Agents and Their Use for Polymer Analysis. *Polym. Chem.*, **2011**, *2* (9), 2074–2083. doi: 10.1039/C1PY00173F.

[126] Sindram, J.; Krüsmann, M.; Otten, M.; Pauly, T.; Nagel-Steger, L.; Karg, M. Versatile Route toward Hydrophobically Polymer-Grafted Gold Nanoparticles from Aqueous Dispersions. *J. Phys. Chem. B*, **2021**, *125* (29), 8225–8237. doi: 10.1021/acs.jpcb.1c03772.

[127] Chong, Y. K.; Krstina, J.; Le, T. P. T.; Moad, G.; Postma, A.; Rizzardo, E.; Thang, S. H. Thiocarbonylthio Compounds [S=C(Ph)S-R] in Free Radical Polymerization with Reversible Addition-Fragmentation Chain Transfer (RAFT Polymerization). Role of the Free-Radical Leaving Group (R). *Macromolecules*, **2003**, *36* (7), 2256–2272. doi: 10.1021/ma020882h.

[128] Yoon, D. Y.; Sundararajan, P. R.; Flory, P. J. Conformational Characteristics of Polystyrene. *Macromolecules*, **1975**, *8* (6), 776–783. doi: 10.1021/ma60048a019.

[129] Kettemann, F.; Birnbaum, A.; Witte, S.; Wuithschick, M.; Pinna, N.; Kraehnert, R.; Rademann, K.; Polte, J. Missing Piece of the Mechanism of the Turkevich Method: The Critical Role of Citrate Protonation. *Chem. Mater.*, **2016**, *28* (11), 4072–4081. doi: 10.1021/acs.chemmater.6b01796.

[130] Nygaard, M.; Kragelund, B. B.; Papaleo, E.; Lindorff-Larsen, K. An Efficient Method for Estimating the Hydrodynamic Radius of Disordered Protein Conformations. *Biophys. J.*, **2017**, *113* (3), 550–557. doi: 10.1016/j.bpj.2017.06.042.

[131] Dekker, F.; Kuipers, B. W. M.; Petukhov, A. V.; Tuinier, R.; Philipse, A. P. Scattering From Colloidal Cubic Silica Shells: Part I, Particle Form Factors and Optical Contrast Variation. *J. Colloid Interface Sci.*, **2020**, *571*, 419–428. doi: 10.1016/j.jcis.2019.11.002.

[132] Hummel, P.; Lerch, A.; Goller, S. M.; Karg, M.; Retsch, M. Simple and High Yield Synthesis of Metal-Polymer Nanocomposites: The Role of Theta-

Centrifugation as an Essential Purification Step. *Polymers*, **2017**, *9* (12), 659. doi: 10.3390/polym9120659.

[133] Jeon, H. B.; Tsalu, P. V.; Ha, J. W. Shape Effect on the Refractive Index Sensitivity at Localized Surface Plasmon Resonance Inflection Points of Single Gold Nanocubes with Vertices. *Sci. Rep.*, **2019**, *9* (1), 13635. doi: 10.1038/s41598-019-50032-3.

[134] Sekhon, J. S. Facile Tuning and Refractive Index Sensitivity of Localized Surface Plasmon Resonance Inflection Points in Hollow Silver Nanoshells. *Plasmonics*, **2021**, *16* (1), 283–292. doi: 10.1007/s11468-020-01277-6.

[135] Maier, S. A. *Plasmonics: Fundamentals and Applications*. Springer US, New York, NY, 2007. ISBN: 978-0-387-37825-1. doi: 10.1007/0-387-37825-1_1.

[136] Mayer, K. M.; Hafner, J. H. Localized Surface Plasmon Resonance Sensors. *Chem. Rev.*, **2011**, *111* (6), 3828–3857. doi: 10.1021/cr100313v.

[137] Volk, K.; Fitzgerald, J. P. S.; Ruckdeschel, P.; Retsch, M.; König, T. A. F.; Karg, M. Reversible Tuning of Visible Wavelength Surface Lattice Resonances in Self-Assembled Hybrid Monolayers. *Adv. Opt. Mater.*, **2017**, *5* (9), 1600971. doi: 10.1002/adom.201600971.

[138] Heller, W. Remarks on Refractive Index Mixture Rules. *J. Phys. Chem.*, **1965**, *69* (4), 1123–1129. doi: 10.1021/j100888a006.

[139] Feller, D.; Otten, M.; Hildebrandt, M.; Krüsmann, M.; Bryant, G.; Karg, M. Translational and Rotational Diffusion Coefficients of Gold Nanorods Functionalized With a High Molecular Weight, Thermoresponsive Ligand: A Depolarized Dynamic Light Scattering Study. *Soft Matter*, **2021**, *17* (15), 4019–4026. doi: 10.1039/D1SM00077B.

[140] Elzey, S.; Tsai, D.-H.; Rabb, S. A.; Yu, L. L.; Winchester, M. R.; Hackley, V. A. Quantification of Ligand Packing Density on Gold Nanoparticles Using ICP-OES. *Anal. Bioanal. Chem.*, **2012**, *403* (1), 145–149. doi: 10.1007/s00216-012-5830-0.

[141] Benoit, D. N.; Zhu, H.; Lilierose, M. H.; Verm, R. A.; Ali, N.; Morrison, A. N.; Fortner, J. D.; Avendano, C.; Colvin, V. L. Measuring the Grafting Density of Nanoparticles in Solution by Analytical Ultracentrifugation and Total Organic Carbon Analysis. *Anal. Chem.*, **2012**, *84* (21), 9238–9245. doi: 10.1021/ac301980a.

[142] Roovers, J.; Zhou, L. L.; Toporowski, P. M.; van der Zwan, M.; Iatrou, H.; Hadjichristidis, N. Regular Star Polymers With 64 and 128 Arms. Models for Polymeric Micelles. *Macromolecules*, **1993**, *26* (16), 4324–4331. doi: 10.1021/ma00068a039.

[143] Haydukivska, K.; Blavatska, V.; Paturej, J. Universal Size Ratios of Gaussian Polymers With Complex Architecture: Radius of Gyration vs Hydrodynamic Radius. *Sci. Rep.*, **2020**, *10* (1), 14127. doi: 10.1038/s41598-020-70649-z.

[144] Binder, K.; Milchev, A. Polymer Brushes on Flat and Curved Surfaces: How Computer Simulations Can Help to Test Theories and to Interpret Experiments. *J. Polym. Sci. B*, **2012**, *50* (22), 1515–1555. doi: 10.1002/polb.23168.

[145] Ligoure, C.; Leibler, L. Thermodynamics and Kinetics of Grafting End-Functionalized Polymers to an Interface. *J. Phys. France*, **1990**, *51* (12), 1313–1328.

[146] Reineck, P.; Gómez, D.; Ng, S. H.; Karg, M.; Bell, T.; Mulvaney, P.; Bach, U. Distance and Wavelength Dependent Quenching of Molecular Fluorescence by Au@SiO2 Core–Shell Nanoparticles. *ACS Nano*, **2013**, *7* (8), 6636–6648. doi: 10.1021/nn401775e.

[147] Sindram, J.; Karg, M. Polymer Ligand Binding to Surface-Immobilized Gold Nanoparticles: A Fluorescence-Based Study on the Adsorption Kinetics. *Soft Matter*, **2021**, *17* (32), 7487–7497. doi: 10.1039/D1SM00892G.

[148] Valeur, B.; Berberan-Santos, M. N. *Molecular Fluorescence: Principles and Applications, Second Edition.* Wiley-VCH, Weinheim, 2 edition, 2012. ISBN: 978-3-527-65003-3.

[149] von Smoluchowski, M. Versuch einer mathematischen Theorie der Koagulationskinetik kolloider Lösungen. *Z. Phys. Chem.*, **1918**, *92U* (1), 129–168. doi: doi:10.1515/zpch-1918-9209.

[150] Collins, F. C.; Kimball, G. E. Diffusion-Controlled Reaction Rates. *J. Colloid Sci.*, **1949**, *4* (4), 425–437. doi: 10.1016/0095-8522(49)90023-9.

[151] Collins, F. C.; Kimball, G. E. Diffusion-Controlled Reactions in Liquid Solutions. *Ind. Eng. Chem.*, **1949**, *41* (11), 2551–2553. doi: 10.1021/ie50479a040.

[152] North, A. M. Diffusion-Controlled Reactions. *Q. Rev. Chem. Soc.*, **1966**, *20* (3), 421–440. doi: 10.1039/QR9662000421.

[153] Northrup, S. H.; Hynes, J. T. On the Description of Reactions in Solution. *Chem. Phys. Lett.*, **1978**, *54* (2), 244–247. doi: https://doi.org/10.1016/0009-2614(78)80093-1.

[154] Szabo, A.; Shoup, D.; Northrup, S. H.; McCammon, J. A. Stochastically Gated Diffusion-Influenced Reactions. *J. Chem. Phys.*, **1982**, *77* (9), 4484–4493. doi: 10.1063/1.444397.

[155] Gaveau, B.; Hynes, J. T.; Kapral, R.; Moreau, M. A Stochastic Theory of Chemical Reaction Rates. I. Formalism. *J. Stat. Phys.*, **1989**, *56* (5), 879–893. doi: 10.1007/BF01016783.

[156] Elliot, A. J.; McCracken, D. R.; Buxton, G. V.; Wood, N. D. Estimation of Rate Constants for Near-Diffusion-Controlled Reactions in Water at High Temperatures. *J. Chem. Soc.*, **1990**, *86* (9), 1539–1547. doi: 10.1039/FT9908601539.

Appendix

A UV/Vis spectra of AuNP@PS

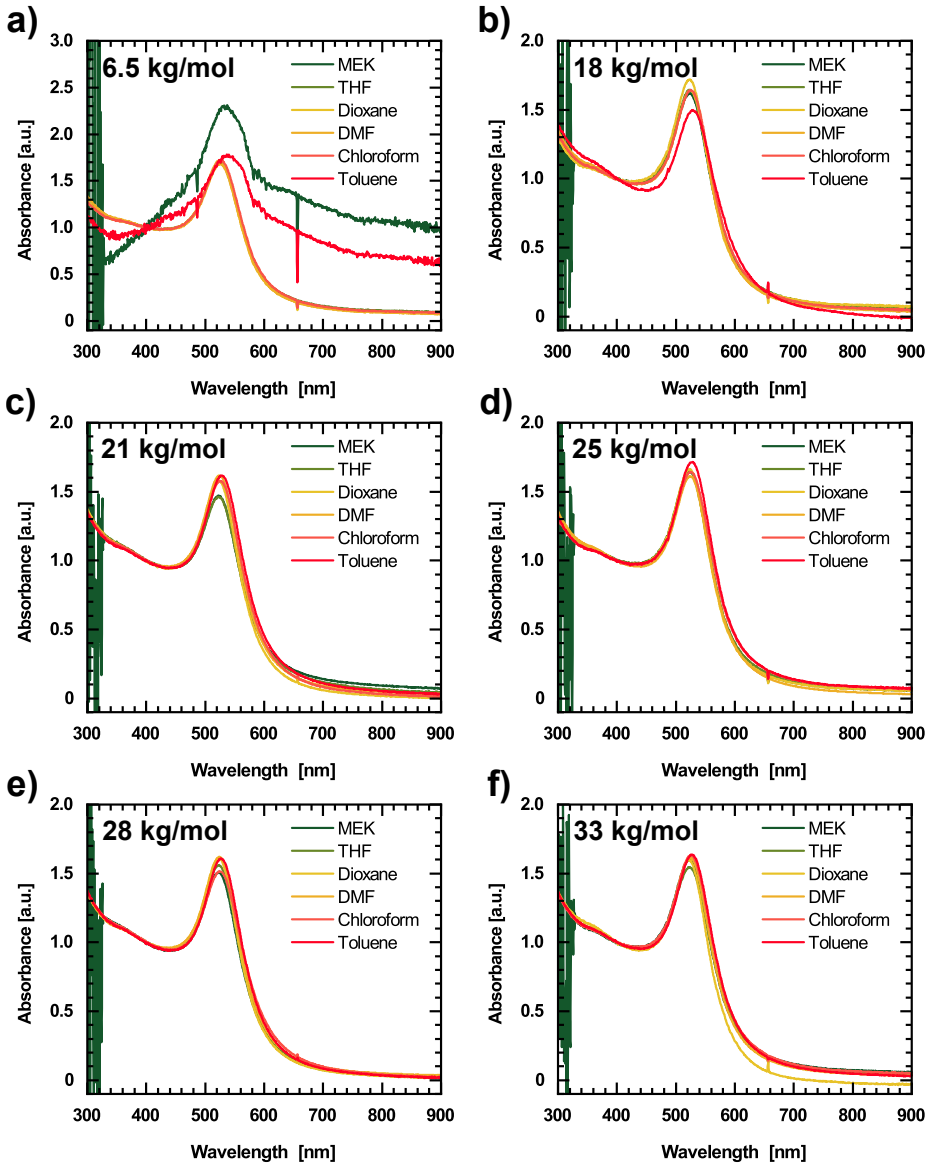

Figure A.1: Normalized UV/Vis spectra of AuNP@PS in different solvents.

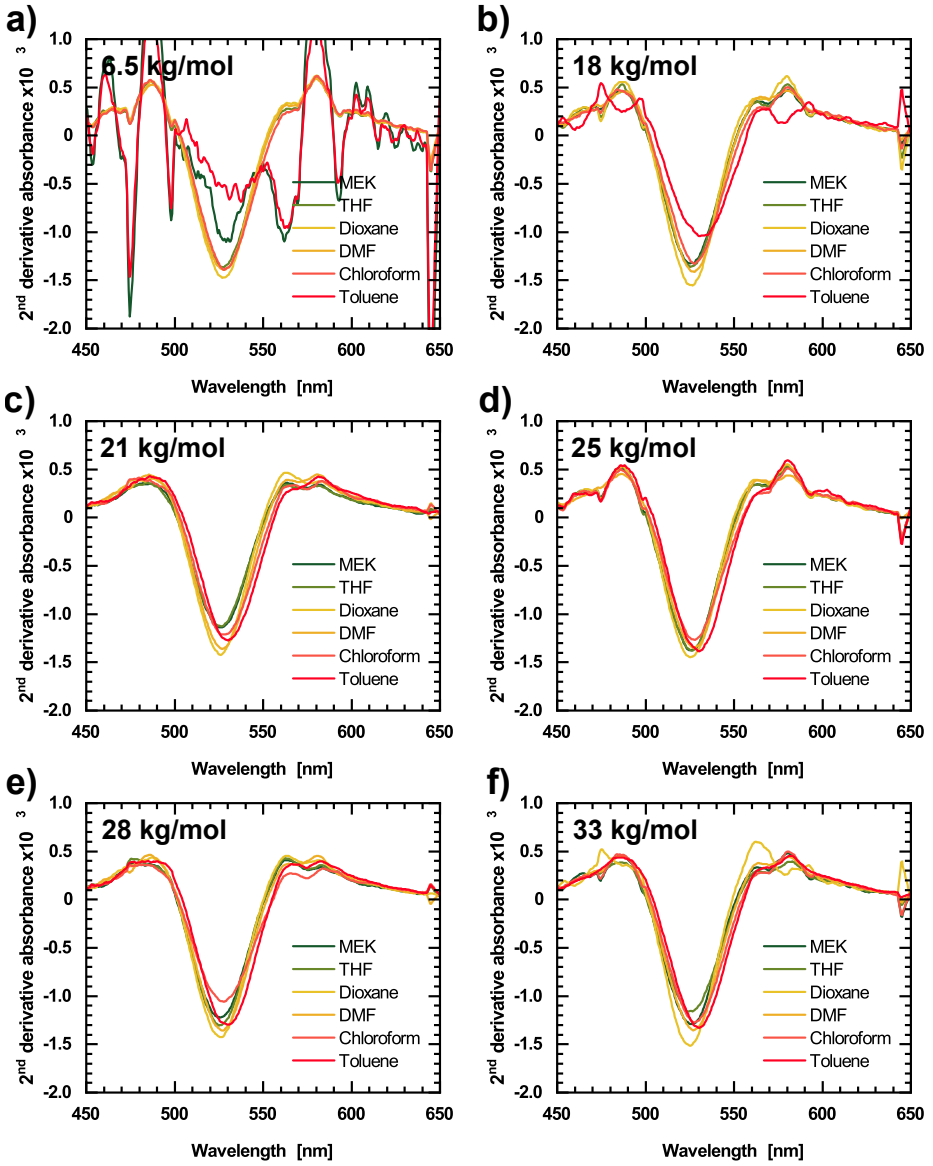

Figure A.2: 2nd derivatives of UV/Vis spectra of AuNP@PS in different solvents.

B AFM images of AuNP immobilized on glass substrates

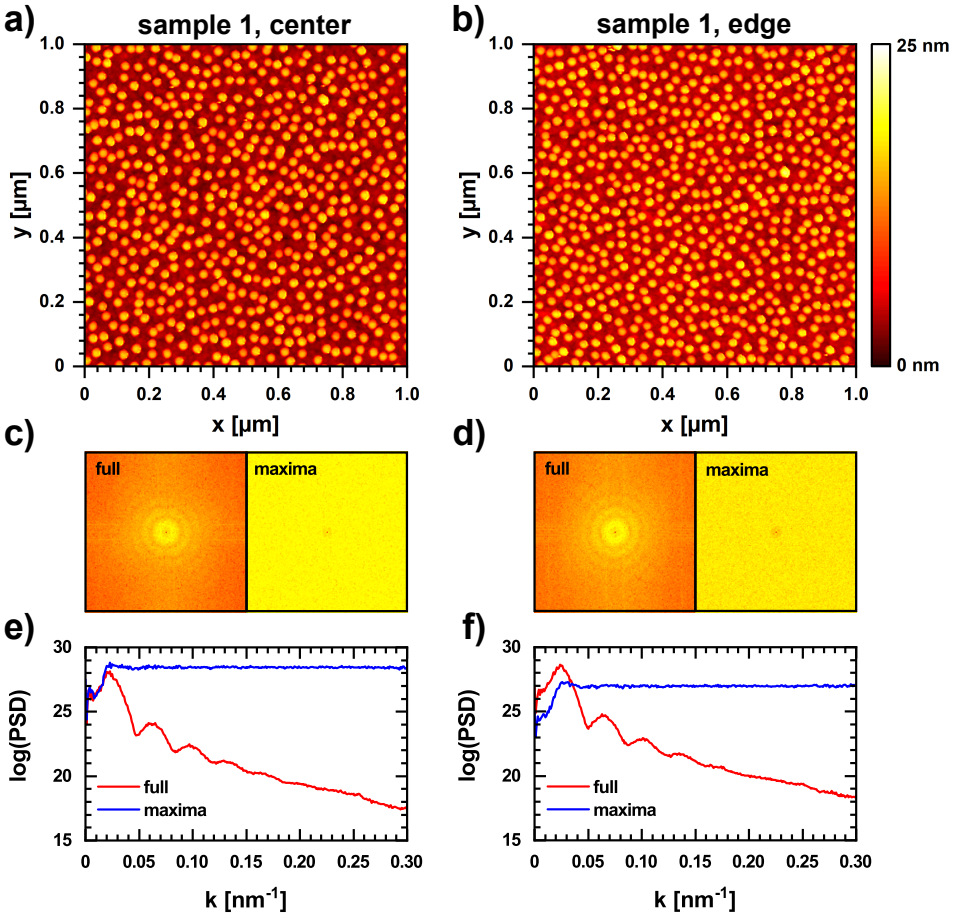

Figure B.1: a – b) AFM height images of the center and edge region of sample 1 of a series of AuNP on amine functionalized glass substrates. c – d) FFTs of the same height images (full) and of the particle position maps (maxima). e –f) Power spectral density (PSD) curves obtained from radial averaging of the FFTs around the center point. Reproduced from Ref. [147] with permission from the Royal Society of Chemistry.

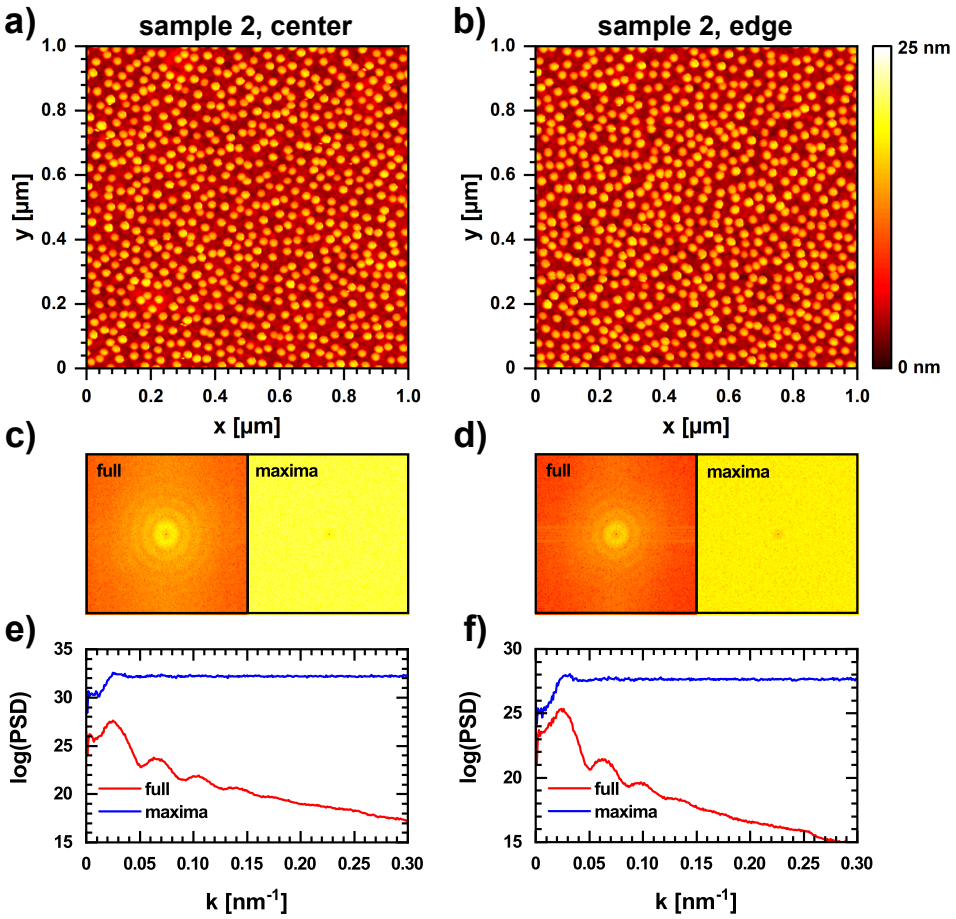

Figure B.2: a – b) AFM height images of the center and edge region of sample 2 of a series of AuNP on amine functionalized glass substrates. c – d) FFTs of the same height images (full) and of the particle position maps (maxima). e –f) Power spectral density (PSD) curves obtained from radial averaging of the FFTs around the center point. Reproduced from Ref. [147] with permission from the Royal Society of Chemistry.

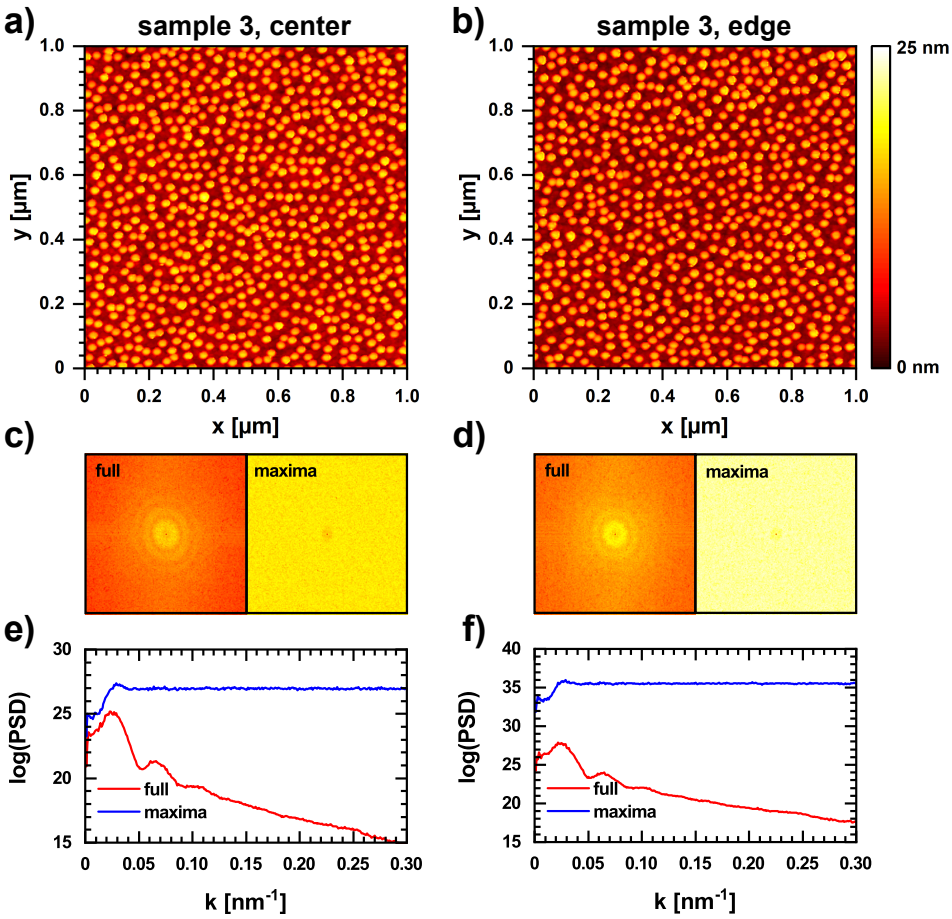

Figure B.3: a – b) AFM height images of the center and edge region of sample 3 of a series of AuNP on amine functionalized glass substrates. c – d) FFTs of the same height images (full) and of the particle position maps (maxima). e –f) Power spectral density (PSD) curves obtained from radial averaging of the FFTs around the center point. Reproduced from Ref. [147] with permission from the Royal Society of Chemistry.

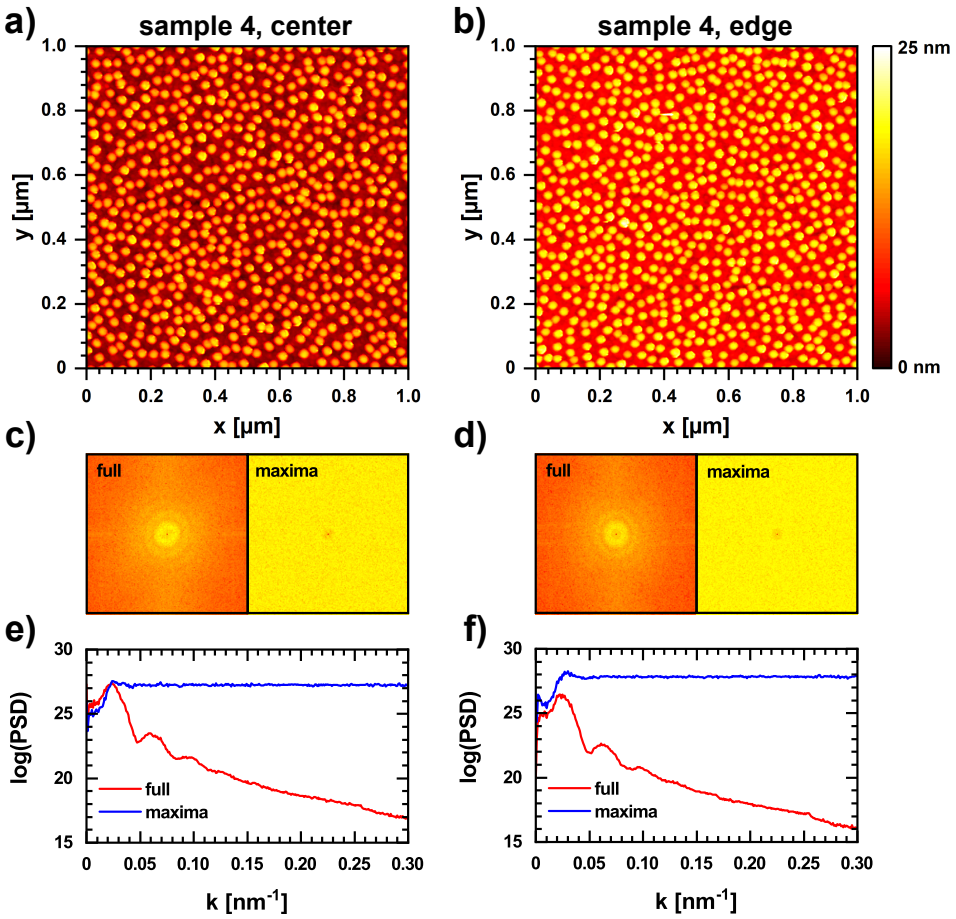

Figure B.4: a – b) AFM height images of the center and edge region of sample 4 of a series of AuNP on amine functionalized glass substrates. c – d) FFTs of the same height images (full) and of the particle position maps (maxima). e –f) Power spectral density (PSD) curves obtained from radial averaging of the FFTs around the center point. Reproduced from Ref. [147] with permission from the Royal Society of Chemistry.

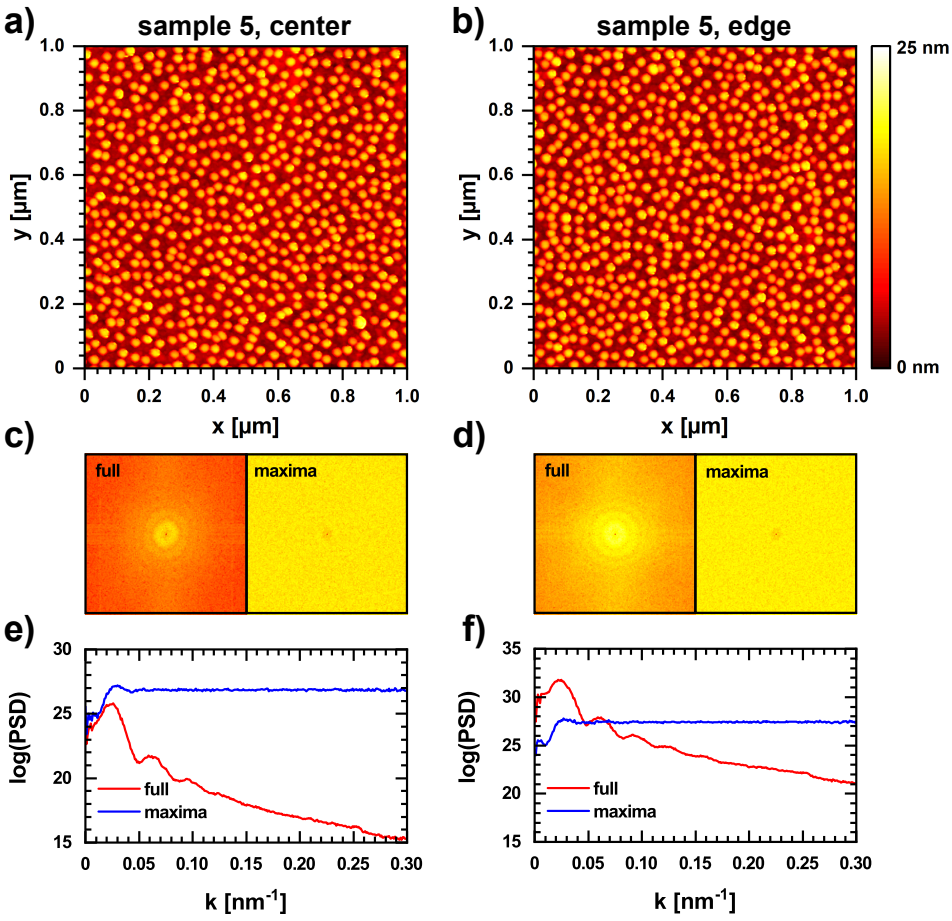

Figure B.5: a – b) AFM height images of the center and edge region of sample 5 of a series of AuNP on amine functionalized glass substrates. c – d) FFTs of the same height images (full) and of the particle position maps (maxima). e –f) Power spectral density (PSD) curves obtained from radial averaging of the FFTs around the center point. Reproduced from Ref. [147] with permission from the Royal Society of Chemistry.